Effect of Chemical Substitutions on the Quantum Spin Liquid Candidates $Na_4Ir_3O_8$ and $Ca_{10}Cr_7O_{28}$

A thesis submitted by

ASHIWINI BALODHI

For the award of the degree of

DOCTOR OF PHILOSOPHY

Department of Physical Sciences

Indian Institute of Science Education and Research Mohali

May 2019

EX root = ../thesis-example.tex

Declaration

The work presented in this dissertation has been carried out by me under the guidance of Dr. Yogesh Singh at the Indian Institute of Science Education and Research Mohali. This work has not been submitted in part or in full for a degree, a diploma, or a fellowship to any other university or institute. Whenever contributions of others are involved, every effort is made to indicate this clearly, with due acknowledgment of collaborative research and discussions. This thesis is a bonafide record of original work done by me and all sources listed within have been detailed in the bibliography.

Ashiwini Balodhi

In my capacity as the supervisor of the candidate′s doctoral thesis, I certify that the above statements by the candidate are true to the best of my knowledge.

Dr. Yogesh Singh
(Supervisor)

Acknowledgements

It is my honor to use this opportunity to acknowledge everyone who has helped me in completing this work.

First of all, It is a great pleasure to express my deepest sense of gratitude and sincere appreciation to my supervisor Dr. Yogesh Singh, who made it possible to carry out my thesis at Novel Material Lab. He turned out to be much more than a Ph.D. supervisor and guided me through all my ventures.

I would like to thank my doctoral committee member Dr. Sanjeev Kumar and Dr. Goutam Sheet for his useful comments and support throughout the Ph.D. Their direction and guidance have been very fruitful during the Ph.D. work.

I would like to thank the reviewers for their thoughtful comments and efforts towards improving this thesis. Their suggestions helped me to improve the quality of thesis.

I would like to acknowledge XRD facility and SEM facility of IISER Mohali. I am grateful to Inderjit and Vivek enough for lending his expertise in using the EDX facility as often as I required it.

I am happy to be a part of a dynamic research group with numerous research directions. My sincere thanks to the group mates: Dr. Gyaneshwer, Anzar Ali, Amit, Shama, Kavita, Ankit, Prins, and Dr. Radha Krishan Gopal.

Many thanks to my friend and group mate Deepak, Mayank, Shubendu, Jaskaran, and Rakesh for their fruitful suggestions, critical comments, wonderful party time, and support that help in making the stay pleasant during the Ph.D. My sincere appreciation to my friends, seniors, and all who contributed to the completion of my doctoral dissertation.

My vocabulary fails to accentuate my profound reverence and sincere regards to my mother and my father for their ceaseless inspiration, moral and spiritual support, pro-

found love and unending encouragement, guiding me to achieve success at every step in life.

The affection, ultimate help, love and constant encouragement that I always got from my sister, my elder brothers is always memorable. Special thanks go to my lovely niece Navya and nephew Aadu.

Last but not the least, I thank the supreme power, the Almighty that blesses one with a thirst for knowledge and the capabilities to learn.

Ashiwini Balodhi

List of Publications

1. Effect of disorder on the quantum spin liquid candidate $Na_4Ir_3O_8$
   Ashiwini Balodhi and Yogesh Singh
   submitted- arxiv:1807.03940 (2018).

2. Crystal growth and magnetic anisotropy in the spin - chain ruthenate Na_2RuO_4
   Ashiwini Balodhi and Yogesh Singh
   Phys. Rev. Materials **2**, 024403 (2018).

3. Synthesis and pressure and field-dependent magnetic properties of the kagome-bilayer spin liquid $Ca_{10}Cr_7O_{28}$
   Ashiwini Balodhi and Yogesh Singh
   Phys. Rev. Materials **1**, 024407 (2017).

4. Spin liquid like Raman signatures in the hyperkagome iridate $Na_4Ir_3O_8$
   S. N. Gupta, P. V. Sriluckshmy, **A. Balodhi**, Y. Singh, D. V. S. Muthu, S. R. Hassan, T. V. Ramakrishnan, and A. K. Sood
   Phys. Rev. B. **94**, 155153 (2016).

5. Raman signatures of strong Kitaev exchange correlations in $(Na_{1-x}Li_x)_2IrO_3$: Experiments and theory
   S. N. Gupta, P. V. Sriluckshmy, **A. Balodhi**, K. M. Mehlawat, D. V. S. Muthu, Y. Singh, S. R. Hassan, T. V. Ramakrishnan, A. K. Sood
   EPL **114**, 47004 (2016).

6. Spin dynamics in $Na_{4-x}Ir_3O_8$ (x = 0.3 and 0.7) investigated by ^{23}Na NMR and μSR
   S. Yoon, S. -H. Baek, **A. Balodhi**, W. -J. Lee, K. -Y. Choi, I. Watanabe, J. S. Lord, B. Büchner, B. J. Suh and Y. Singh
   J. Phys. Condens. Matter **27**, 485603 (2015).

7. Evolution of magnetic, transport, and thermal properties in $\mathrm{Na}_{4-x}\mathrm{Ir}_3\mathrm{O}_8$
   Ashiwini Balodhi, A. Thamizhavel, and Yogesh Singh
   Phys. Rev. B. **91**, 224409 (2015).

Abstract

Quantum spin liquids (QSLs) are exotic states of matter, in which magnetic frustration and strong quantum fluctuations destroy long-range magnetic order. Highly frustrated lattices with antiferromagnetic exchange interactions and low-spin value open up possibilities in the exploration and designing of new QSL candidates. QSLs in three-dimensions are very rare, and only a couple of candidate materials exist.

In this thesis, we investigate bond-disordered quantum spin-liquid state in three dimensional magnetic insulators $Na_4Ir_3O_8$ and $Ca_{10}Cr_7O_{28}$. The central theme of thesis is to explore how these QSL's respond to external perturbations like pressure, magnetic field, and chemical substitutions. In this thesis, I have synthesized two QSL candidates the hyperkagome $Na_4Ir_3O_8$ and kagome bilayer $Ca_{10}Cr_7O_{28}$ and studied their electrical transport, magnetic, and thermal properties. Our work provides several new results: (i) the strongly frustrated Mott insulating state in $Na_4Ir_3O_8$ is quite robust against large removal of Na from the lattice, (ii) evidence through magnetic (Ru) and nonmagnetic (Ti) impurity doping in a magnetic sublattice, of fragile magnetic order and importance of nearestneighbour interactions and spin-orbit coupling in deciding the magnetic ground state in $Na_4Ir_3O_8$, (iii) high-pressure magnetic susceptibility measurements reveal the QSL at ambient pressure is quite robust and may not depend on a delicate balance between any specific values of competing exchange interactions in $Ca_{10}Cr_7O_{28}$, and (iv) the first experimental realization of a perfect nonmagnetic analog $Ca_{10}V_7O_{27.5}$ of $Ca_{10}Cr_7O_{28}$, which enables an accurate exclusion of the lattice heat capacities.

Contents

List of Figures

List of Tables

LIST OF TABLES

Chapter 1

General Introduction

1.1 Introduction

Recent research in Condensed Matter Physics has opened up the possibility of phases and phase transitions, which can't be understood within the previously existing frameworks to understand these phenomena. The success of condensed matter theory rests on two pillars: Fermi liquid theory (FL) and Landau symmetry-breaking theory. The importance of both the approaches made them fundamental theories in condensed matter physics up to the height from where they set the language and notion used to communicate and interpret physical observations in condensed matter physics. The concept of elementary excitations (quasi-particle) introduced by Landau in Fermi-liquid theory is quite successful in explaining some interacting quantum systems at low-temperatures. Landau showed that the problem of correlated particles can be replaced by a problem of a weakly interacting Fermi gas made up of quasi-particles with re-normalized properties. The applicability of the quasi-particle theory was not limited to Fermionic systems like Helium (He^3), but it extends to Bosonic systems like He^4 [1]. Recently the quasi-particle concept has become a playground for theoretical condensed matter physicists to predict properties of matter by introducing quasi-particles, like gapped or gapless spinons, and Majorana fermions in spin-liquids, Skyrmions and Weyl-Fermions etc[2]-[8].

The study of magnetism has been an enduring theme in condensed matter physics. Magnetism in a material arises due to the orbital and spin motion of an electron. In a material the competition among the different energy scales like on-site Hubbard interaction U, Hund's coupling J_H, the Spin-Orbit coupling (SOC) λ, the crystal field energy Δ, and the electron kinetic energy (hopping) t, can lead to different magnetic ground states. Phase transitions from a disordered state to an ordered ground state became the core theme of study in magnetism. Landau symmetry-breaking theory has proven to be useful to study the phase transitions in condensed matter physics. Phase transitions induced by a temperature variation ($T \geq 0$) are called classical phase transitions. Due to the absence of entropy at T = 0, a classical phase transition can't occur at T = 0. Classical phase transitions are very well studied and understood. Simple magnetic systems with large spins on bi-partite lattices undergo classical phase transitions into long-range magnetically ordered states.

On the other hand in quantum systems, the small spin value (S = 1/2) leads to large quantum fluctuations which can suppress the phase transition to T = 0, which is referred to as a Quantum phase transition (QPT). Such QPTs were investigated by Hertz (1976) who developed a renormalization group approach to the study of critical phenomena in quantum-mechanical systems (magnetic transitions of itinerant electrons) at zero or low-temperatures, where classical free-energy functionals of the Landau-Ginzburg-Wilson kind are not valid [9]. Many classical magnetic transitions can be tuned to T = 0 by some external control parameter like pressure and magnetic field. The dipolar-coupled Ising ferromagnet $LiHoF_4$ (S = 1/2) is an example of such a classical to quantum crossover. In $LiHoF_4$ the classical, thermally driven transition at T_c = 1.53 K can be converted into a quantum transition at T = 0 driven by a transverse magnetic field H_t applied perpendicular to the Ising axis [10][11][12].

The three well known conventional magnetic phase transitions, i.e., paramagnet to ferromagnet, antiferromagnet or ferrimagnets can be characterized by an order parameter. The order parameter is a response function, which equals to zero in the disordered paramagnetic state and non-zero in the ordered state. The total magnetization in ferromagnet and sub-lattice magnetization in antiferromagnets work as an order parameter for these transitions.

In 1982, the remarkable discovery of Fractional Quantum Hall (FQH) effect opened a new chapter in condensed matter physics by introducing the word "Quantum-order." This quantum order was characterized by the absence of any order parameter in FQH state. Many different degenerate FQH states are possible and these have the same symmetry and cannot be described by the Landau symmetry-breaking theory. The need to explain quantum order required new mathematical techniques which go beyond the Landau Fermi liquid theory and Landau symmetry-breaking theory [13][14]. Quantum spin-liquids are the example of states of matter which can not be understood within the language of symmetry breaking and conventional order parameters.

In the following sections, we will slowly build the definition of what quantum spin-liquids are.

1.1.1 Mott insulator

Insulators are materials having vanishing electrical conductivity at zero temperature. The mechanism behind the insulating behavior divides insulators into two main categories. Band, Peierls and Anderson insulators lie in the first class, which can be understood by the single electron-ion interaction. Mott insulators correspond to the second class, where the insulating behavior is due to the correlation effects arising from the electron-electron interaction.

Band insulators can be understood within the band theory picture. The success of band theory in condensed matter physics is its ability to differentiate a large number of crystalline solids as metals or insulators by simply looking at the filling of electronic bands. These energy bands can be separated by an energy gap due to the influence of the periodic lattice potential. According to the band theory, if a material has an odd number of electron per site, i.e. there is a non-vanishing density of states at the Fermi level $\rho(\epsilon_F) \neq 0$, the material is classified as a metal. For insulators, vanishing density of states $\rho(\epsilon_F) = 0$ at the Fermi level, are the consequences of energy band gap in the material. Even number of electron per site results in a band insulator. Band theory of solids works well for the broad band s and p shell orbitals where electron can delocalize very easily and correlations are weak.

The breakdown of band theory comes in the transition metal oxides like Cuprates and Manganites having a narrow band of partially filled d and f electrons. The most dramatic failure of band theory is the ignorance of correlations effects. As a result of ignoring electron-electron correlation, it predicts that several known insulators should be metals. For example, in the transition metal oxide CaO, the number of electrons per unit cell is 15. According to band theory of solids, CaO should be a metal for having an odd number of electrons per unit cell, but it is known to be a robust insulator. V_2O_3

[15], Sr_2IrO_4 [16][17], Na_2IrO_3 [18][19], square-lattice material La_2CuO_4 [20] and $Sr_3Ru_2O_7$ [21] are some examples of the materials showing the insulating behavior as a result of electron-electron correlations.

The electrical transport properties of a material are the result of the competition between localization and delocalization. The Mott-Hubbard model allows a meaningful description of these two opposing behavior of an electron in a lattice. The form of the one-band Hubbard model Hamiltonian is

$$H_{band} = -t \sum_{<i,j>} \sum_{\sigma} (C^{\dagger}_{i\sigma} C_{j\sigma} + C^{\dagger}_{j\sigma} C_{i\sigma}) + U \sum_{i} \hat{n}_{i\uparrow} \hat{n}_{i\downarrow} \tag{1.1}$$

where t is the transfer integral or hopping integral as shown in Fig: 1.1(a). It is an interaction integral that represents the kinetic energy gain of electrons hopping between sites. Thus it is directly related to orbital overlap and to bandwidth W. $C^{\dagger}_{i\sigma}$ creates an electron with spin σ at the lattice site i, and $\hat{n}_{i\uparrow}\hat{n}_{i\downarrow}$ is the occupation number operator which counts the number of electrons with spin $\uparrow$ and $\downarrow$ on site i.

There are two limiting cases in this Hubbard model:

Case-1: U = 0, when Coulomb repulsion is zero, all we have is non-interacting band electrons, and we essentially get the band model.

Case- 2: t = 0 (or U/t = ∞) The band structure collapses and the system decomposes into isolated atoms (or molecules). This condition is called the atomic limit.

When both U and t are finite, the Hubbard model is most fascinating. If we consider the electron hopping between the neighboring sites, the tight binding approximation results in the cosine dispersion relation

$$\epsilon(\boldsymbol{k}) = -2t \sum_{i=1}^{d} cos(k_l a) \tag{1.2}$$

When we introduce the hopping term t, the charge excitation becomes mobile and now the hopping term leads to a broadening of the atomic levels into a tight binding band of bandwidth W = 2z, where $z = 2d$ is the number of the nearest neighbors[22]. The singly occupied band is lower by U in energy from the doubly occupied band. This upper energy band is called "upper Hubbard-band," and the lower band is called "lower Hubbard band" as shown in Fig: 1.1(b). Since there is an energy gap for a single charge excitation at the half-filling of bands the system behaves like an insulator. This

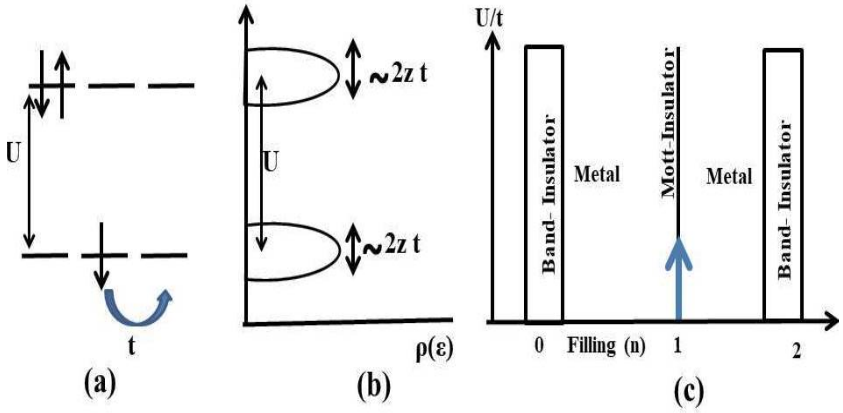

Figure 1.1: (a) An electron can hop from one site to another site as a result of its kinetic energy t, but to have two electrons on the same site will cost an energy U, which is an effective on-site Coulomb repulsion between the two electrons. (b) Energy ε versus density of states $\rho(\varepsilon)$ plot showing the energy level scheme of Hubbard sub-bands. (c) U vs band filing phase diagram for Mott insulator.

type of insulators are known as Mott insulators. A metal to Mott insulator transition can be driven by either tuning U/t or by the band filling n as shown in Fig: 1.1(c).

1.1.2 Frustrated magnets

Psychological theory and dominant social ideologies describe the frustration in normal human life as a natural response to opposition. Although it can be an indicator of the problems in a person's life and it's very hard to get rid of frustration forever, but sometimes as a result, it can act as a motivator to learn some new ways or techniques in order to minimize the frustrations. Physics is also not untouched by frustration and this concept has been applied broadly in condensed matter physics. The first appearance of "frustration" in magnetism came in the context of spin-glasses [10][23][24][25]. Frustration in condensed matter physics is a condition where the interactions between the magnetic moments are incompatible with their spatial arrangement in a lattice geometry. This frustration phenomenon leads to exotic and remarkable properties of physical systems.

P. W. Anderson suggested that triangular structure based lattices are one of the best possibility to melt the expected Neel ordering in a magnet [26]. Thus the materials based on lattices with triangular geometry and nearest-neighbor antiferromagnetic exchange interactions belong to the family of geometrically frustrated magnets. Triangular, kagome (in two-dimensions), hyper-kagome and pyrochlore are some of the examples of geometrically frustrated lattices. We briefly discuss some of these lattices below:

1.1.2.1 The triangular lattice

In 2-dimension, the triangular lattice works as an essential building block for the highly frustrated magnet (HFM) compounds because most of the well understood HFM compounds have magnetic lattices made out of triangles. As shown in Fig: 1.2(a), the triangular lattice consists of edge-shared triangular sub-units, where a vertex is connected to six neighboring vertices. This triangular geometry gives rise to the geometrical frustration. Consider a single triangular unit as shown in Fig: 1.2(b), and place Ising spins on the corners of the triangle. The ferromagnetic exchange between the spin-pair leads to a stable ferromagnetic ground state. If the interactions between each spin pair are antiferromagnetic, then due to the triangular geometry, it's impossible to satisfy all three spin-pair antiferromagnetic interactions simultaneously. As a result, the system finds no way to simultaneously satisfy the three interactions while the system is in the lowest energy state. As shown in Fig: 1.2(c) its ground state is six-fold degenerate, and all of the three spins are frustrated in each ground state because none of them can satisfy its two neighbors simultaneously. Wannier in 1950, studied a classical model of Ising spins on the triangular net with antiferromagnetic interaction. This classical ground state is highly degenerate with a larger residual (T = 0) entropy S(0) = 0.3383R [27]. With a comparison of ordered ferromagnetic state, the energy for an antiferromagnetic case is one-third of the ordered ferromagnetic one. Due to the absence of any singularity, the system remains disordered.

There is a long list of real materials with triangular lattices showing some remarkable properties like unconventional spin-freezing in $NiGa_2S_4$ [28] and spin liquid ground states in κ-(BEDT-TTF)$_2$Cu$_2$(CN)$_3$ [29][31][58], $Ca_{10}Cr_7O_{28}$ [32][33] and $EtMe_3Sb[Pd(dmit)_2]_2$ [34][35].

1.1.2.2 The kagome lattice

Antiferromagnetic solids based on the kagome lattice are of great interest because of their geometrically induced magnetic frustration. The word kagome is derived from

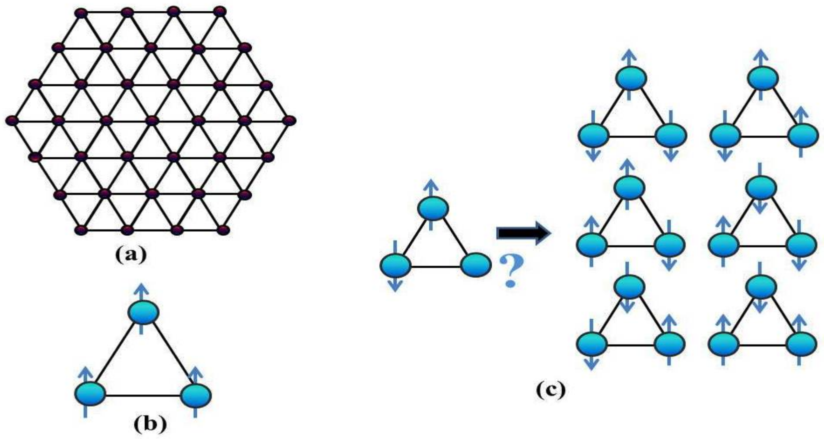

Figure 1.2: (a) A triangular lattice. (b) Ferromagnetic ground state of a triangular lattice (unfrustrated). (c) A degenerate ground states on the triangular lattice as a consequence of geometrical frustration.

the Japanese word used for a particular Japanese bamboo-basketry and became popular in the magnetism community when it was connected to geometrical frustration by Itiro Syozi in 1951 [36]. The kagome lattice comprises of a planar array of corner-sharing triangles which can be seen as a diluted triangular lattice as shown in Fig: 1.3. This combination of regular triangles and hexagons gives a huge classical ground state degeneracy as a consequence of frustration. The kagome lattice has been extensively studied both theoretically and experimentally as a source of exotic physical properties. We will discuss magnetism in the kagome lattice in more detail later.

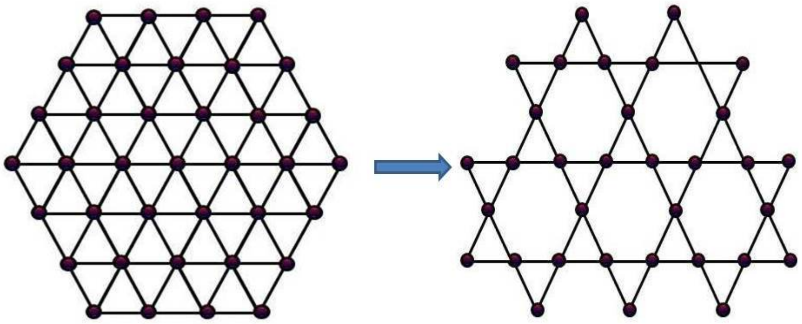

Figure 1.3: The kagome lattice which can be seen as a diluted triangular lattice.

1.1.2.3 The pyrochlore lattice

The pyrochlore lattice shown in Fig:1.4(a), is one of the most celebrated frustrated lattice in 3-dimensions. This three-dimensional frustrated lattice contains a network of corner shared tetrahedra. As a result of strong frustration, pyrochlore lattice materials show some exciting phenomenon, which includes the prediction of magnetic monopole quasiparticles and magnetic Coulomb phase in the spin-ice family [37][38]. Spin-ice is classified as a very unusual magnet, where the lattice geometry alone cannot cause frustration. In spin-ice, the presence of strong local Ising anisotropy leads to a geometrically frustrated ground state even though it has ferromagnetic interactions [39][40][41]. The "two spin-in and two spin-out" condition is shown in fig: 1.4(b) found in the pyrochlore materials is known as "spin-ice rules." The rare earth magnets $Ho_2Ti_2O_7$, $Dy_2Ti_2O_7$, and $Ho_2Sn_2O_7$ are the well known spin-ice materials [39]. Exotic spin-liquid states are also claimed to be found in 3-dimensional pyrochlore lattice materials Y(Sc)Mn_2, and $Lu_2Mo_2O_5N_2$ [42][43].

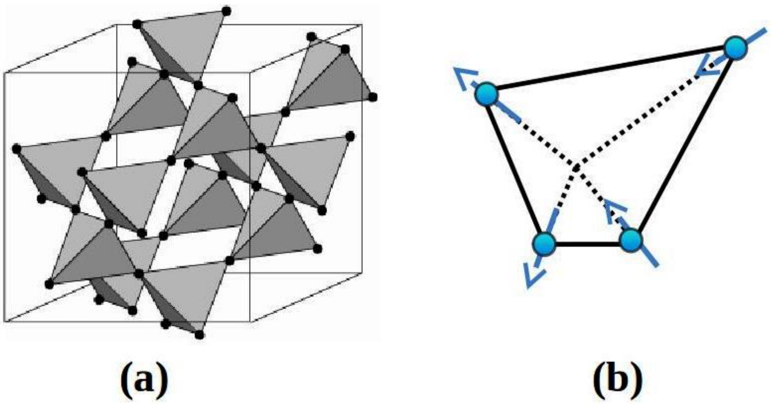

Figure 1.4: (a) 3 - dimensional pyrochlore lattice [Figure from ref. [73]]. (b) The "spin-ice" rule in pyrochlore lattice.

1.1.2.4 The hyper-kagome lattice

The crystal lattice in the materials $Na_4Ir_3O_8$ and $Gd_3Ga_5O_{12}$ is called hyperkagome lattice. In contrast to the kagome lattice, where the triangles lie in a plane, hyperkagome lattice is built from a three-dimensional network of corner-sharing triangles. In parallel to rapid experimental progress in discovering new materials, the hyperkagome lattice has also drawn theoretical attention due to its non-symmorphic space group symmetry which includes a space group operation combining translation by a fraction of the unit cell and a point group operation, such as screw or glide operations. These can lead to non-trivial topological properties.

1.1.3 Spin Liquid-A spin world in its own image

The term Quantum Spin-Liquid (QSL), an elusive state of matter, originated from research in highly frustrated insulating magnets [44][45]. As shown in Fig-1.5, the conventional magnetic systems show long-range magnetic order below a critical temperature T$_C$. The ordered Neel state has broken translational, spin-rotational, time-reversal, and parity symmetry with low-energy spin-1 gapless "Goldstone" mode excitations, or magnons. The Valence-Bond crystal (VBC) also shows broken translational symmetry without breaking spin rotational symmetry. The several fold degenerate ground state of VBC has an integer spin-gapped excitation spectrum. In contrast to the conventional magnetic states, the spin-liquid phase behaves as a cooperative paramagnetic state, and it doesn't order even at absolute zero [44][46]. The cooperative paramagnetic state has no broken symmetry and the excitations are characterized by a gapped or gapless fractionalized quasiparticle (spinon) spectra.

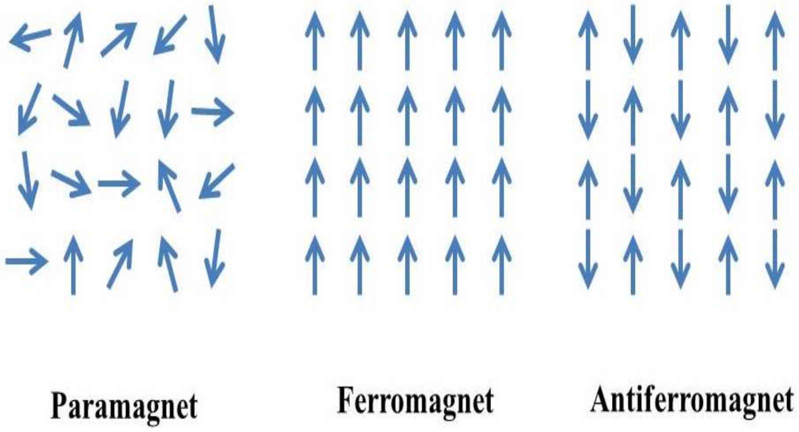

Figure 1.5: Conventional magnetic ground state

The term quantum spin-liquid was introduced by Anderson in 1973, and was derived by making a comparison between valance bond solids and quantum-liquid ground state found in the Resonating Valance Bond (RVB) theory. In his pioneering theoretical work, Anderson predicted the RVB state as an alternative to Neel order, which established a new research domain in many body correlated electron systems [26].

A decade later the discovery of Quantum Hall effect and Fractional Quantum Hall effect (1983), offered a new way in which strongly correlated materials in low-dimension could establish an order that disobeyed the traditional Landau paradigm of symmetry breaking in condensed matter physics [13]. The fractionalization approach in FQHE became a key point in spin-liquids, where excitations (spinons) in certain QSL's are regarded as fractionalized quasiparticles [47]. In contrast to FQHE where a high magnetic field is necessary for charge fractionalization, some frustrated lattice models in 2D and 3D predict charge fractionalization in the absence of magnetic field at low-temperature [48][49].

Research into the field of quantum spin-liquid got a tremendous boost after Anderson proposed that the normal state of high-temperature superconductors is a RVB state. Motivated by Anderson and Ramirez [50][51], the idea that frustration can lead to the Quantum spin-liquid (QSL) state has become an intense field of research from last four decades because of the variety of exciting phenomenon like-fractional low energy spinon excitation [47][52][53], massive electron spin entanglement, and coherent quantum fluctuations giving rise to topological order (topological excitations) [44],[54].

Several connected, but slight different definitions for a spin liquid can be written:

1- A spin liquid is a state without any spontaneously broken (local) symmetry, i.e. there is no long-range ordering down to absolute zero temperature. It is the simplest definition which doesn't refer to excitations of spin-liquids.

2- A spin liquid is a state without any spontaneously broken (local) symmetry, with a half-odd-integer spin in the unit cell.

3- A QSL is a state without any spontaneous symmetry breaking at zero temperature, with decaying spin correlations, $<S_i.S_j> \rightarrow 0$ for $\mid r_i - r_j \mid \rightarrow \infty$, and with fractional excitations [24].

The experimental verification of QSL state is a difficult and challenging task because of unavailability of any single probe by which we can confirm the QSL state. X-ray scattering, neutron scattering, magnetic susceptibility measurements, Nuclear magnetic resonance (NMR), muon spin relaxation (μSR) are all measurements that are geared towards looking for an order. Quasi-two-dimensional kagome quantum magnet Herbertsmithite $ZnCu_3(OH)_6Cl_2$ [48][55][56][61], triangular lattice organic magnets $EtMe_3Sb[Pd(dmit)_2]_2$ [28][35][57] and κ-(BEDT-TTF)$_2$Cu$_2$(CN)$_3$ [30][58] are the most prominent candidates for spin-liquid state. In NMR, μSR, Neutron scattering and magnetic measurements, these three prominent materials don't show any long-range magnetic ordering down to 50 mK. The absence of long-range order alone is not evidence for a spin-liquid state. We need to investigate the spinon excitation spectra expected for the spin liquid state [47][55]. Broad characteristic spectra of fractionalization have also been predicted [59] and observed in other two and three-dimensional candidate QSL materials [53][55]. The spin gap is an important physical quantity to characterize the spin liquid behavior. Whether the S = 1/2 kagome-lattice antiferromagnet is gapless or has a finite spin gap, is still an unsolved issue. Recently developed numerical calculation methods are not accurate enough to determine the gap in the thermodynamic limit [57][60][62][74].

1.1.3.1 Spin-liquid state in kagome antiferromagnets

Two-dimensional (2-D) kagome lattice with quantum magnets hosts a wide range of physical states at zero temperature ranging from classical ordering to Valence-Bond Solids (VBS) and spin-liquids. It displays both frustration and low-dimensionality which work against the spin-order. Further, S = 1/2 Heisenberg antiferromagnet on the kagome lattice is a good candidate for a two-dimensional quantum spin-liquid. In 2-dimensional systems, very few exact results exist and the application of approximate methods have become crucial to their understanding. A complete picture of their ground state behavior is still a matter of active research. The kagome lattice antiferromagnet gained attention after the discovery of some new spin-liquid materials as it shows the break down of spin-wave analysis to the lack of spin-order. The best quantum spin-liquid candidate material herbertsmithite $ZnCu_3(OH)_6Cl_2$ [48][55][56][61][78], vesignieite $BaCu_3V_2O_8(OH)_2$ [63], and volborthite [75] belong to the kagome lattice family. Thus a large number of theoretical model studies have been done on antiferromagnetic kagome lattices [64][65]. In contrast to the frustrated triangular lattice, where the nearest neighbor Ising model calculations provided the degenerate ground state with spin entropy per site ≈ 0.323 [27], kagome lattice shows disorder at all temperature with higher spin entropy per site $\approx$ 0.502 [64][65].

1.1.3.2 Spin-liquid state in hyperkagome antiferromagnets

The hyperkagome lattice is a unique lattice which gives us the opportunity to understand the comparative behavior of frustration and thermal energy in 3-dimensions. The iridate material $Na_4Ir_3O_8$ is a rare example of a hyperkagome lattice with effective S = 1/2. Magnetic measurements on $Na_4Ir_3O_8$ shows a high Curie-Weiss constant $\theta \approx$ -650 K while microscopic probes like μSR and neutron scattering measurements have shown the absence of long-range magnetic order on polycrystalline samples down to T = 50 mK, although $Na_4Ir_3O_8$ develops a static spin glass ground state around T $\approx$ 6 K most likely driven by disorder [66].

The true ground state of $Na_4Ir_3O_8$ is still an open question. On one side the spectroscopic results like NMR and μSR, showed a symmetry breaking to the fully frozen state at $T_f \approx 6$ K [66][67]. On the other side, the thermal conductivity and magnetic specific heat show neither a peak nor a steep increase at the respective temperature. Instead, the specific heat has a small T-linear and a sizable T-squared contribution while the thermal conductivity has a vanishingly small T-linear term [68][69]. The T-linear term usually arises from gapless spinon excitations whereas the T-squared term may be ascribed to a pairing gap formation or unusual excitations pertaining to a Kagome lattice. There are predictions of both (Bosonic or Fermionic) spin-liquid ground state and magnetically ordered states. As far as low-energy excitations are concerned, proposals for both a gapless or gapped state have been made[70][71].

From an experimental point of view, synthesizing a QSL compound in higher dimension is a long-standing problem and has been attracting plenty of interest recently. The unavailability of a unique single probe for the confirmation of QSL state makes the experimental realization of QSL more difficult and challenging. The magnetic measurements show the absence of a long-range ordering in a material[51]. Only the absence of a long-range magnetic order is not sufficient to conclude that the material has a spin-liquid state. Further microscopic measurements: muon spin relaxation (μSR), nuclear magnetic resonance (NMR), and neutron scattering measurements became the essential tools for investigating the spinon excitations spectra expected for the QSL state.

1.2 Structure of the thesis

In this thesis, two 3-D quantum magnets $Na_4Ir_3O_8$ and $Ca_{10}Cr_7O_{28}$ with spin-liquid properties were investigated. The main focus was to study the evolution of the magnetic properties of hyperkagome lattice compound $Na_4Ir_3O_8$ and kagome bilayer Ca_{10} Cr_7O_{28} in response to various perturbations like magnetic field, and magnetic/non-magnetic doping. In addition, this thesis also includes the evolution of magnetic properties of $Ca_{10}Cr_7O_{28}$ under high pressure (P = 1 GPa). This thesis is structured as follows :

Chapter 1 introduces an overview of the QSL state. We start by briefly introducing the Fermi-Liquid theory (FL) and Landau symmetry-breaking theory followed by the effects of geometrical frustration in the Mott insulating magnets. The mechanism of highly frustrated systems go beyond the FL theory and nowadays the condensed matter community is very much interested in looking for the physical realization of these materials. This introductory chapter gives some background of debates about the true physical ground states of frustrated spin systems.

In **Chapter 2** we present material synthesis details and briefly summarise the various experimental setups for bulk characterization of samples studied in this thesis.

Chapter 3 presents a comprehensive study of the effect of hole doping in $Na_4Ir_3O_8$, which is proposed as a rare 3-dimensional S = 1/2 QSL candidate material. Magnetic measurements on $Na_4Ir_3O_8$ shows a large Curie-Weiss constant $\approx$ -650 K. The microscopic μSR and neutron scattering measurements have shown the absence of long-range magnetic order on polycrystalline samples down to T = 20 mK, although $Na_4Ir_3O_8$ develops a static spin-glass ground state around T $\approx$ 6K. Theories about $Na_4Ir_3O_8$ predict either Bosonic or Fermionic spin-liquid ground states. As far as low-energy excitations are concerned, proposals for both a gapped or gapless state have been made. Our study on hole doped polycrystalline material $Na_{4-x}Ir_3O_8$ (x $\approx$ 0, 0.1, 0.3, and 0.7) allowed us to understand in more detail the robustness of QSL like features against the large removal of Na from the lattice. Another distinct aspect of hole doped $Na_{4-x}Ir_3O_8$ is that the undoped Mott-insulator $Na_4Ir_3O_8$ can be tuned away to a (semi) metallic state by controlling Na deficiency x.

Chapter 4 addresses the evolution of magnetic properties of the electron-doped $Na_4(Ir_{1-x}Ru_x)_3O_8$ (x $\approx$ 0, 0.05, 0.1, 0.2, and 0.3) and non-magnetic Ti^{4+} doped $Na_4Ir_{2.7}$ $Ti_{0.3}O_8$, with the motivation of studying a bond-disordered QSL state and tuning the system from classical to quantum spin system by partially replacing Ru^{4+} (S = 1) in place of Ir^{4+} (S = 1/2). In this chapter, the focus is on the comprehensive study of bulk characterisation of electron dopped $Na_4Ir_3O_8$. We track the variation in Curie-Weiss temperature and spin-glass transition with the doping concentration x. In contrast to the hole-doping, the electron-doped materials $Na_4(Ir_{1-x}Ru_x)_3O_8$ (x $\approx$ 0, 0.05, 0.1, 0.2, and 0.3) shows the possibility of tuning of spin-glassy temperature and magnetic heat capacity peak with doping concentration x. The power law behavior in C_{mag} versus temperature in our results supports in the fermionic ground state in doped materials. On the other hand, for nonmagnetic Ti substitution we find that Curie-Weiss temperature, frozen spin-glass transition become smaller and the anomaly in magnetic heat capacity C_{mag} is completely suppressed. In addition, introducing non-magnetic Ti leads to the creation of orphan spins (5% Ir), which show up in the low-temperature magnetic susceptibility.

In **Chapter 5** we study the evolution of low-temperature properties of $Ca_{10}Cr_7O_{28}$ with hydrostatic pressure and negative chemical pressure. Frustrated lattices with antiferromagnetic exchange are considered as an essential ingredient for QSL. The kagome bilayer compound $Ca_{10}Cr_7O_{28}$ provides a new direction in the field of QSL, where dominant ferromagnetic interactions within the kagome bilayer are responsible for the QSL state. This kagome bilayer compound develops a novel frustration mechanism where it is believed that competing ferro and antiferromagnetic exchange interactions suppress long-range magnetic order. Our high-pressure magnetic measurements up to $P \approx$ 1.3 GPa reveal that the spin-liquid state at ambient pressure is quite robust and may not depend on a delicate balance between any specific values of competing exchange interactions. The work of the substitution of non-magnetic S = 0, V^{5+} ions in $Ca_{10}(Cr_{1-x}V_x)_7O_{28}$ ($0 \leq x \leq 0.5$) leads to an interacting network of Chromium(Cr^{5+}-Cr^{6+})-V^{5+} moments within the kagome bilayer. This chapter also include the first time experimental realization of a perfect nonmagnetic analog $Ca_{10}V_7O_{27.5}$ of $Ca_{10}Cr_7O_{28}$, which enables an accurate exclusion of the lattice heat capacities without any fitting. Such an advantage is absent in the previous reports on $\mathrm{Ca_{10}Cr_7O_{28}}$. The systematic investigation of magnetic susceptibility and heat capacity analysis of $\mathrm{Ca_{10}(Cr_{1-x}V_x)_7O_{28}}$ ($0 \leq$ x ≤ 0.5), shows the absence of any long-ranged magnetic ordering down to 2 K. Magnetic heat capacity analysis of this diluted spin system reveals a gradual removal of magnetic entropy over an extended range of temperatures up to 40 K.

Finally, I will summarize the main results which have come out of this work in **Chapter 6**.

Chapter 2

Materials and Methods

In this chapter, we give a detailed account of the synthesis and experimental techniques used. This chapter is organised into two sections. The first section addresses the crystal-growth of polycrystalline samples $Na_{4-x}Ir_3O_8$ (x $\approx$ 0, 0.1, 0.3 and 0.7), $Na_4(Ir_{1-x}Ru_x)O_8$ (x $\approx$ 0, 0.05, 0.1, and 0.3), $Ca_{10}(Cr_{1-x}V_x)_7O_{28}$ ($0 \leq x \leq 0.5$), and $Ca_{10}V_7O_{27.5}$ followed by brief discussion of the measurement techniques used for physical characterisation of these materials.

2.0.1 Sample Preparation

All the polycrystalline samples were synthesized from the solid-state reaction method which is the most widely technique used to synthesize materials. It involves a diffusion limited reaction which requires high temperature for the components of a mixture to react [79][80][81]. The various steps we used for our materials are as follows. For proper mixing, we mixed the solid reactants thoroughly in agate mortar and pestle for 1 hour. After the mixing, 5 bar pressure has been used to make a hard pellet of the mixture. The right choice of container/crucible is one of the most important point during the solid state growth. One should know the reactivity between the container and the reagents beforehand. Based upon this, the environment and crucibles are chosen. Generally, for our materials, we have used alumina crucibles. At the last stage of sample synthesis, the mixed materials/pellets have to be given high-temperature heat treatments for several days with intermediate grinding.

For the synthesis of all materials, high-purity (99.99 %) starting materials (Alfa

Figure 2.1: Tabletop muffle furnaces used for heat treatments of the samples.

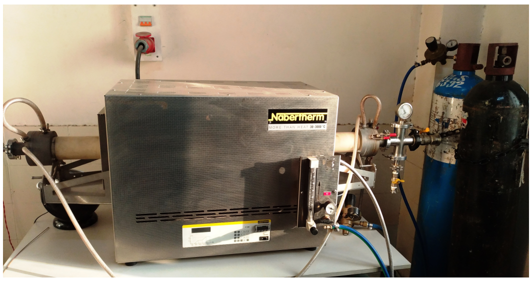

Figure 2.2: Tube furnaces used for heating treatment of the samples in vacuum or argon/ oxygen.

Aesar) were used. The stoichiometric mixture were mixed by a mortar-pestel and the 25-ton hydraulic press by Kimaya engineers was used for making the sample pellets. For the heat treatment of different samples, two types of high-temperature table top furnaces were used which are shown in Fig.-2.1 and Fig.-2.2 respectively. The tube furnace is used for heating the samples in vacuum, argon or oxygen environment. In the next part, we give the detailed procedure and heat profiles for synthesis of samples discussed in this thesis.

2.0.1.1 $Na_4Ir_3O_8$ and doped $Na_{4-x}Ir_3O_8$ Polycrystals

Polycrystalline samples of $Na_{4-x}Ir_3O_8$ (x $\approx$ 0, 0.1, 0.3 and 0.7) were prepared by starting materials Na_2CO_3 and Ir metal powder. Starting materials were mixed in amounts appropriate for a given x and heated in the air inside covered alumina crucibles (Alfa Aesar) at 750 °C for 24 h for calcination. The resulting black powders were thoroughly ground and mixed, and pressed into pellets and given two heat treatments at 985°C and 1000°C for 16 h each with an intermediate grinding and pelletizing step. The material was finally quenched in the air after the final treatment. All materials were stored and handled in an inert gas glovebox (MBraun, argon, $H_2O < 0.1$ ppm, $O_2 < 0.1$ ppm) which is shown in Fig:2.3.

2.0.1.2 $Na_4(Ir_{1-x}Ru_x)_3O_8$ Polycrystals

Polycrystalline samples of $Na_4(Ir_{1-x}Ru_x)_3O_8$ (x = 0.05, 0.1, 0.2 and 0.3) were synthesized from mixtures of Na_2CO_3, Ir and Ru (99.99 % -Alfa Aesar) metal powders. Stoichiometric amounts of the high-purity starting ingredients were mixed thoroughly

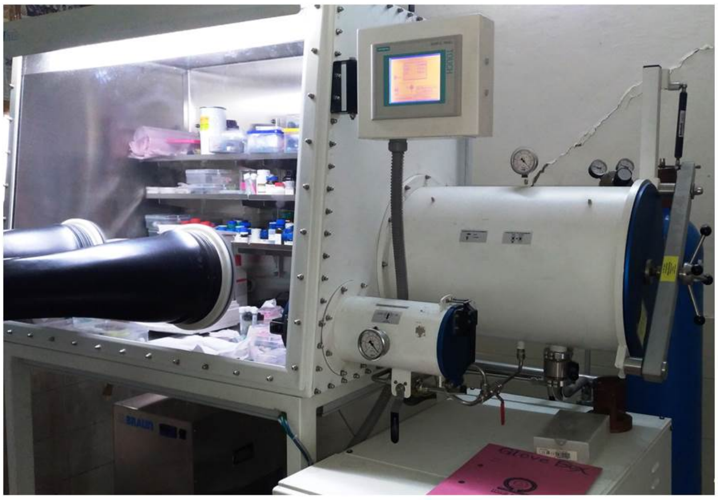

Figure 2.3: Glove-box with a very high purity inert (argon) atmosphere.

and loaded into alumina crucibles with a lid. These mixtures were first calcined at 750 °C for 22 hrs. The resulting mixtures were ground and pressed into a pellet (10 mm) and subsequently heated twice at 975 °C for 35 hrs in oxygen in a tube furnace with an intermediate grinding and pelletizing step. An oxygen environment was necessary to make sure the Ru stabilizes in the Ru^{4+} valance state.

2.0.1.3 $Ca_{10}Cr_7O_{28}$ and $Ca_{10}(Cr_{1-x}V_x)_7O_{28}$ Polycrystals

Polycrystalline samples of $Ca_{10}Cr_7O_{28}$, and vanadium doped $Ca_{10}(Cr_{1-x}V_x)_7O_{28}$ ($0 \leq x \leq 0.5$) were prepared by solid-state synthesis. The starting materials $CaCO_3$ (99.99 %, Alfa Aesar) and Cr_2O_3 (99.99 %, Alfa Aesar) were taken to make the Ca:Cr/Cr+V ratio 10.5 : 7 and mixed thoroughly in an agate mortar and pelletized. The pellet was placed in a covered Al_2O_3 crucible, heated in air at 750 °C for 24 h for calcination and then heated to 1000 °C for 48 h, and then quenched in Argon to room temperature. After the initial heat treatment, the material was reground and pressed into a pellet and given two heat treatments of 24 h each at 1100 °C, with an intermediate grinding and pelletizing step. The pellet was always brought to room temperature by quenching in Argon. Hard well sintered dark green pellets were obtained.

2.0.1.4 $Ca_{10}V_7O_{27.5}$ Polycrystals

The first experimental realization of non-magnetic analog $Ca_{10}V_7O_{27.5}$ of QSL $Ca_{10}Cr_7O_{28}$ is also discussed in this thesis. The polycrystalline samples of $Ca_{10}V_7O_{27.5}$ has been grown by the similar initial heat profile (750 °C for 24 h) of $Ca_{10}Cr_7O_{28}$ as we discussed in the previous subsection section. Despite two high-temperature heat treatments at 1150 °C a brittle pellet was obtained.

2.0.2 Structure characterization : X-ray diffraction

For confirming the phase purity of the polycrystalline samples we have used the Rigaku Ultima IV fully automatic high-resolution X-ray diffractometer system at the X-ray Facility of IISER Mohali. The radiation used for X-ray was from a Cu target. During our measurements we have used the angular range from 5° to 90° in the steps of 0.02 with the angular rate 3° per minute.

The analysis of PXRD data by Rietveld refinement was carried out by the GSAS software. The International Centre for Diffraction Database-ICDD PDF-4 was also used for searching the different possible phases.

2.0.3 Bulk property measurements

For most of the bulk measurements, we have used a commercial Quantum Design physical property measurement system (QD-PPMS) which is shown in Fig: 2.4. This PPMS is equipped with a 9 T magnet and can measure magnetisation with a temperature range between 1.8 and 400 K [82]. The different PPMS probes used for various physical property measurements are explained in their respective sections as below.

2.0.3.1 Electrical transport

For electrical transport, four probe resistivity option in PPMS was used. The schematic diagram of four probe resistivity measurement, where out of four lead contacts, two outer ones were used as current leads, and the two inner ones were used as voltage leads to measure the potential difference across the sample as shown in Fig- 2.5. All the measurements were done on bar-shaped polycrystalline materials mounted on the

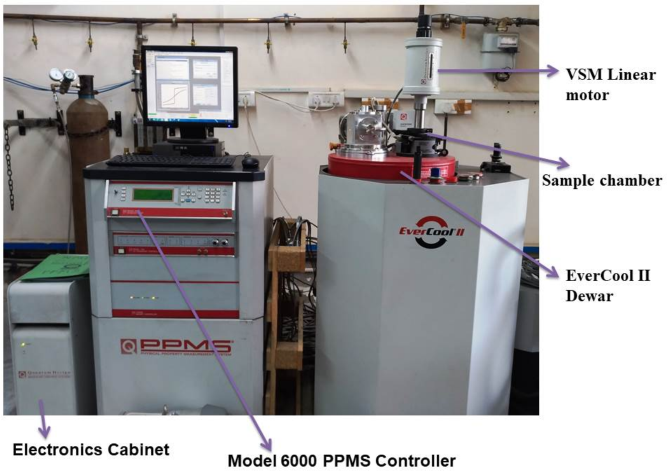

Figure 2.4: 9 T Quantum Design Physical Property Measurement System(PPMS).

standard resistivity puck. The resistivity ρ of the sample is obtained from a voltage V measurement at constant current I using the Ohm's law:

$$\rho = \frac{VA}{IL} \tag{2.1}$$

Here A is the cross-sectional area of the sample through which current passes, and L is the distance between the two voltage leads.

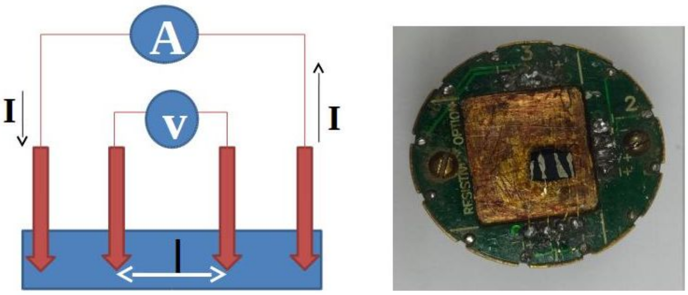

Figure 2.5: Left: A schematic view of four probe measurement. Right: sample mounted on resistivity puck.

2.0.3.2 Magnetic measurement

DC or static Magnetometry

DC magnetic susceptibility measurements determine the equilibrium value of the magnetisation in a sample. A constant magnetic field magnetizes the sample and the magnetic moment of the sample is measured M(H) . The magnetic susceptibility is then defined as:

$$\chi_{dc} = M/H_{dc} \tag{2.2}$$

The low-temperature magnetic measurements down to T = 2 K were done by the Vibrating Sample Magnetometer (VSM) option of the QD-PPMS. In a VSM magnetic properties of materials are measured as a function of applied magnetic field H, temperature T, and time t. The operation principle of the VSM is that a changing magnetic flux will induce a voltage in a pickup coil. For vibrating the sample and detecting the change in the magnetic flux, QD-PPMS have a sensitive DC magnetometer, build with a VSM linear motor transport (head) and compact gradiometer pickup coil for detection, which is shown in Fig:-2.6(a) and (b). Fig:-2.4 shows the VSM linear motor transport (head) attached on the sample chamber of PPMS. The sample is attached with the help of GE varnish to the end of a brass trough (sample tube) that is driven sinusoidally. This sample mounting brass trough is made from cartridge brass tubing with a cobalt-hardened gold plating finish and is shown in Fig-2.6(c). The magnetisation of brass sample holder is in the order of -10^{-6} emu, which is very small as compared to our samples (10^{-3} emu). The oscillation center of the sample is positioned at the vertical center of a gradiometer pickup coil. The voltage induced in the pickup coil is amplified and lock-in detected in the VSM detection module [83].

The time-dependent induced voltage in VSM option of the PPMS follows the equation

$$V_{coil} = \frac{d\phi}{dt} = \frac{d\phi}{dz}\frac{dz}{dt} \tag{2.3}$$

Here ϕ is the magnetic flux enclosed by the pickup coil, z is the vertical position of the sample with respect to the coil, and t is time. This VSM linear motor is designed to operate at 40 Hz with a relatively large oscillation amplitude (1-3 mm peak) and a frequency of 40 Hz, the system can resolve magnetisation changes of less than 10^{-6} emu at a data rate of 1 Hz [83].

AC Magnetometry

AC susceptibility (χ_{ac}) is a sensitive tool for characterising various states of matter, especially spin-glass, superparamagnetic state and superconductors [23][76][77]. One advantage of the AC measurement is that it can detect small magnetic changes even

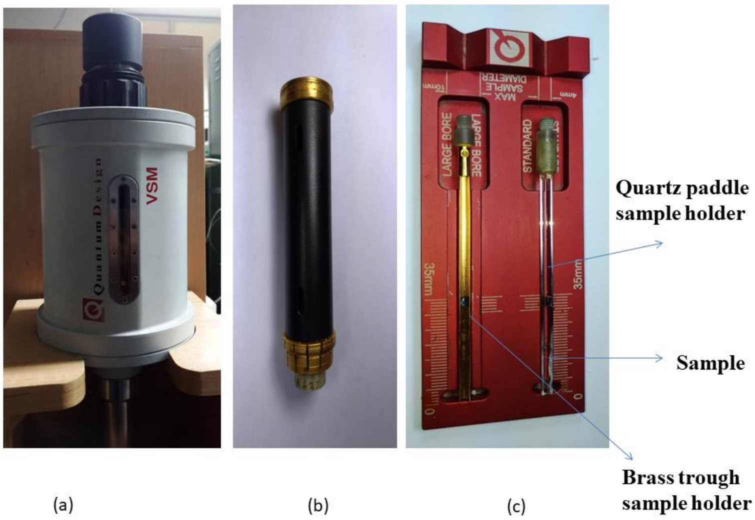

Figure 2.6: For PPMS VSM option- (a) VSM linear motor transport (head) for vibrating the sample (b) Compact gradiometer pickup coil for magnetic flux detection, and (c) the quartz tube and brass tube sample holders for VSM measurement.

when the absolute moment is large. It is a dynamic measurement technique, which gives the differential response (dM/dH) of the magnetisation (M) of the sample to an oscillating magnetic field H. In contrast to the DC or static magnetic measurement, where the magnetic moment of the sample doesn't change with time, in AC or dynamic magnetic measurement the magnetic moment of the sample is changing with applied ac frequency f[84].

In AC magnetic measurements, a small AC drive magnetic field is superimposed on the DC field, causing a time-dependent moment in the sample. Similar to DC magnetometer, an AC susceptometer uses a detection coil to detect changes in the magnetic flux due to the sample. The field of the time-dependent moment induces a current in the pickup coils, allowing measurement without sample motion. So the measured χ_{ac} becomes a complex value and written in terms of real part (χ') and imaginary part (χ") of susceptibility as

$$\chi_{ac} = \chi' - i\chi'' \tag{2.4}$$

AC measurements are sensitive by up to three orders of magnitude compared to a DC measurement. A DC field in addition to the AC drive helps increase the absolute moment and make it easier to measure weakly magnetic samples. We have measured

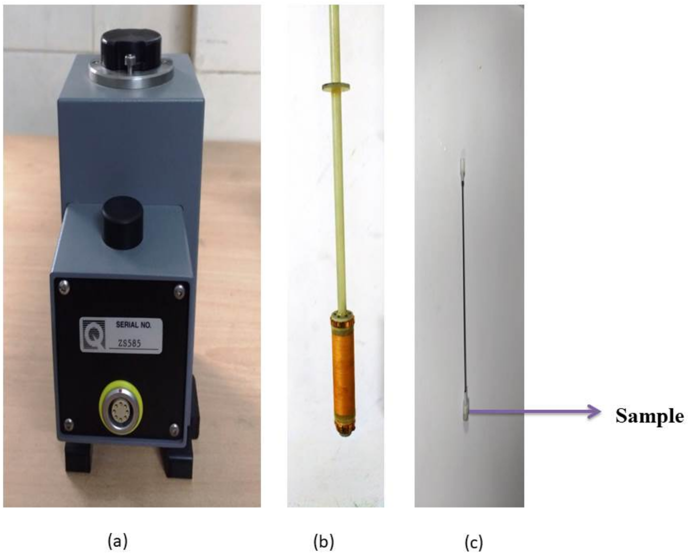

Figure 2.7: (a) ACMS insert houses the ACMS drive and detection coils and all electrical connections for χ_{ac} measurement. (b) ACMS drive coil set. (c) Sample holder for ACMS measurement.

the AC susceptibility for $Na_4Ir_3O_8$ samples by applying a low amplitude of the ac field (10 Oe) and varying frequency in the range 10-10000 Hz.

2.0.3.3 Heat capacity

Heat capacity measurements provide information on the structural, electronic and magnetic properties of a material. They give useful information about the presence of any phase transitions which appear as anomalies in the heat capacity from which the nature of the phase transitions can be identified.

The heat capacity option in QD-PPMS measures heat capacity at constant pressure C_P. During the measurement, a known amount of heat at a constant power is applied for a fixed time by a platform heater. A schematic of the heat capacity experimental setup shown in the right side of the Fig: 2.8. The heat capacity measurement uses a relaxation technique in which the heating period is followed by a cooling period of the same duration (measurement cycle).

For this purpose, the sample is placed on a platform which is connected with a weak thermal link to a constant temperature bath (puck), at a temperature T_0 a small amount of heat raises the temperature of the sample by T (typically T_0 /T $\approx$ 1%) and then it decays exponentially down to the puck temperature[85]. The exponentially decaying temperature of the sample T$_s$ is given by

$$T_s = T_0 + \Delta T exp(t/\tau_1) \tag{2.5}$$

where t is the time and τ_1 is sample to bath relaxation time constant. The heat capacity C is determined from the measurement of τ_1 and the known thermal conductivity κ of the weak thermal link as

$$C = \tau_1 \kappa \tag{2.6}$$

The sample is mounted on the calorimeter puck with the help of m-grease supplied by the Quantum Design as shown in the left part of Fig-2.8. This sample puck has a resistive platform heater and platform thermometer attached to the bottom side of a calorimeter chip that functions as the sample platform as shown in the Fig-2.8. A precision current source provides the AC excitation for reading the platform thermometer while a high-precision, high-accuracy analog to digital converter (ADC) reads the voltage across the thermometer. The integrated vacuum system in the cryostat provides a sufficient vacuum (0.01 mTorr) so that the conductance of the wires dominates the total thermal conductance between the sample platform and the puck. This gives a

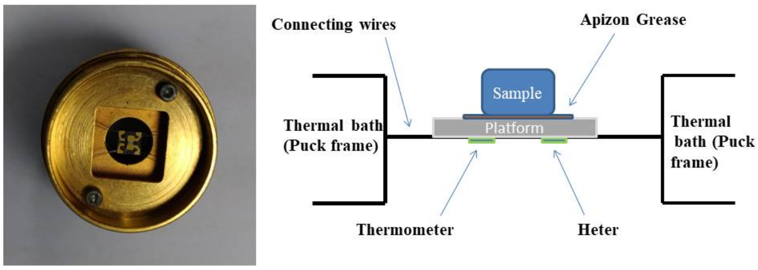

Figure 2.8: Heat capacity puck (left one) and its schematic of the experimental setup shown in right side.

.

reproducible heat link to the bath with a corresponding time constant large enough to allow both the platform and sample to achieve sufficient thermal equilibrium during the measurement[85].

Each heat capacity measurement contains the two consecutive measurements first the background (m grease) called addenda measurement followed by the sample with grease measurement. The final sample heat capacity of the sample is obtained by subtracting the addenda measurement from total heat capacity.

Chapter 3

Hole doped quantum spin-liquid $Na_{4-x}Ir_3O_8$ (x ≈ 0, 0.1, 0.3 and 0.7)

3.1 Introduction

After Anderson's prediction of the "Resonating Valance Bond (RVB)" state as the ground state of the parent compounds of the high-temperature cuprate superconductors, Quantum Spin-Liquids (QSL's) have attracted much attention[26, 51]. A lot of effort has been put in tuning the QSL state including high-pressure measurements and carrier doping . These are expected to stabalize superconducting or metallic states with unconventional magnetic excitations [93][100]. We have seen examples of 1T - TaS_2, Li - doped Herbertsmithite $ZnLi_xCu_3(OH)_6Cl_2$, and $Na_4Ir_3O_8$ (theoretical results) like Kagome spin-liquid candidate systems, where impurities/disorder play a critical role and the induced spin-states destroy the spin liquid behavior of the system [86][87][94].

The initial motivation of our experimental work on $Na_{4-x}Ir_3O_8$ (x $\approx$ 0, 0.1, 0.3 and 0.7) was to produce nearby magnetic states of $Na_4Ir_3O_8$. The previous experiments conducted by Okamoto (2007), on parent compound $Na_4Ir_3O_8$ strongly suggested it as a first unique case of three-dimensional QSL compound. The high degree of frustration in $Na_4Ir_3O_8$ was realized by the magnetic measurements, which showed antiferromagnetically coupled spin S = 1/2 on hyperkagome Ir lattice with Curie-Weiss temperature $\theta \approx$ -650 K [66][68]. The absence of any long-range ordering down to 10 mK was confirmed by the neutron diffraction measurements and muon spin rotation (μSR) measurments[66] [68][72]. However, a spin glassy state around temperature

6 K was observed [66][68].

Our detailed study of hole doped samples of $Na_{4-x}Ir_3O_8$ (x ≈ 0, 0.1, 0.3 and 0.7) allowed us to understand in more detail the robustness of the QSL-like state in the parent material against the large removal of Na from the lattice. In $Na_{4-x}Ir_3O_8$ we were able to tune the Mott insulator state of $Na_4Ir_3O_8$ continuously to a (semi)metallic state by controlling Na deficiency 'x' .

3.2 Results and discussion

3.2.1 Structure Analysis

The parent compound $Na_4Ir_3O_8$ has a structure related to a spinel oxide AB_2O_4 structure. Okamoto suggested that it can be rewritten as the $(Na_{1.5})_1(Ir_{3/4}, Na_{1/4})_2O_4$, where B - sublattice is Pyrochlore lattice [66]. From the rewritten spinel - based chemical formula, it is evident that each tetrahedron in the B - sublattice is occupied by three Ir and one Na, constituting a 3-Dimensional analog of 2 - dimensional kagome lattice. Due to the low spin value and high frustration, the hyperkagome lattice of $Na_4Ir_3O_8$ turns out a rare 3 - dimensional strongly frustrated lattice. This hyperkagome lattice is a cubic-one with 12 sites per unit cell and corresponds to one of two chiral space groups $P4_132$ or $P4_332$ as shown in Fig.-3.1(a), (c) and (d). In this thesis, we have used the space group $P4_132$ for crystal structure refinement [66][68].

The crystal structure of sodium doped $Na_{4-x}Ir_3O_8$ (x ≈ 0, 0.1, 0.3 and 0.7) were confirmed by powder X-ray diffraction (PXRD) which shows a similar peak pattern with the $Na_4Ir_3O_8$. Fig-3.2 shows room temperature PXRD patterns for three representative samples $Na_{4-x}Ir_3O_8$ (x = 0, 0.3, 0.7). The solid (red) curves in the data are the results obtained from two phase Rietveld refinement with cubic symmetry and space group $P4_132$ by using GSAS software. The parameters obtained from the Rietveld refinements are listed in Table-3.1. All samples were found to have the majority phase of $Na_4Ir_3O_8$.

The only impurity phase found in the samples was a small amount of IrO_2 (θ = 28° and 54°). The position of the most intense IrO_2 reflection at θ = 28° is marked with an $*$ in the XRD patterns shown in Fig-3.2. The approximate amount of IrO_2 in each sample is also listed in Table-3.1. From Table-3.1, we didn't find any significant

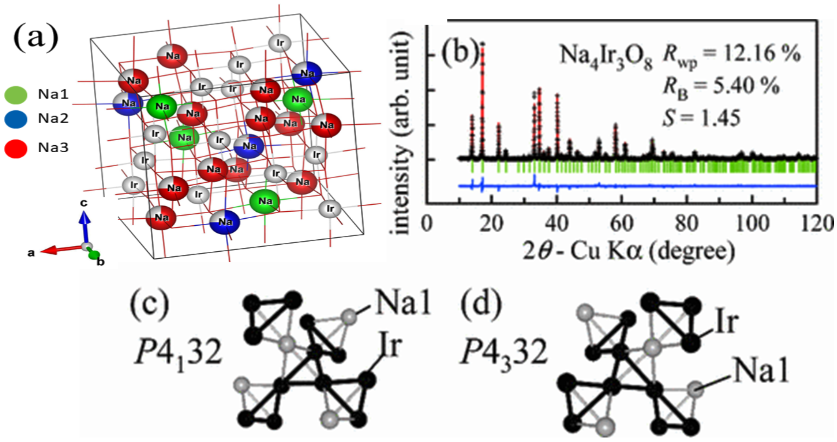

Figure 3.1: (a) Crystal structure of $Na_4Ir_3O_8$ with the space group $P4_132$. (b) The x-ray diffraction pattern of $Na_4Ir_3O_8$ at room temperature [Figure from ref. [66]]. (c) and (d) Hyperkagome Ir and Na sublattice derived from the structure of $Na_4Ir_3O_8$. These two structures with different chirality are indistinguishable by conventional x-ray diffraction, giving the identical result in refinement [Figure from ref. [66]] .

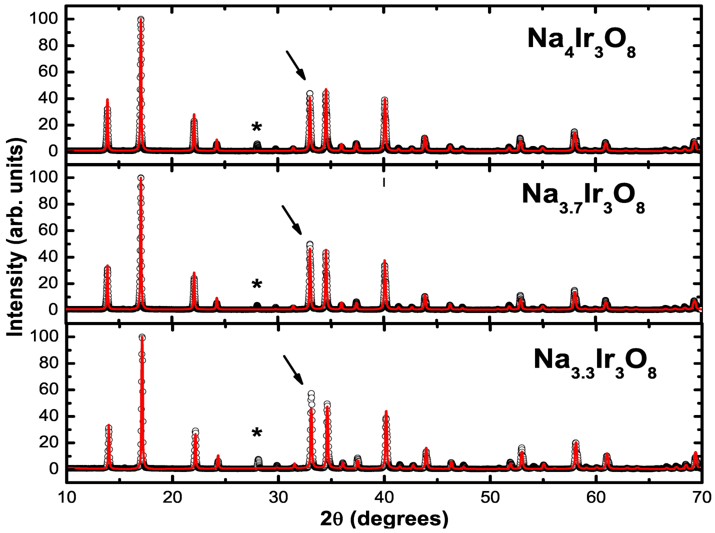

Figure 3.2: (Color online) Powder X-ray diffraction pattern for $Na_{4-x}Ir_3O_8$ (x = 0,0.3,0.7) materials (open symbols). The $*$ marks the position of the largest diffraction peak for the IrO_2 impurity phase found in the samples. The solid curve through the data is the Rietveld refinement. The arrow marks the position of the (311) reflection whose intensity increases with Na deficiency.

change in lattice parameter, with Na deficiency. The major difference was found in the occupation of the Na2 and Na3 sites. This reduction in occupation is expected and consistent with the Na deficiency in doped samples. Between these two Na sites, the occupancy of Na2 site reduces more in comparison to Na3. In the PXRD diffraction pattern, the only major change with increasing Na deficiency is the peak intensity of the (311) reflection which increases relative to the other X-ray reflections as indicated by an arrow in Fig-3.2.

Removing Na from $Na_4Ir_3O_8$ can in principle lead to a two-phase mixture of $Na_4Ir_3O_8$ and $Na_3Ir_3O_8$ [66] [90]. $Na_3Ir_3O_8$ has the very similar X-ray diffraction patterns as $Na_4Ir_3O_8$ as shown in Table-3.2. In contrast to $Na_4Ir_3O_8$ (Mott insulating state), $Na_3Ir_3O_8$ shows the semi-metallic behavior [90]. The main difference between the crystal structures of these two materials is the number of Na positions. $Na_4Ir_3O_8$ has three distinct Na sites while $Na_3Ir_3O_8$ has two. Only one of the Na site is common between the two structures as shown Table-3.1 and Table-3.2. The laboratory X-ray diffraction experiments was not able to distinguish a mixed phase sample from a single phase Na - deficient sample. For confirming the $Na_4Ir_3O_8$ phase purity, we have done the ^{23}Na NMR at room temperature (see the appendix - B). In the case of a mixture of two different phases of $Na_4Ir_3O_8$ and $Na_3Ir_3O_8$, there should be four peaks corresponding to four different Na positions in NMR. The observation of three Na response peaks in preliminary Na NMR measurements on our samples strongly suggests that our materials are predominantly single phase Na-deficient $Na_4Ir_3O_8$ [99].

Refinements of the powder diffraction patterns have shown that with increasing x, Na is progressively removed from the lattice. Additionally, we have found that Na is preferentially removed from the Na2(4b) site, which is not on the Ir tetrahedra (magnetic sublattice) and hence deficiency in this site is not expected to lead to disorder in the magnetic Ir sublattice as shown in Fig.-3.1. Therefore, the frustrated hyperkagome lattice of Ir moments is not disturbed with Na deficiency. This is probably why the strong magnetic frustration is robust under removal of fairly large amounts of Na. Na deficiency is however, expected to lead to hole doping of the system. It is therefore surprising that local - moment behavior and insulating behavior survives under hole doping. This is consistent with experiments on single crystals of $Na_{3+x}Ir_3O_8$, where it was found that for x = 0.6 (this would be x = 0.4 for our samples) the material was insulating [90].

Table 3.1: Structural parameters obtained from a Rietveld refinement of room temperature powder X - ray patterns shown in Fig-3.2 with space group 213, $P4_1 32$. We have used the standardized structural parameters. The unit cell coordinates in this notation are related to the earlier published unit cell by an origin shift of (1/2,1/2,1/2).

Atom	Wyck	x	y	z	Occ.	B Å^2
$Na_4Ir_3O_8$	a = 8.981(2)Å		$IrO_2 \approx 7$ %	χ^2= 1.248, R_{exp} = 7.43%; R_{wp} = 9.28%		
Ir	12d	1/8	0.141(3)	0.392(5)	1	0.4 (1)
Na1	4a	7/8	7/8	7/8	1	1.8 (6)
Na2	4b	3/8	3/8	3/8	0.71(1)	2.1 (4)
Na3	12d	1/8	0.883	0.131(2)	0.75	1.4 (8)
O1	8c	0.142(6)	x	x	1	0.9 (2)
O2	24e	0.124 (6)	0.315 (8)	0.352	1	1.3 (6)
$Na_{3.9}Ir_3O_8$	a = 8.981(2)Å		$IrO_2 \approx 4$ %	χ^2= 1.46, R_{exp} = 10.92%; R_{wp} = 15.94%		
Ir	12d	1/8	0.136(6)	0.385(6)	1	0.8(5)
Na1	4a	7/8	7/8	7/8	1	2.2 (1)
Na2	4b	3/8	3/8	3/8	0.68(1)	1.7 (3)
Na3	12d	1/8	0.684(3)	0.127(2)	0.73(2)	2.4(1)
O1	8c	0.105(6)	0.105 (5)	105 (3)	1	1.7 (5)
O2	24e	0.112 (6)	0.337(7)	0.337(5)	1	2.1 (3)
$Na_{3.7}Ir_3O_8$	a = 8.979(2)Å		$IrO_2 \approx 5$ % χ^2= 1.30, R_{exp} = 9.59%; R_{wp} = 12.46%			
Ir	12d	1/8	0.137(3)	0.383(4)	1	0.8(3)
Na1	4a	7/8	7/8	7/8	1	2.2 (1)
Na2	4b	3/8	3/8	3/8	0.64(1)	1.7 (3)
Na3	12d	1/8	0.686(4)	0.129(4)	0.70(2)	2.4(8
O1	8c	0.105(6)	0.105 (6)	105 (6)	1	1.7 (7)
O2	24e	0.112 (6)	0.335(8)	0.337(4)	1	2.1 (3)
$Na_{3.3}Ir_3O_8$	a = 8.980(2)Å		$IrO_2 \approx 6$ %	χ^2= 1.28, R_{exp} = 12.23%; R_{wp} = 15.65%		
Ir	12d	1/8	0.139(3)	0.386(4)	1	0.7(2)
Na1	4a	7/8	7/8	7/8	1	2.1 (2)
Na2	4b	3/8	3/8	3/8	0.36(3)	2.6 (4)
Na3	12d	1/8	0.876(4)	0.122(4)	0.64(2)	1.9(7)
O1	8c	0.105(6)	105 (6)	105 (6)	1	0.9 (3)
O2	24e	0.112 (6)	0.335(8)	0.337(4)	1	1.1 (4)

Table 3.2: Refined structural parameters of $Na_3Ir_3O_8$ with space group 213, $P4_1 32$. χ^2 = 1.28, R_{exp} = 4.35%, R_{wp} = 5.6%. [Ref. - [90]].

Atom	Wyck	x	y	z	Occ.	B Å^2
$Na_3Ir_3O_8$	a = 8.9857(4) Å					
Ir	12d	0.61264 (1)	x+1/4	5/8	1	0.00802
Na1	4b	7/8	7/8	7/8	1	0.0122
Na2	8c	0.2570(2)	x	x	1	0.0138
O1	8c	0.1144(2)	x	x	1	0.0105
O2	24e	0.1364(3)	0.9071(2)	0.9186(2)	1	0.0111

3.2.2 Electronic transport

The resistance R(T) divided by the resistance at T = 300 K value is shown in Fig-3.3 for the x = 0 and x = 0.7 samples. The T = 300 K resistivity values for the two samples are 41 and 16 mΩ cm, respectively. Both samples show a T dependence suggesting insulating behaviour.

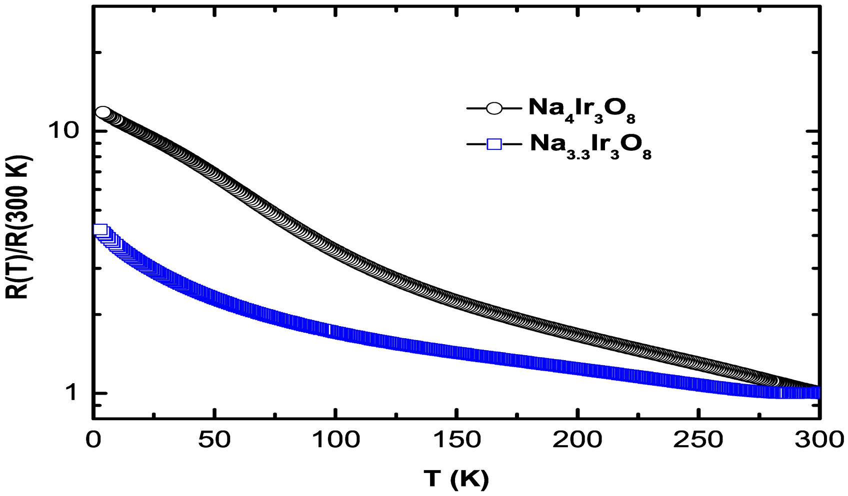

Figure 3.3: (Color online) Normalized resistance R(T)/R(300 K) versus T of $Na_{4-x}Ir_3O_8$ (x = 0, 0.7).

However, the values and magnitude of change of R with temperature suggest that the conductivity for the x = 0.7 sample is slightly enhanced compared to the parent x = 0 material. We note that the amount of IrO_2 phase in the x = 0 and x = 0.7 samples is approximately the same and hence conclusion made from a comparison of the resistivities of these two samples will not be affected by the presence of the impurity phase. The temperature dependence and room temperature value of the resistivity for our samples are similar to those reported for $Na_{3.6}Ir_3O_8$ single crystals [90]. For the x = 0.7 sample R(2 K)/R(300 K) ≈ 3.5 suggesting that this sample is close to being (semi)metallic. Both the magnetic susceptibility χ and heat capacity C for this sample support this conclusion.

3.2.3 Magnetic measurements

Fig-3.4(a) shows the magnetic susceptibility χ versus temperature T between T = 1.8 and 400 K for $Na_{4-x}Ir_3O_8$ (x $\approx$ 0, 0.1, 0.3, 0.7). To check the low - temperature spin - disorder induced glass state we have performed zero - field - cooled (ZFC) and field - cooled (FC) magnetic susceptibility χ measurement. Fig-3.4(b) shows the ZFC and FC magnetic susceptibility χ versus temperature T measured in a small magnetic field of H = 500 Oe for $Na_4Ir_3O_8$. The magnetic irreversibility (bifurcation) in the ZFC - FC data was found at T $\approx$ 6 K, suggesting the onset of a frozen spin - glass like state below this temperature. Similar low - temperature (low magnetic field) behaviors were observed for sodium deficient samples $Na_{4-x}Ir_3O_8$ (x $\approx$ 0.1, 0.3). This observation of magnetic irreversibility below T $\approx$ 6 K is consistent with previous reports of $Na_4Ir_3O_8$[66] [72].

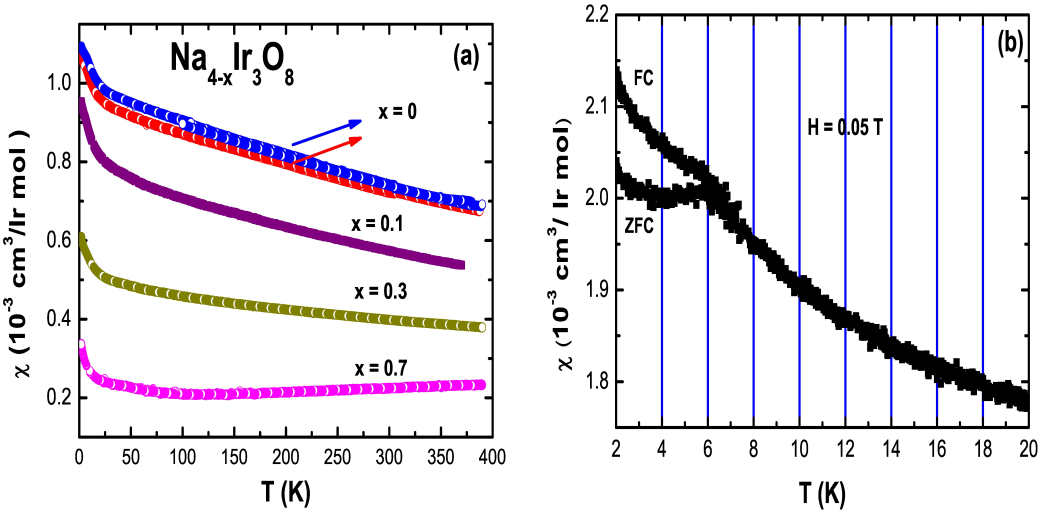

Figure 3.4: (a)(Color online) Magnetic susceptibility χ versus T of $Na_{4-x}Ir_3O_8$ (x = 0, 0.1, 0.3, 0.7) between T = 2 and 400 K. (b) Zero-field-cooled (ZFC) and field-cooled (FC) data measured in H = 500 Oe for the x = 0 parent compound.

We now discuss the high magnetic field susceptibility data shown in Fig-3.4(a). Data for two samples with x $\approx$ 0 are shown and are marked with arrows in Fig-3.4(a). Although the temperature dependence of these two samples is similar, one can already see a slight difference in the absolute magnitude of χ(T) for two samples with apparently the same Na content. When Na is intentionally removed the magnetic susceptibility χ drops in magnitude although the local moment behavior persists up to at least x $\approx$ 0.3. The high - temperature χ(T) (T $\geq$ 200 K) data were fit by the Curie-Weiss

Table 3.3: Parameters obtained from fits to the magnetic susceptibility data by the Curie - Weiss expression χ = χ_0 + C/T-θ.

x	χ_0 $\frac{10^{-5}cm^3}{Ir-mol}$	C $\frac{cm^3K}{Ir-mol}$	$\mu_{eff}(\mu_B)$	θ (K)
0	1.2 (1)	0.39(1)	1.77	-568(9)
0.1	1.4 (1)	0.36(2)	1.62	-512(6)
0.3	1.8 (6)	0.28(3)	1.5	-509(7)

expression χ = χ_0 + C /T-θ. The parameters obtained from Curie - Weiss fits to the data sets for the samples $Na_{4-x}Ir_3O_8$ (x = 0,0.1,0.3) are given in Table-3.3. The Curie constant C can be written in terms of the effective moment as, C = μ^2_{eff}/8. A clear monotonic decreases in the Curie constant C with increasing x is observed, suggesting a decrease in the effective magnetic moment per iridium in the Na deficient samples. The value of the effective magnetic moments estimated from C is also given in Table-3.3, which matches well with the expected values. Additionally, the Weiss temperature θ decreases slightly but stays large and negative indicating that strong antiferromagnetic interactions persist between the surviving local magnetic moments [97].

The magnetic susceptibility χ(T) behavior for the sample x = 0.7 shows qualitatively different behavior. The χ(T) is almost T independent except the low - temperature upturn which is seen for all samples. The T independent χ is similar to the behavior expected for a Pauli paramagnetic metal. It must be noted however, that χ actually shows a weak increase with T and thus it's not the behavior of a simple metal. This weak increase in χ(T) with increasing temperature is similar to what has been reported previously for $Na_3Ir_3O_8$ [66][72]. We believe, based on NMR evidence, that our x = 0.7 sample is a distinct chemical phase (see the appendix - I) [97].

3.2.4 Heat-capacity

To rule out long - range magnetic order, we have performed heat capacity measurements on $Na_4Ir_3O_8$ down to T = 100 mK. In Fig-3.5 we show the low - temperature magnetic heat capacity C_{mag} as a function of T for $Na_4Ir_3O_8$ measured at various magnetic fields H = 0, 5, 14 T between T = 100 mK and 2 K. To calculate the magnetic heat capacity, we have synthesized the nonmagnetic analog $Na_4Sn_3O_8$ of $Na_4Ir_3O_8$. The magnetic contribution C_{mag} of heat capacity was obtained by subtracting the heat capacity C(T) data of $Na_4Ir_3O_8$ (by corrected for the molar mass difference) from the data of non magnetic sample $Na_4Sn_3O_8$. The lattice heat capacity C(T) for $Na_4Sn_3O_8$ can be converted to the lattice C(T) for $Na_4Ir_3O_8$ by multiplying the temperature (T) for C(T) data of $Na_4Sn_3O_8$ by the factor (θ_D of $Na_4Ir_3O_8$ / θ_D of $Na_4Sn_3O_8$)$^{1/2}$, where θ_D is Debye temperature. A simple harmonic oscillator model predicts $\theta_D \propto$ (1/M)$^{1/2}$, where M is the molar mass of the compound. No lambda-like sharp transition was observed for any samples, which supports the absence of magnetic ordering or freezing down to the lowest temperatures measured. If the case: when the bulk of the sample goes into a frozen spin - glass state, then one would expect to see a broad anomaly at a temperature of roughly 1.5 - 2 times the temperature at which the anomaly in the magnetic measurement is seen. This would be around T $\approx$ 10 - 12 K for our samples with a magnetic anomaly at T$\approx$ 6 K. No such anomalies are observed in the heat capacity for any of our samples. The C_{mag} is also insensitive to applied magnetic fields up to H = 14 T as shown in Fig-3.5, which is the hallmark of frustrated magnets. The Fig-3.5 inset shows the zero field C_{mag}/T vs T between T = 100 mK and T = 4K.The data above T = 0.75K were fit by the expression C = γT + β T^n. We were able to obtain an excellent fit, shown as the solid curve through the data in the inset of Fig-3.5, with the values γ = 2.8(4) mJ/(K^2- mol-Ir), β = 3.4(2) mJ/mol K^4, and n = 2.38(3). The value of $\gamma \approx$ 2 mJ/(K^2 mol - Ir) and an exponent n between 2 and 3 is consistent with previous reports [66][68].

Below 0.6 K, an upturn in C_{mag}/T does not follow the 1/T^2 behavior expected for the high - temperature tail of a Schottky anomaly and is not field dependent. A similar upturn was seen for $Na_3Ir_3O_8$ and was suggested to arise from an impurity contribution [69]. The origin of this upturn for our sample is unknown at present.

We now present the evolution with doping of another notable feature of the parent material: the broad anomaly in the magnetic contribution to the heat capacity at around T $\approx$ 30 K [17,18]. Fig-3.6 shows the zero - field C_{mag}/T vs T for $Na_{4-x}Ir_3O_8$ (x = 0, 0.3, 0.7) between T = 2 K and T = 50 K. The broad anomaly observed earlier for the undoped sample persists in the Na - deficient samples as well. Although the magnitude of the anomaly decreases slightly, the maximum of the anomaly only reduces from $\approx$ 55 to about $\approx$ 42 mJ/molK^2. The position of this peak does not change. These

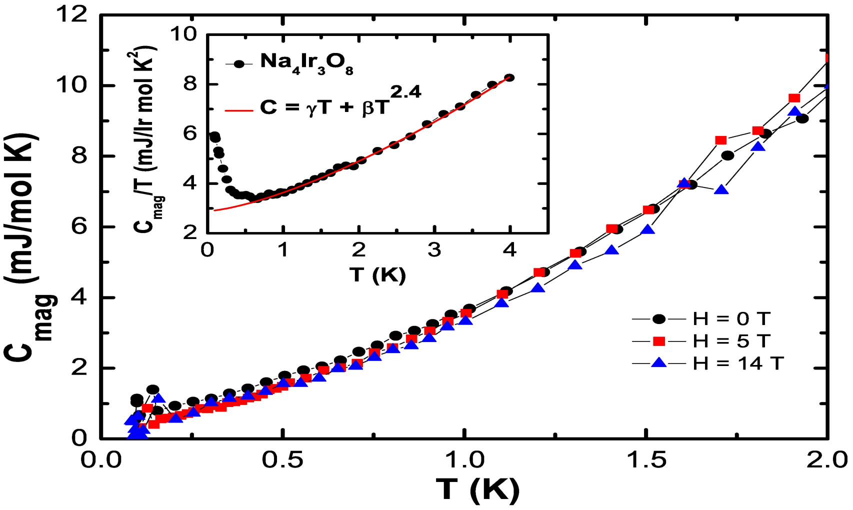

Figure 3.5: (Color online) Low - temperature magnetic heat capacity C_{mag} versus temperature T for the spin - liquid $Na_4Ir_3O_8$ between T = 100 mK and 2 K in magnetic fields H = 0, 5, 14 T. The inset shows the H = 0 data plotted as C_{mag}/T versus T. The data above T = 0.75 K were fit (shown as the solid red curve through the data) by the expression C = γT + βT^n.

observations suggest that the mechanism leading to the anomaly in $Na_4Ir_3O_8$ is also at work in the Na deficient samples. A simpler and disturbing possibility is that the anomaly in the magnetic heat capacity has nothing to do with the spin - liquid state but arises from an improper lattice subtraction. This could happen if $Na_4Sn_3O_8$ lattice does not have the same lattice heat capacity as $Na_4Ir_3O_8$.

Fig-3.6 inset shows the zero - field C_{mag}/T vs T^2 for $Na_{4-x}Ir_3O_8$ (x = 0, 0.3, 0.7) between T = 2 K and T = 10 K. The downward curvature of the data for $Na_4Ir_3O_8$ in this plot highlights the power - law dependence of C_{mag}(T) with an exponent between 2 and 3. This exponent increases for the Na deficient samples with the data at the lowest temperatures ($T < 5$ K) for the x = 0.7 sample $Na_{3.3}Ir_3O_8$ showing a more conventional T^3 behavior. It is also evident that C_{mag}/T for all samples extrapolate to similar T = 0 values of $\gamma \approx 2$ to 3 mJ/(Ir molK^2).

3.3 Summary

We have successfully synthesized Na deficient samples $Na_{4-x}Ir_3O_8$ (x = 0, 0.1, 0.3, 0.7) having the hyperkagome structure with the cubic space group symmetry $P4_332$,

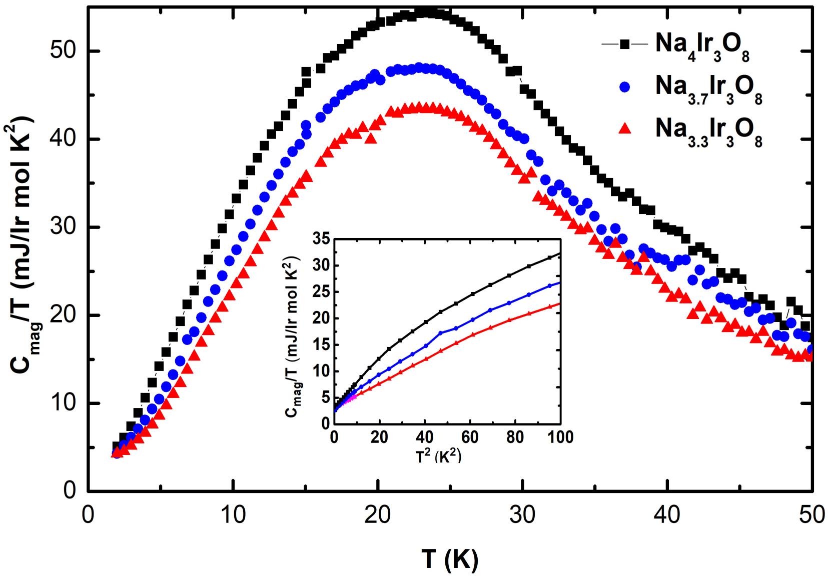

Figure 3.6: (Color online) The magnetic contribution to the heat capacity C_{mag}/T versus T for $Na_{4-x}Ir_3O_8$ (x = 0, 0.3, 0.7). (Inset) Low-temperature C_{mag}/T vs T^2 for $Na_{4-x}Ir_3O_8$ (x = 0, 0.3, 0.7).

and performed electrical transport and magnetic susceptibility χ(T) and heat capacity C(T). We have extended heat capacity measurements on the x = 0 parent compound down to T = 100 mK to look for any magnetic transition and have found none. This firmly establishes $Na_4Ir_3O_8$ as a strong spin - liquid candidate material. The parent compound also shows spin freezing below T $\approx$ 6 K in the magnetic measurements.

For the Na deficient samples, we find that the basic behavior of the parent x = 0 compound persists even on removing large amounts of Na. Specifically, the local moment magnetism with large antiferromagnetic interactions is seen up to x = 0.3. The broad anomaly in the magnetic heat capacity seen in the parent x = 0 material around T = 30 K is still seen for the x = 0.7 sample although its magnitude decreases a bit. Future experiments need to explore whether this anomaly arises from an improper lattice subtraction or is related to the material's magnetism. We can also estimate the Wilson ratio R_W, which is the ratio of the density of states probed by χ (χ_P is the Pauli paramagnetic susceptibility as T $\rightarrow$ 0) to the density of states probed by heat capacity (γ is the Sommerfield coefficient) and is expected to be 1 for a free - electron Fermi gas. For $Na_4Ir_3O_8$, using χ_P $\approx$ 1×10^{-3}cm^3/mol Ir and γ = 2.5 mJ/(mol Ir-K^2), we find a quite large $R_W \approx 30$ suggesting strong magnetic correlations which enhance χ_P

compared to γ. Since χ_P progressively decreases and γ stays approximately the same as Na is removed, the R_W progressively decreases for the Na deficient samples. For the x = 0.7 sample, using $\chi_P = \chi_0 \approx 2.2\times$ 10^4 cm^3/mol Ir and γ = 2.5 mJ/(mol Ir-K^2) from Fig. 3.4(a) and 3.5 insets, respectively, we obtain $R_W \approx 7$. The reduced value of R_W for the Na deficient samples is consistent with a recent theoretical work where it was shown that the susceptibility in the spin liquid state is enhanced over the heat capacity due to strong spin - orbit coupling and correlations, which are reduced in the (semi)metallic state leading to a smaller R_W for the (semi)metallic sample.

Refinements of the powder diffraction patterns have shown that with increasing x, Na is progressively removed from the lattice. Additionally, we have found that Na is preferentially removed from the Na2 (4b) site. This site is not on the Ir tetrahedra and hence deficiency in this site is not expected to lead to disorder in the magnetic Ir sublattice. Therefore, the frustrated hyperkagome lattice of Ir moments is not disturbed with Na deficiency. This is probably why the strong magnetic frustration is robust under removal of fairly large amounts of Na. Na deficiency is however, expected to lead to hole doping of the system. It is therefore surprising that local - moment behavior and insulating behavior survives under hole doping. This is consistent with recent experiments on single crystals of $Na_{3+x}Ir_3O_8$ where it was found that for x = 0.6 (this would be x = 0.4 for our samples) the material was insulating [69]. A metallic state is obtained only for $Na_3Ir_3O_8$ where a different crystal structure is obtained [90]. These observations are surprising given that $Na_4Ir_3O_8$ is regarded as sitting close to a metal - insulator transition and near a quantum critical point (QCP)[68].

In summary, we have shown that the strongly frustrated Mott insulating state in $Na_4Ir_3O_8$ is quite robust against large removal of Na from the lattice. The anomalous properties like the peak in C_{mag} at T ≈ 30 K, the power-law heat capacity, and the large Wilson ratio persists for the doped samples. [97].

Chapter 4

Effect of magnetic and non-magnetic disorder on the quantum spin liquid candidate $Na_4Ir_3O_8$

4.1 Introduction

Iridium has a unique place among transition metals (TMO) in the periodic table. With high atomic number z = 77, its position is in the third row of transition metal atoms. Generally in 3-d transition metals (TM), the spin - orbit coupling (SOC) (SOC $\propto$ z^2, where z is atomic number) is smaller than the crystal field energy Δ. On the other side, the SOC is quite comparable to the other energy scales in 5 - d transition metals. The competition among these energy scales provides the variety of novel physical ground states in Iridates [96].

In the previous chapter we have discussed the robustness of the spin-liquid-like state against large Na removal in the hyper-kagome iridate $Na_4Ir_3O_8$. The comprehensive bulk study of $Na_{4-x}Ir_3O_8$ suggested that the extracted Na, doesn't involve any change in magnetic B-sublattice, which is responsible for the exotic magnetic properties of the parent compound. Keeping this in mind and the recent idea of clarifying the bond disordered spin-liquid behavior of $Na_4Ir_3O_8$, we partially replaced the B sites by magnetic S = 1 ion (Ru^{4+}) as well as non-magnetic ion (Ti^{4+}). This study aims to make a systematic investigation of the role of disorder in a three-dimensional lattice with frustrated magnetic interactions, which can give rise to exotic ground states such as spin glass or bond-disordered spin-liquids.

Another motivation of replacing Ir (5d - TM) with a different magnetic ion is to study the influence of changes in the SOC coupling scheme of the parent compound, which in turn can give rise to a disturbance in the nature and range of the exchange interactions in $Na_4Ir_3O_8$. A study of the influence of changing the spin-orbit coupling might help explain some outstanding experimental observations in $Na_4Ir_3O_8$ [93][94]. In this chapter, we present a comprehensive study of electron transport, magnetic, and thermal properties of $Na_4Ir_3O_8$ as Ir is partially replaced by magnetic Ru and non-magnetic Ti.

4.2 Result and discussion

4.2.1 Powder X - ray diffraction

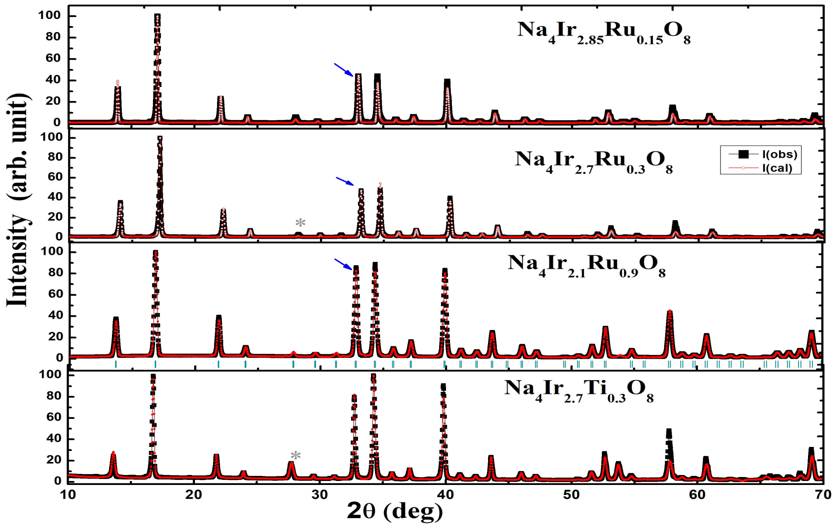

Figure 4.1: (Color online) Powder X - ray diffraction pattern for $Na_4(Ir_{1-x}Ru_x)_3O_8$ (x = 0.05, 0.1, 0.3) and $Na_4Ir_{2.7}Ti_{0.3}O_8$ materials (open symbols). The solid curve through the data is the Rietveld refinement. The $*$ marks the position of the largest diffraction peak for the IrO_2 impurity phase found in the samples. The arrow marks the position of the (311) reflection whose intensity increases with Na deficiency.

Room temperature PXRD for $Na_4(Ir_{1-x}Ru_x)_3O_8$ with different Ru concentrations x = 0.05, 0.10, 0.2, 0.3 and $Na_4Ir_{2.7}Ti_{0.3}O_8$ along with a two phase Rietveld refinement of the data are shown in Fig 4.1. All samples have the expected PXRD pattern apart from a small amount of IrO_2 $(3-4\%)$ which is marked by the $*$ in Fig 4.1 and is similar to the data discussed in the last chapter [66][97][98]. Parameters obtained from a two phase Rietveld refinements are shown in Table-4.1. The variation of the cubic lattice constant 'a' obtained from the refinements and the unit cell volume as a function of Ru doping x are shown in Fig-4.1.

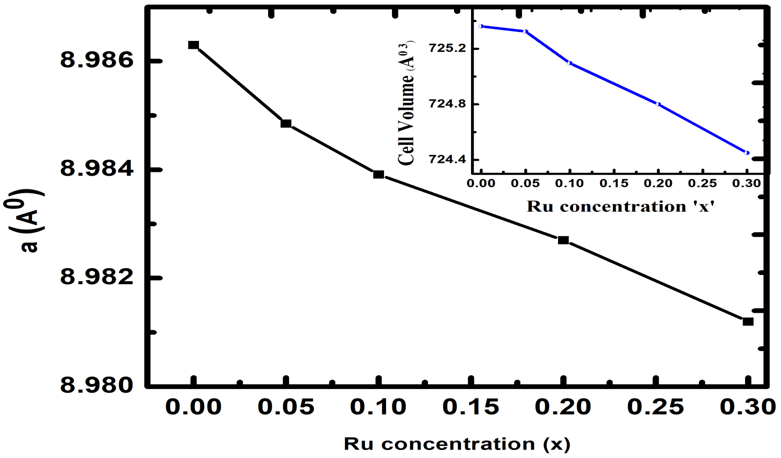

Figure 4.2: Variation of lattice constant with Ru concentration for $Na_4(Ir_{1-x}Ru_x)_3O_8$ (x = 0, 0.05, 0.10, 0.2, 0.3).

Our structural analysis indicates, a monotonic reduction of the cubic lattice parameter a with increasing Ru concentration 'x' which is expected from a comparison of the ionic size of Ir^{4+} (0.625 Å) to Ru^{4+} (0.62 Å). Similarly for $Na_4Ir_{2.7}Ti_{0.3}O_8$, where the lattice parameter shrinks to 8.9684 Å (Ti^{4+} = 0.605Å), an $\approx 1\%$ reduction in the cell volume is estimated compared to the parent compound.

The refined fractional occupation of Ir and Ru/Ti shown in the Table-4.1 matches well with the target concentration x for all samples. These observations indicate that partial substitution of Ru/Ti as a disorder in $Na_4Ir_3O_8$ was successful. As can be seen from Table-4.1, the refinement shows that no appreciable change in the occupancy of the Na1 position which lies in the magnetic B-sublattice. However, small deficit was found in the occupation of Na2 and Na3 sites for all samples. From our previous study of Na deficient samples[97] we conclude that the Na deficiency found in the Ru/Ti substituted samples is small and will keep the materials in the insulating regime. We note that recently crystal growth of $Na_4Ir_3O_8$ has been successful. These authors also found slight Na deficiency in the crystals even though insulating behaviour persisted

Table 4.1: Structural parameters for $Na_4(Ir_{1-x}Ru_x)_3O_8$ (x = 0.05, 0.1, 0.2, and 0.3) and $Na_4Ir_{2.7}Ti_{0.3}O_8$ obtained from a Rietveld refinement of room temperature powder X - ray patterns are shown in Fig-4.1 with space group 213, $P4_132$.

Atom	Wyck	x	y	z	Occ.	B Å^2
$Na_4Ir_{2.85}Ru_{0.15}O_8$,	a = 8.9848 Å		$IrO_2 \approx 3$ %	χ^2= 1.46, R_{exp} = 9.99%; R_{wp} = 14.61%		
Ir	12d	1/8	0.141(3)	0.392(5)	0.94	0.009
Ru	12d	1/8	0.141(3)	0.392(5)	0.06	0.0024
Na1	4a	3/8	3/8	3/8	1	0.009
Na2	4b	7/8	7/8	7/8	0.72(1)	0.008
Na3	12d	0.125	0.1564	0.4064	0.69	0.0042
O1	8c	0.6181	x	x	1	0.006
O2	24e	0.1368	0.8287	0.8592	1	0.025
$Na_4Ir_{2.7}Ru_{0.3}O_8$,	a = 8.9839 Å		$IrO_2 \approx 4$ %	χ^2 = 1.4, R_{exp} = 12.69%; R_{wp} = 17.77%		
Ir	12d	1/8	0.8825	0.1325	0.89	0.0039
Ru	12d	1/8	0.8825	0.1325	0.11	0.0026
Na1	4a	3/8	3/8	3/8	1	0.0069
Na2	4b	7/8	7/8	7/8	0.73	0.0009
Na3	12d	0.125	0.12505	0.3106	0.64	0.0028
O1	8c	0.6654	x	x	1	0.0046
O2	24e	0.1467	0.9809	0.9068	1	0.025
$Na_4Ir_{2.4}Ru_{0.6}O_8$,	a = 8.9827(5) Å		$IrO_2 \approx 6$ %	χ^2 = 1.38; R_{exp} = 14.26%; R_{wp} = 19.72%		
Ir	12d	1/8	0.8854	0.135	0.80	0.009
Ru	12d	1/8	0.8854	0.135	0.19	0.0009
Na1	4a	3/8	3/8	3/8	1	0.0025
Na2	4b	7/8	7/8	7/8	0.70	0.0028
Na3	12d	0.125	0.141900	0.391900	0.64	0.0025
O1	8c	0.629706	x	x	1	0.0025
O2	24e	0.1439	0.8956	0.9025	1	0.0025
$Na_4Ir_{2.1}Ru_{0.9}O_8$,	a = 8.9812 Å		$IrO_2 \approx 5$ %	χ^2 = 1.36; R_{exp} = 15.659%; R_{wp} = 20.61%		
Ir	12d	1/8	0.9025	0.1588	0.69	00013
Ru	12d	1/8	0.9025	0.1588	0.30	0.0074
Na1	4a	3/8	3/8	3/8	1	0.0025
Na2	4b	7/8	7/8	7/8	0.68	0.0028
Na3	12d	0.125	0.1544	0.4044	0.61	0.0025
O1	8c	0.6339	x	x	1	0.0025
O2	24e	0.1354	0.8972	0.9007	1	0.0025
$Na_4Ir_{2.7}Ti_{0.3}O_8$,	a = 8.9684(16) Å		$IrO_2 \approx 11$ %, χ^2 = 1.24; R_{exp} = 10.11%; R_{wp} = 12.64%			
Ir	12d	1/8	0.8828	0.1328	0.889	0.002
Ti	12d	1/8	0.8828	0.1328	0.09	0.009
Na1	4a	3/8	3/8	3/8	1	0.0025
Na2	4b	7/8	7/8	7/8	0.70	0.0013
Na3	12d	0.125	0.1575	0.4075	0.65	0.0078
O1	8c	0.6316	x	x	1	0.0047
O2	24e	0.1399	0.8760	0.9052	1	0.0025

[98]. We will show that the slight Na deficiency in our samples will not affect the conclusions we draw about changes to properties of $Na_4Ir_3O_8$ due to partial replacement of Ir by Ru/Ti.

4.2.2 Resistivity

Fig 4.3 shows the variation of resistivity ρ versus temperature of $Na_4(Ir_{1-x}Ru_x)_3O_8$ for x = 0, 0.1 , 0.2, and 0.3. At $T = 300$ K, for $x = 0.3$ the resistivity value decreases by about an order of magnitude compared to the parent compound $Na_4Ir_3O_8$. We didn't find any systematic variation of resistivity versus temperature for x = 0, 0.1, 0.2, and 0.3. Since PXRD data also shows some trace (≈ 5 %) of IrO_2 impurity in all samples, this might be a reason for the change in resistivity values for other samples but all samples were showing insulating behavior. The decrease in ρ(T) for x = 0.3 then the parent compound is consistent with electron addition in $Na_4Ir_3O_8$ which leads the system into a metallic state.

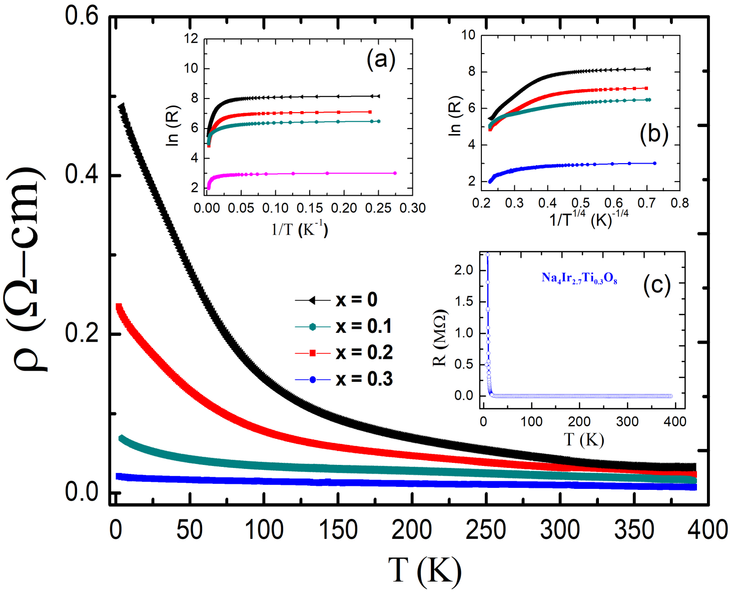

Figure 4.3: Resistivity versus Temperature of $Na_4(Ir_{1-x}Ru_x)_3O_8$ for (x = 0, 0.1, 0.2, and 0.3). Inset: (a) shows a semilog plot of R vs 1/T data. Inset: (b) a semilog plot of R vs $1/T^{1/4}$. Inset: (c) shows the resistance versus temperature of $Na_4Ir_{2.7}Ti_{0.3}O_8$.

Inset Fig-4.3(a) shows the data plotted as R versus 1/T on a semilog plot. From this plot it is clear that the data do not follow an Arrhenius kind of activated behavior in any extended temperature range. Inset (b) shows the data plotted as R versus 1/$T^{1/4}$ on a semilog plot. Such behavior is expected when the conduction mechanism is variable range hopping (VRH) in three dimensions, which is usually observed in disordered semiconductors. We did not find the correct fit (straight line) for both mechanisms. The source of this type of behavior is unclear at the moment. Further measurements like: X-ray photoelectron spectroscopy (XPS) to account for the exact oxdiation state of Ir (Ir^{4+} or Ir^{5+}) will be helpful to explain this mechanism in the doped samples. The drastic change in resistivity was observed in $Na_4Ir_{2.7}Ti_{0.3}O_8$, where the resistance goes into the MΩ at low-temperature (below 5 K) as shown in the inset of Fig-4.3(c).

4.2.3 Magnetic Susceptibility

The temperature dependence of the dc magnetic susceptibility $\chi = M/H$ at applied magnetic field H = 1 T for $Na_4(Ir_{1-x}\ Ru_x)_3O_8$ (x = 0.05, 0.10, 0.2, 0.3) and $Na_4Ir_{2.7}Ti_{0.3}O_8$ is shown in Fig. 4.4. It can be seen from Fig 4.4(a) that χ for Na_4 $(Ir_{1-x}Ru_x)_3O_8$ continually increases with increase in Ru concentration as expected on partially substituting Ir (S = 1/2) with Ru (S = 1) moments. The high-temperature data were found to follow a Curie-Weiss behavior. The χ(T) data for $T \geq 150$ K were fit by the Curie-Weiss expression $\chi = \chi_0 + C/(T - \theta)$ where χ_0, C, and θ are the fitting parameters. The parameters obtained from the fit to the data for each sample $Na_4(Ir_{1-x}Ru_x)_3O_8$ (x = 0, 0.05, 0.1, 0.2, 0.3) are given in Table 4.2. There were two results which we got from DC magnetic susceptibility data analysis for Ru dopping. (1) The experimental values of effective magnetic moment (μ_{eff}) estimated from the Curie constant C are consistent with expectations of substituting S = 1/2 with S = 1 ions. (2) Curie-Weiss fit gave Curie temperature θ, which is large and negative and increases with increasing 'x' (listed in Table 4.2). This large and negative value of θ indicates that strong antiferromagnetic interactions persist in all the Ru substituted samples.

Another feature of interest in the parent compound $Na_4Ir_34O_8$ is the spin freezing below $T_f \approx 6$ K. To track the evolution of T_f with x the inset of Fig.-4.4 shows the zero - field - cooled (ZFC) and field - cooled (FC) magnetization versus temperature data for various x measured at H = 0.02 T. The bifurcation between ZFC - FC marked by arrows in Fig-4.4(a) inset is taken as the T_f and is seen clearly in all Ru substituted

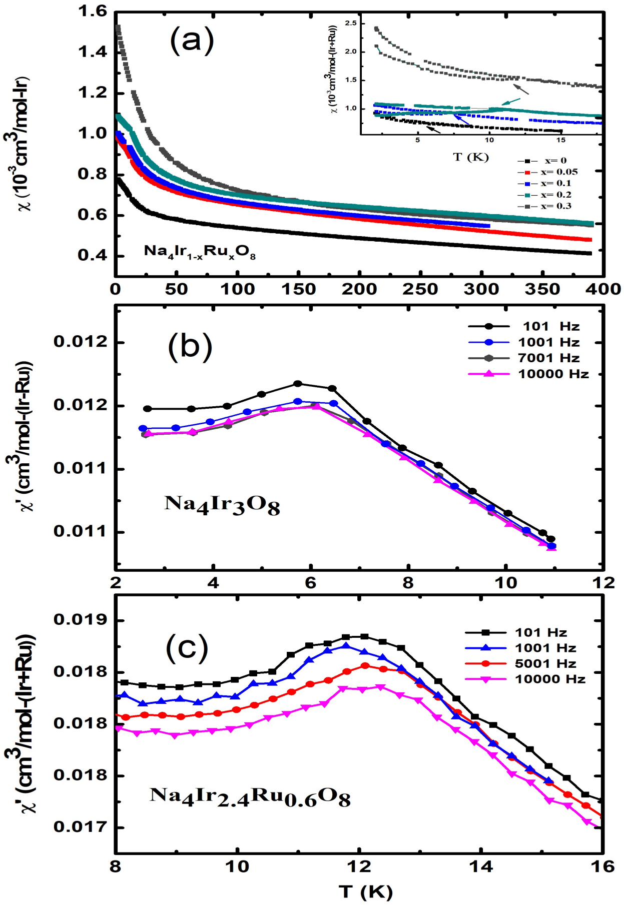

Figure 4.4: (color line) (a) DC Magnetic susceptibility χ versus temperature T(K) for Na$_4$(Ir$_{1-x}$Ru$_x$)$_3$O$_8$ (x = 0, 0.05, 0.1, 0.2, and 0.3) measured at a magnetic field H = 1 T. The inset shows the ZFC - FC χ versus T measured at H = 200 Oe for x = 0, 0.05, 0.1, 0.2 samples. (b) Real part of the AC magnetic susceptibility χ' versus T for Na$_4$Ir$_3$O$_8$ and (c) Na$_4$Ir$_{2.4}$Ru$_{0.6}$O$_8$ measured with various excitation frequencies.

samples. It was found that T$_f$ increases significantly with x reaching a value T$_f$ = 13.2 K for x = 0.3. The ZFC - FC bifurcation being a signature of a spin - glass state is supported by our AC susceptibility χ_{ac} measurements.

Fig.-4.4 (b) and (c) show the frequency dependence of χ_{ac} versus T for the x = 0 and x = 0.3 samples. A clear maximum is observed in χ_{ac} at a temperature which matches with the bifurcation in ZFC - FC dc χ data. The maximum, which moves to higher temperatures on increasing the excitation frequency is a strong signature of a glassy state[23]. Thus, the increased disorder due to Ru substitution results in higher freezing temperature.

A different picture emerges for non-magnetic Ti doping. Figure- 4.5(a) shows the

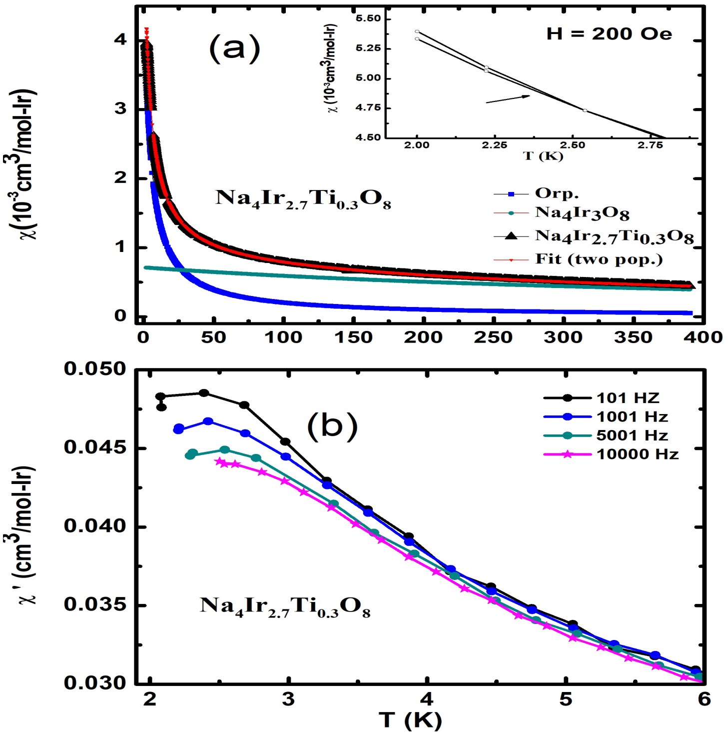

Figure 4.5: (color line) DC Magnetic susceptibility χ versus T for $Na_4Ir_{2.7}Ti_{0.3}O_8$. A two population model fit is shown as the solid curve through the data. The orphan spin contribution is also shown (see text for details). Inset shows the ZFC - FC χ versus T measured at H = 200 Oe. (b) Real part of the AC Magnetic susceptibility χ' versus T for $Na_4Ir_{2.7}Ti_{0.3}O_8$ measured with different excitation frequencies.

χ versus temperature for the $Na_4Ir_{2.7}Ti_{0.3}O_8$. We observe that Ti^{4+} substitution results in an enhanced paramagnetic susceptibility. This is most likely due to the creation of orphan spins i.e. some of the Ir spins behave as free spins and contribute an extra Curie paramagnetic term. The "orphan spins" were hypothesized in a phenomenological two level population model for geometrically frustrated magnets [95], where as a result of disorder, a small fraction of the spins are excluded from the correlated spin clusters (uncorrelated). Hence we have used the two-population model for quantitative estimation of the orphan-spin contribution. Specifically, we fit the data with the expression $(\chi - \chi_0) = \frac{C_1}{(T+\theta_1)} + \frac{C_2}{(T+\theta_2)}$, where C_1, C_2, θ_1 and θ_2 are the Curie constant and Curie - Weiss temperature for correlated and orphan spins respectively [95]. We found C_1 = 0.36 cm^3-K/mol-(Ir+Ru), C_2= 0.017 cm^3-K/mol-(Ir+Ru), θ_1 = -500 K and θ_2 = - 4.5 K. Additionally, from the fitted data we found that 5.1 % of Ir spin could give rise to the orphan spin states which result in a significant suppression in the magnetic energy scale θ_1. The ZFC - FC magnetization versus temperature of $Na_4Ir_{2.7}Ti_{0.3}O_8$ has been plotted in the inset of Fig-4.5(a). We find a clear bifurcation in the ZFC - FC curve around the 2.3 K, which was seen in the parent compound at T$_f$ = 6 K. Our magnetic measurements support the fragile nature of magnetic ground state of $Na_4Ir_3O_3$, where the non - magnetic Ti doping shows the opposite behavior of magnetic energy scale θ and spin - freezing temperature T_f as compared to magnetic doping.

Table 4.2: Parameters obtained by Curie - Weiss fit of magnetic susceptibility of $Na_4(Ir_{1-x}Ru_x)_3O_8$ (x = 0, 0.05, 0.1, 0.2, and 0.3) in the temperature range 150 - 400 K.

	$\chi_0 \frac{10^{-5}cm^3}{(Ir+Ru)mol}$	θ (K)	C $\frac{cm^3K}{(Ir+Ru)mol}$	$\mu_{eff}(\mu_B)$	T$_f$ (K)
x = 0	8.58 (2)	-650 (4)	0.39 (3)	1.77	6.3
x = 0.05	2.006 (1)	-689.4 (2)	0.48 (4)	1.96	7.41
x = 0.1	6.299 (1)	-787.15(5)	0.52 (2)	2.03	9.8
x = 0.2	6.101(4)	-889(3)	0.59(7)	2.17	11.6
x = 0.3	6.35(2)	-983(4)	0.67(3)	2.31	13.2

The data of the real part of AC magnetization as (χ') versus temperature for $Na_4Ir_{2.7}$ $Ti_{0.3}O_8$ at various excitation frequencies f from 1 kHz to 10 kHz is shown in Fig-4.5(c). A clear maximum is observed near 2.3 K at low frequency and this maximum moves to higher temperatures for higher frequencies, a clear signature of spin - glassy behaviour below T$_f$ $\approx$ 2.3 K[23].

Therefore, both Ru and Ti substituted samples show a spin-glassy state at low temperatures. A quantitative measure of the shift in the peak position with frequency is usually made using the ratio $\frac{\Delta T_f}{T_f \Delta log f}$, where ΔT_f is a shift in the freezing temperature T$_g$ and $\Delta log f$ is the decade change in the frequency f [23]. The ratio is found to be 0.056 and 0.072 for $Na_4Ir_3O_8$,and $Na_4Ir_{2.4}Ru_{0.6}O_8$ respectively. For the canonical spin glass material CuMn and other metallic spin-glasses this ratio is found $\sim$ 0.005 [23], but for our samples it's very large.

4.2.4 Heat capacity

The magnetic contribution to the heat capacity C$_{mag}$ versus T data for the Ru substituted samples $Na_4(Ir_{1-x}Ru_x)_3O_8$ (x = 0, 0.05, 0.1, 0.2) are plotted in Fig.4.6(a). The heat capacity of the iso - structural non - magnetic material $Na_4Sn_3O_8$ was used to estimate the lattice contribution to the heat capacity for $Na_4(Ir_{1-x}Ru_x)_3O_8$ in the same manner as described in the previous chapter for x = 0 sample. The parent compound $Na_4Ir_3O_8$ shows a broad anomaly in magnetic heat capacity around T = 28 K, which is the consequence of some short-range magnetic correlations. Surprisingly, we found that the broad heat capacity anomaly decreased in height with increasing the Ru (S = 1) concentration from x = 0 to 0.2 as shown in Fig-4.6(a). Since the robustness of specific heat was reported for our sodium deficient samples [97], but there was no shifting and squeezing of these magnetic heat anomaly on sodium deficiency. These magnetic heat anomaly shifted from T $\approx$ 25 K to T $\approx$ 20 K as we go from x = 0 to 0.2.

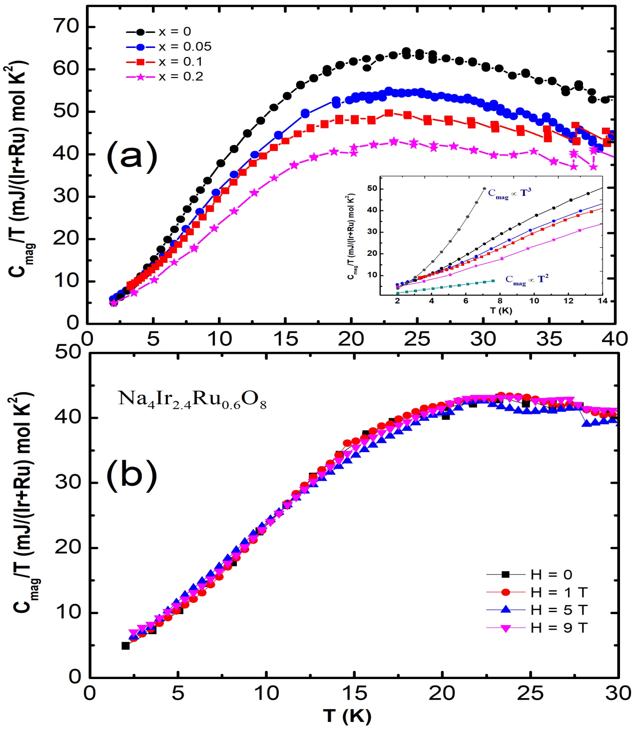

Figure 4.6: (a) C_{mag} /T versus T for $Na_4(Ir_{1-x}Ru_x)_3O_8$ (x = 0, 0.1, 0.05 and 0.2). Inset shows the low - temperature power - law T dependence of C_{mag}/T for $Na_4(Ir_{1-x}Ru_x)_3O_8$ (x = 0, 0.1, 0.05 and 0.2). (b) C_{mag}/T versus T for $Na_4Ir_{2.4}Ru_{0.6}O_8$ at different applied magnetic fields.

The inset in Fig.-4.6(a) shows the variation of C_{mag}/T versus T at low-temperatures to highlight the power - law behaviour of C_{mag}. The power law fit were done for T = 2 to 10K. These data show power law $C_{mag} \sim T^{\alpha}$ behaviour with an exponent α between 2 and 3 as has been reported previously for the x = 0 material[66]. The exponent was

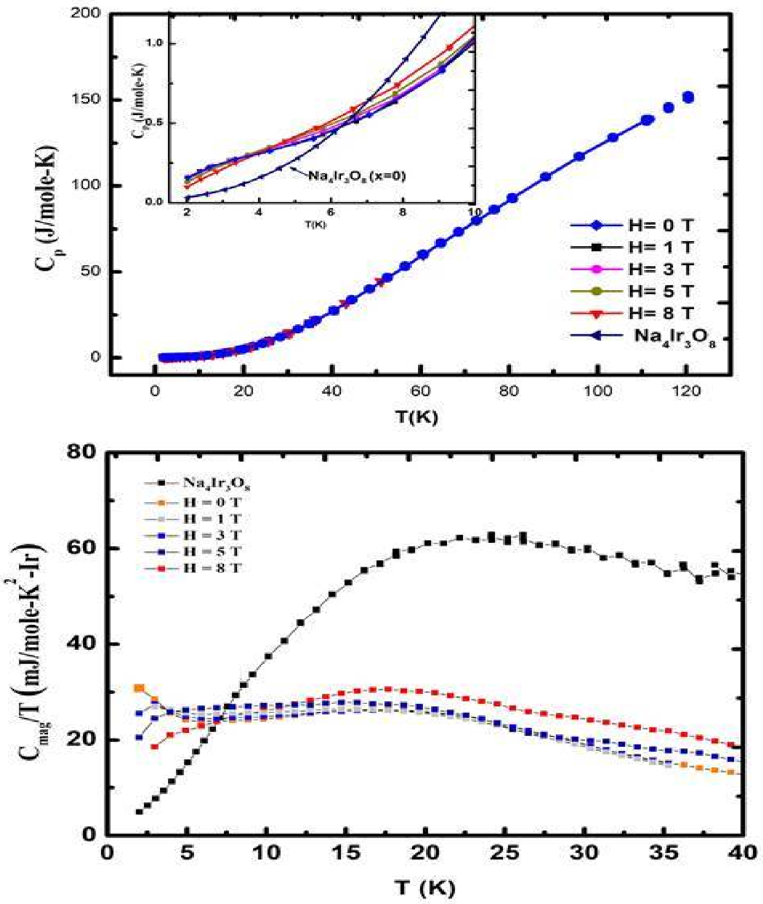

Figure 4.7: (a) Heat capacity C$_p$ versus Temperature T(K) for Na$_4$Ir$_{2.7}$Ti$_{0.3}$O$_8$ at different applied magnetic fields up to 9 T. Inset: shows the low - temperature variation of C$_p$/T for Na$_4$Ir$_{2.7}$Ti$_{0.3}$O$_8$ at different applied magnetic fields. (b) C$_{mag}$/T versus T for Na$_4$Ir$_{2.7}$Ti$_{0.3}$O$_8$.

found to decrease with increasing x and reaches ≈ 2 for x = 0.2. Fig.-4.6(b) shows the C$_{mag}$/T vs T data for Na$_4$Ir$_{2.4}$Ru$_{0.6}$O$_8$ measured at various applied magnetic fields. It was found that the broad anomaly in C$_{mag}$ and the exponent of the low - temperature power - law bevaviour are largely insensitive to magnetic fields up to H = 9 T.

The C$_{mag}$ data measured in various magnetic fields for Ti - doped Na$_4$Ir$_{2.7}$Ti$_{0.3}$O$_8$ is shown in Fig- 4.7(a). The comparision of C$_{mag}$/T versus temperature between Na$_4$Ir$_{2.7}$Ti$_{0.3}$O$_8$ and Na$_4$Ir$_3$O$_8$ at the different applied magnetic field is shown in Fig-4.7 (b). A drastic suppression of magnetic heat capacity as compared to the parent compound is seen and the magnetic heat capacity C$_{mag}$/T shows the strong magnetic field dependence in the measured temperature range. The Ti substitution thus has significant influence on the thermodynamic properties of $Na_4Ir_3O_8$.

4.3 Summary

The primary motive of this study is to understand the bond disorderd spin - liquid state. By substitution of Ru/Ti for Ir, we disturbed the magnetic interactions between the Ir atoms in $Na_4Ir_3O_8$. Our PXRD results confirm the substitution of Ru/Ti in $Na_4Ir_3O_8$. Both Ru and Ti have a metallic radius smaller than Ir, which leads to a decrease in the lattice size. The cell volume shrinks by almost 1% for $Na_4Ir_{2.7}Ti_{0.3}O_8$.

At first, we briefly want to summarize the results of the Ru doping with x = 0, 0.1, 0.05, 0.2, and 0.3, which are quite different from Ti doping in $Na_4(Ir_{1-x}Ru_x)_3O_8$. Since $Na_4Ir_3O_8$ is a well defined Mott insulator. With the addition of electron the resistivity of system decrease but persist it's insulating behavior. DC magnetic susceptibility shows the effective magnetic moment μ_{eff} and Curie - Weiss temperature with large antiferromagnetic exchange of $Na_4(Ir_{1-x}Ru_x)_3O_8$ (x = 0, 0.05, 0.1 and 0.3) increases with increase in ruthenium content. This is most likely due to an enhancement of magnetic exchange due to compression of the lattice. The combined results of ZFC - FC magnetization and ACMS provide that the spin - freezing temperature T_f increases with x and reaches $T_f \approx 12.4$ K for x = 0.2. This reflects the increasing disorder in the partially substituted samples which leads to an enhanced freezing temperature. This also suggests that the parent material is inherently disordered and efforts to synthesize less disordered $Na_4Ir_3O_8$ should be made to reveal the true ground state which might well be the much sought after three - dimensional quantum spin liquid.

Further, the magnetic heat capacity analysis confirmed the magnetic field independence of the anomaly of the C_{mag}/T of x = 0.2 sample. This behavior is generally expected for the spin - liquid state. The most surprising result was found that the broad anomoly in magnetic heat capacity squeezed and shifted towards the lower temperature with increase in Ru concentration. It shifted from 25 K to 20 K as x changing from 0 to 0.2. The C_{mag} data continues to show a magnetic field insensitive power - law bhaviour $C_{mag} \sim T^{\alpha}$ for all x and the exponent α falls towards 2 with increasing x.

The non - magnetic Ti doping $Na_4Ir_{2.7}Ti_0.3O_8$ shows a different behavior with compared to magnetic Ru doping. Although both Ru^{4+} and Ti^{4+} has the smaller ionic radii, which suggest the similar chemical pressure in $Na_4Ir_3O_8$. But this study strongly suggest the fragile nature of magnetic sublattice against the bond disorder with respect to magnetic or non - magenic doping.

The drastic change was found in magnetic susceptibility and magnetic heat capacity of the $Na_4Ir_{2.7}Ti_{0.3}O_8$. The magnetic correlations weaken as evidenced by a smaller Weiss temperature, the spin - freezing is pushed to much lower temperature $T_f \approx$ 2.3 K suggesting a percolation mechanism, and the anomaly in C_{mag} is completely suppressed. Future microscopic studies like NMR, μSR on our Ru/Ti - doped material should help in our understanding of $Na_4Ir_3O_8$ and its evolution under various chemical perturbations.

Chapter 5

Pressure and field-dependent magnetic properties of the kagome-bilayer spin liquid $Ca_{10}Cr_7O_{28}$

5.1 Introduction

The recently discovered kagome bi-layer spin-liquid material $Ca_{10}Cr_7O_{28}$, provides a new direction in the field of QSL, where dominant ferromagnetic interactions within the kagome bilayer are responsible for QSL state. This kagome bilayer compound hosts a novel frustration mechanism where competing ferro and antiferromagnetic exchange interactions within a kagome bilayer suppress the possibility of long-range magnetic order [32][33]. Both experimental and theoretical studies strongly suggested the signatures of a gapless quantum spin liquid (QSL) in $Ca_{10}Cr_7O_{28}$ [32][33].

While low-dimensionality and large frustration with AFM exchange interaction are considered essential ingredients for the QSL state, $Ca_{10}Cr_7O_{28}$ provides an excellent new direction in the field of QSL where the QSL state is achieved by the dominant ferromagnetic interactions. One out of seven chromium ions in the formula unit is a nonmagnetic Cr^{6+} ion. Fig:-5.1 shows the arrangement of the magnetic (Cr1, Cr2) and nonmagnetic chromium (Cr3A, Cr3B) ions. These ions sit in four inequivalent tetrahedra. The structure is made up of layers of these different tetrahedra alternating along the c-axis as shown in Fig:- 5.1(a). Within the layers the tetrahedra are arranged on a distorted Kagome lattice as can be seen in Fig:- 5.1(b). The magnetic connectivity between the Kagome layers is such that the blue and orange Kagome layers interact with each other but are isolated from the other layers. Similarly, the yellow and purple Kagome layers interact but are isolated from the others. Thus, magnetically, $Ca_{10}Cr_7O_{28}$ can be viewed as a bilayer Kagome system as shown in Fig:- 5.1(c).

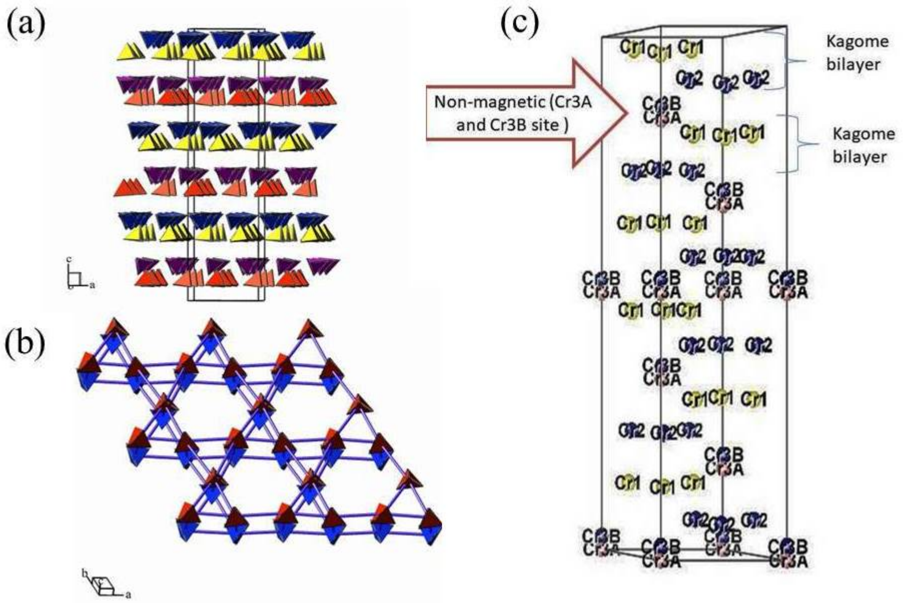

Figure 5.1: (a) Structure of $Ca_{10}Cr_7O_{28}$ viewed perpendicular to the c - axis. The four inequivalent CrO_4 tetrahedra are shown in different colors. Planes formed by these CrO_4 tetrahedra are stacked along the c - axis. (b) A view approximately down the c- axis showing the bilayer kagome network of Cr ions. (c) Structure of $Ca_{10}Cr_7O_{28}$ viewed perpendicular to the c - axis with different chromium positions.

In this chapter, we address the synthesis, crystal structure and effect of hydrostatic pressure ($P \approx 1$ GPa) on the magnetic properties of $Ca_{10}Cr_7O_{28}$.

5.2 Results and discussion

5.2.1 Powder X-ray diffraction-structure

The powder X-ray diffraction (PXRD) data are shown in Fig-5.2. The PXRD data could be refined starting with the structural model of $Ca_{10}Cr_7O_{28}$[32][33]. The Rietveld refinement results are also plotted in Fig-5.2. The lattice parameters obtained from the fit are a = b = 10.7885(3) Å, c = 38.163(1)Å, $\alpha = \beta = 90°$, $\gamma = 120°$, and the cell volume V = 3846.79(20) $Å^3$. The Wyckoff atomic positions, site occupancies, and thermal parameters obtained from the fit are given in Table-5.1. These parameters match well with recently reported data on single crystals [32][33] and confirm the single phase synthesis of polycrystalline $Ca_{10}Cr_7O_{28}$ for the first time.

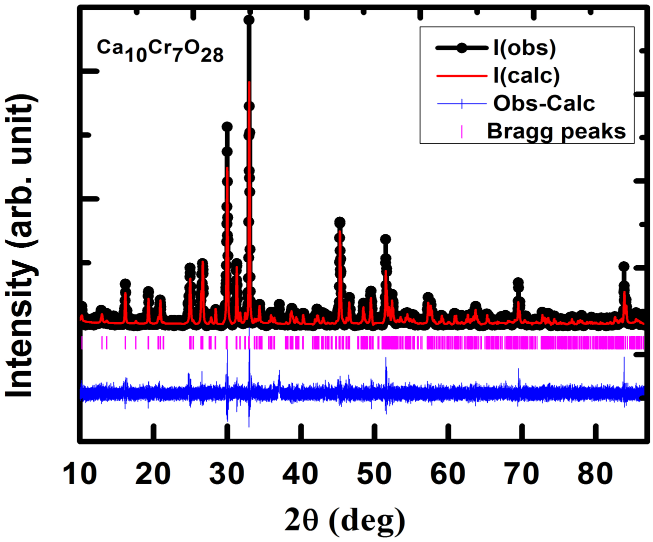

Figure 5.2: Rietveld refinement of powder, which diffraction data for $Ca_{10}Cr_7O_{28}$. The solid circles represent the observed data, the solid lines through the data represent the fitted pattern, the vertical bars represent the peak positions, and the solid curve below the vertical bars is the difference between the observed and the fitted patterns.

5.2.2 Ambient pressure magnetism

Fig:-5.3 shows the magnetic susceptibility χ = M/H versus temperature T of $Ca_{10}Cr_7O_{28}$ measured in a magnetic field H = 500 Oe and 20 kOe. Curie - Weiss like local moment paramagnetism is clearly evident. At low temperatures, χ increases rapidly and reaches values which are quite large and similar to values seen in ferromagnetic materials. However, no anomaly signalling long-range magnetic order is observed down to T = 1.8 K.

The χ^{-1}(T) data at high temperatures T $\geq$ 200 K were fit by the Curie-Weiss expression χ = χ_0 + C /T-θ, where χ_0 is a T independent contribution, C is the Curie constant, and θ is the Weiss temperature. The 1/χ(T) data and the fit are shown in Fig.-**??**. The fit gave the values χ_0 = - 5.2(4) $\times$ 10^{-5} cm^3/Cr, C = 0.30(2) cm^3 K/Cr, and θ = 4.1(6) K. The value of C is smaller than the value 0.375 cm^3K/Cr expected for S =

Table 5.1: Atomic parameters obtained by refining X-ray powder diffraction for $Ca_{10}Cr_7O_{28}$ with a space group 167, R-3c. The lattice constants are a = b = 10.788(3)Å, c = 38.163(1) Å, α = β = 90° and λ = 120°. χ^2 = 1.54; R_{wp} = 19.43%; R_{exp} = 12.59%

Atom	Wyck	x	y	z	Occ.	B $Å^2$
Ca1	36f	0.292(4)	0.165(8)	-0.070(6)	0.97	0.008
Ca2	36f	0.182	-0.204(3)	-0.008(5)	0.96	0.0071
Ca3	36f	0.374	0.157	0.022	1	0.0086
Ca4	12c	0.666(7	0.333	0.087	1	0.0099
Cr1	36f	0.316(2)	0.154(7)	0.124	1	0.0012
Cr2	36f	0.164(7)	-0.142	-0.107	0.95	0.0143
Cr3A	12c	0.000	0.000	-0.018(4)	0.64(5)	0.0031
Cr4B	12c	0.000	0.000	-0.007(5)	33	0.0064
O3A	12c	0.000	0.000	-0.023(2)	0.65	0.001
O3B	12c	0.000	0.000	-0.364	0.025	0.009
O1	36f	0.300(9)	0.189(8)	0.054(9)	0.84(8)	0.0192
O2	36f	0.209	0.173(4)	0.182(5)	1	0.0110
O3	36f	0.116	-0.0331	0.130(7)	1	0.0395
O4	36f	0.367	0.147(6)	0.131	1	0.0008
O5	36f	0.1239	-0.155(7)	-0.062	0.95(4)	0.033
O6	36f	0.231(7)	-0.267(6)	-0.124(4)	1	0.0081
O7	36f	-0.010(3)	-0.227(7)	-0.118(4)	0.86	0.0094
O8	36f	-0.106	0.011(5)	0.006(6)	0.95	0.0131

1/2 with g = 2. However, out of the seven Cr ions in each formula unit of $Ca_{10}Cr_7O_{28}$, six are in Cr^{5+} valence state with S = 1/2 and one Cr ion is in Cr^{6+} valence state and is expected to be nonmagnetic with S = 0. Therefore the value of the Curie constant per magnetic Cr ion will be C = 7/6 the value 0.30(2) cm^3 K/Cr found above. This gives C $\approx$ 0.35(2), which in turn leads to an effective magnetic moment $\mu_{eff} \approx$ 1.68(5) μ_B, which is close to the value 1.73 μ_B expected for spin S = 1/2 with g factor equal to 2 [104].

The value of θ = 4.1(6) K is small and positive indicating weak ferromagnetic exchange interactions. This is consistent with the huge increase in χ at low T seen in

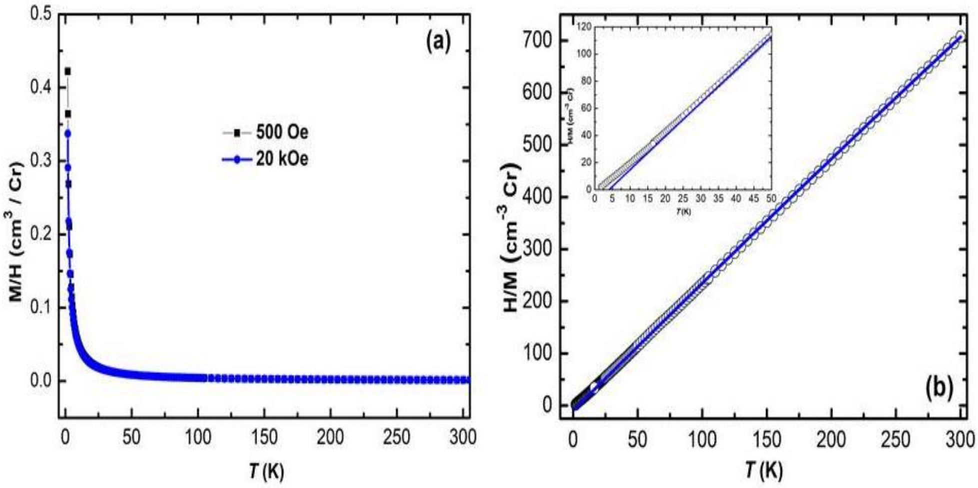

Figure 5.3: (a) Magnetization M divided by magnetic field H vs temperature T for $Ca_{10}Cr_7O_{28}$ measured in H = 500 Oe and 20 kOe. (b) H/M vs T measured at H = 20 kOe. The solid curve through the data is a fit by the Curie-Weiss expression. The inset shows the H/M data below T = 50 K to highlight the deviation of the data from the Curie-Weiss fit. The data are presented per Cr in the formula unit (which is 7).

Fig.-5.3(a). The magnetic exchange interactions are, however, more complex as can be inferred from the deviation below T = 20 K of $1/\chi(T)$ from the Curie-Weiss fit as can be seen in Fig.-5.3(b) inset. The $1/\chi(T)$ data deviate upwards of the Curie-Weiss fit, which means that the χ(T) data becomes smaller than expectation from the fit. This indicates the presence of antiferromagnetic interactions. Thus the magnetic susceptibility data suggest the presence of both ferromagnetic and antiferromagnetic exchange interactions with the ferromagnetic interactions being the dominant ones leading to a net positive Weiss temperature $\theta \approx 4$ K [104].

The magnetisation M versus magnetic field H data measured at various temperature T are shown in Fig.-5.4. For T $\geq$ 50 K, M(H) isotherms are linear in H. For the M(H) data at T = 25 K one observes a slight curvature. However, the M(H) isotherms at T = 5 and 1.8 K show clear curvature with the tendency of saturation. This is consistent with net ferromagnetic interactions, which are weak. The data at T = 1.8K, although still increasing with H, is near saturation to values close to ≈ 80 % of the value expected (M = 1 μ_B/Cr) for S = 1/2 moments. This is again consistent with only six out of seven chromium ions being magnetic. The fact that the magnetic moments can be saturated at magnetic fields ~ 5 T also suggests that the energy scale of the largest magnetic exchange interactions in $Ca_{10}Cr_7O_{28}$ is small ~ 10 K.

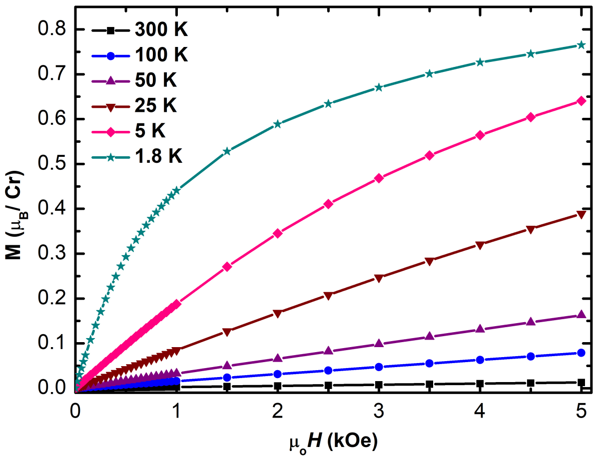

Figure 5.4: Magnetization M vs magnetic field H for $Ca_{10}Cr_7O_{28}$ measured at various temperatures T. The data are presented per Cr in the formula unit (which is 7).

5.2.3 High-pressure magnetism

If, as is believed, the spin-liquid state in $Ca_{10}Cr_7O_{28}$ is stabilized by a delicate balance of several magnetic exchanges [32], then pressurizing the material may disturb this balance and lead to a destruction of the spin-liquid state and may in turn lead to the stabilization of a magnetically ordered state. Additionally, the kagome bilayers, which are magnetically isolated at ambient pressure [32] may start interacting if brought closer. With this motivation we have performed high-pressure measurements of the magnetic susceptibility χ versus T at various applied hydrostatic pressures P. Fig.-5.5 shows the high-pressure χ(T) data for $Ca_{10}Cr_7O_{28}$. From the main panel, we can see that although the magnitude of χ at the lowest temperature increases slightly, the basic behavior of χ(T) does not change up to the highest pressures used in our measurements P $\approx$ 1 GPa. For typical transition metal oxides, this pressure amounts to a contraction in the unit cell volume of about 1%. This is a large change in the unit-cell size. The fact that χ(T) does not show any significant change suggests that the spin-liquid state in $Ca_{10}Cr_7O_{28}$ is quite robust and does not hinge on some special values of the exchange parameters.

To make a quantitative analysis of the change in χ(T), we have fitted the high-temperature 1/χ(T) data for P = 0 and $\approx$ 1 GPa to a Curie-Weiss behavior as shown in the inset of Fig.-5.5. In these fits, the effective magnetic moment was fixed at its ambient pressure value. The value of the Weiss temperature changes from $\theta \approx$ 4 K at P = 0 GPa to 7

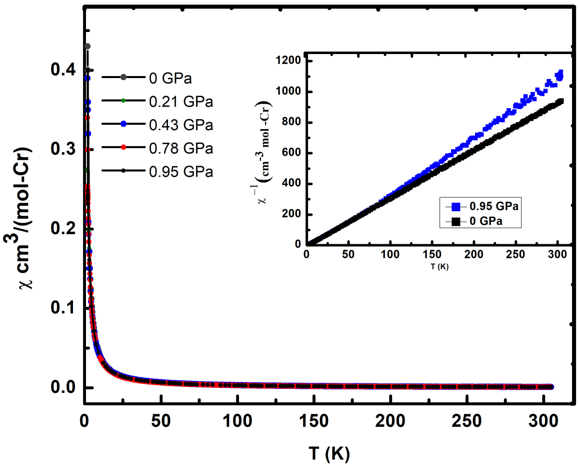

Figure 5.5: Magnetic susceptibility χ vs T for $Ca_{10}Cr_7O_{28}$ measured in various externally applied pressures P in amagnetic field H = 1T. The inset shows the χ^{-1}(T) vs T data for P = 0 and P $\approx$ 1 GPa. The solid curve through the data in the inset are fits to a Curie-Weiss expression. The data are presented per Cr in the formula unit (which is 7).

K at P = 1 GPa suggesting an increase in the relative importance of the existing ferromagnetic exchanges. This is consistent with the increased magnitude of χ at the lowest temperatures in applied pressures [104].

5.2.4 Heat capacity

Heat capacity C versus temperature T data for $Ca_{10}Cr_7O_{28}$ measured between T = 1.8 and 40 K in various magnetic fields H are shown in the main panel in Fig.-5.6. The inset shows the same data plotted as C/T versus T. The first thing to note is that the H = 0 data below T = 10 K shows an upturn and approximately saturates below T = 3 K. This might suggest an onset of long-range order. On application of a magnetic field this upturn moves up in temperature and develops into a complete peak at H = 3 T. The peak then moves to higher temperatures for larger H. The broad peak is very unlike that expected for a second-order phase transition where a λ-like anomaly is usually seen in the heat capacity. Thus we believe that this anomaly does not signal a magnetic phase transition. This is supported by the entropy recovered under the peak as we now describe. From Fig.-5.6 inset, it is clear that the magnetic fields have a pronounced effect at low temperatures. However, the data above T = 30 K are independent of H suggesting that it is mostly of nonmagnetic origin. We therefore use the data above T = 30 K and extrapolate it to lower temperatures to get an approximate estimation of the lattice heat capacity. These data are shown as the solid curve in Fig.-5.6. Using this, we can get the magnetic contribution to the heat capacity at various magnetic fields by subtracting the approximate lattice contribution from the C(T,H) data. This has been done and the resulting difference data $\triangle$C(T,H) are shown in Fig.-5.7 for all magnetic fields. The $\triangle$C(T,H) thus obtained can be used to estimate the magnetic entropy by integrating $\triangle$C/T versus T data. The temperature dependence of the entropy S(T) estimated in this way is shown in Fig.-5.7 (inset) for all magnetic fields. The S(T) data are presented in units of Rln2 per magnetic Cr.

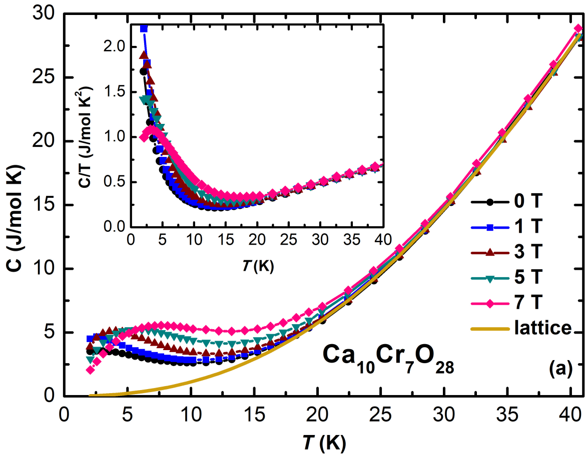

Figure 5.6: Heat capacity C vs temperature T for $Ca_{10}Cr_7O_{28}$ measured in various magnetic fields H. The inset shows the C/T vs T data.

We note that S(T) for H = 0 reaches about 85%Rln2 at T $\approx$ 30 K. It is therefore unlikely that a long-range magnetic order will occur at lower temperatures. If such a transition does occur, it can involve only 15%Rln2 entropy, which would mean a much reduced moment ordering. This is consistent with previous C(T) measurements on single crystalline $Ca_{10}Cr_7O_{28}$ down to T = 0.3 K in H = 0 that have revealed the absence of long-range magnetic ordering [32].

In a magnetic field, the anomaly in the magnetic contribution moves to higher temperatures although the magnitude of the peak does not change as can be seen most clearly in Fig.-5.7. The temperature of the peak T_P as a function of magnetic field H is plotted in the smaller inset in Fig.-5.7. We find an almost linear dependence of T_P on

H as can be seen by the solid curve through the data, which is the relation T_P = 1.986 + 0.63H. The entropy S(T) associated with the peak in the magnetic contribution to C, shown in Fig.-5.6 inset, is also pushed up in temperatures with increasing H and we recover the full Rln2 at H $\geq$ 3 T. This behavior of the entropy in a magnetic field is a hallmark of geometrically frustrated magnets. The frustration suppresses the tendency for long-range order leading to the accumulation of the entropy of the unordered S = 1/2 moments at lower temperatures. The magnetic field leads to partial alignment of the disordered moments at higher temperatures than at H = 0 leading to magnetic entropy being recovered to higher temperatures. The observation that fields of H $\leq$ 7 T affect the magnetic heat capacity and are able to move the magnetic entropy to higher temperatures again suggests that the magnetic energy scales in $Ca_{10}Cr_7O_{28}$ are $\sim$ 10 - 20 K.

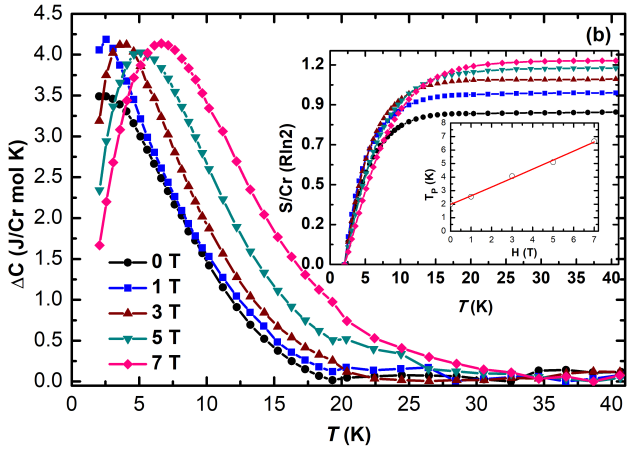

Figure 5.7: The difference heat capacity $\triangle C = C - C_{lattice}$ vs T for various magnetic fields. Inset shows the magnetic entropy estimated from the $\triangle C(T)$ data at various H. The inset in the inset shows the peak position T_P vs magnetic field H. The solid curve through the data is a linear fit.

5.3 Summary

We have for the first time synthesized polycrystalline samples of the recently discovered kagome-bilayer spin-liquid material $Ca_{10}Cr_7O_{28}$ and studied in detail its temperature-dependent magnetic susceptibility at ambient and high pressure, isothermal magnetization, and temperature and magnetic field-dependent heat capacity measurements. The ambient pressure magnetic measurements indicate the presence of both ferromagnetic (FM) and antiferromagnetic (AFM) exchange interactions with the dominating FM interactions. The net magnetic scale is about $\sim$ 10 - 20 K as evidenced by the near saturation of the magnetization at T = 1.8 K in a magnetic field of H = 5 T. The Curie constant is consistent with one out of the seven chromium ions per formula unit being nonmagnetic. The magnetic Cr ions form a bilayer kagome lattice. High-pressure magnetic susceptibility measurements up to P $\approx$ 1 GPa reveal that the spin-liquid state at ambient pressure is quite robust and may not depend on a delicate balance between any specific values of competing exchange interactions. Additionally, our results indicate that at high pressure the relative strength of ferromagnetic interactions increases as evidenced by an increase in the value of the Weiss temperature from θ = 4 K at P = 0 to θ = 7 K at P = 1 GPa.

The heat capacity in H = 0 shows an incomplete anomaly peaked around 2 K. The entropy recovered between T = 1.8 K and T = 30 K in H = 0 is close to 85%Rln2 suggesting the absence of magnetic ordering for lower temperatures, consistent with a spin-liquid state. This broad anomaly peaked in C is consistent with previous zero-field measurements on single crystal $Ca_{10}Cr_7O_{28}$ and was associated with the onset of coherent quantum fluctuations [32]. A similar broad anomaly has been observed for several other QSL candidates. For example, the organic triangular lattice spin liquid $EtMe_3Sb[Pd(dmit)_2]_2$ [57] shows an anomaly in the heat capacity at 6 K, while the recently discovered QSL candidate $YbMgGaO_4$ shows a heat capacity anomaly at 2.4 K [101]. This anomaly for QSLs is understood to be a crossover from a thermally disordered state to a quantum disordered state. A low-temperature anomaly in the heat capacity which moves up in temperatures on the application of the magnetic field is a hallmark of frustrated magnets in general. For example, in addition to the above materials, the pyrochlore spin-ice material $Pr_2Zr_2O_7$ also shows an anomaly in the heat capacity at 2 K, which is attributed to the formation of a collective spin-ice state. This anomaly has been shown to move approximately linearly to higher temperatures with magnetic field [102][103].

The heat capacity anomaly for $Ca_{10}Cr_7O_{28}$ occurs at 2.4 K at H = 0 and moves to higher temperatures in a magnetic field approximately linearly. Since the fields of our measurements are much smaller than the saturation fields of 12-13 T [15,16] the linear dependence of the peak temperature with H is intriguing. Since the ferromagnetic exchange is dominant in $Ca_{10}Cr_7O_{28}$, it is possible that in-plane short-range order develops and is strengthened in a field. However, future measurements would be needed to understand this observation [104].

Chapter 6

Site dilution study of kagome bilayer $Ca_{10}(Cr_{1-x}V_x)_7O_{28}$

In the previous chapter, we have focused on the ambient and high-pressure magnetic study of the Kagome bilayer material $Ca_{10}Cr_7O_{28}$, which has been proposed as a novel quantum spin-liquid candidate with a complex exchange coupling scheme of ferromagnetic and antiferromagnetic exchanges.

In this chapter, we study the effect of nonmagnetic S = 0, V^{5+} substitution on the QSL properties. We have synthesized $Ca_{10}(Cr_{1-x}V_x)_7O_{28}$ ($0 \leq x \leq 0.5$) polycrystals and studied their low - temperature magnetic properties. We also report first time experimental realization of a perfect nonmagnetic analog $Ca_{10}V_7O_{27.5}$ of $Ca_{10}Cr_7O_{28}$, which enables an accurate estimation of lattice heat capacities without any high - temperature Debye fit.

6.1 Results and discussion

6.1.1 Structure Analysis

The crystal structure of $Ca_{10}Cr_7O_{28}$ has been discussed in the previous chapter and is built up by distorted Kagome bilayers of Cr^{5+} - Cr^{6+} ions stacked along the c-axis in the trigonal space group - R-3c [32][104]. Room temperature powder X - Ray diffraction pattern (PXRD) along with Rietveld refinement for $Ca_{10}(Cr_{1-x}V_x)_7O_{28}$ with different vanadium concentrations x = 0.0, 0.1, 0.2, and 0.3 is shown in Fig-6.1. Similar

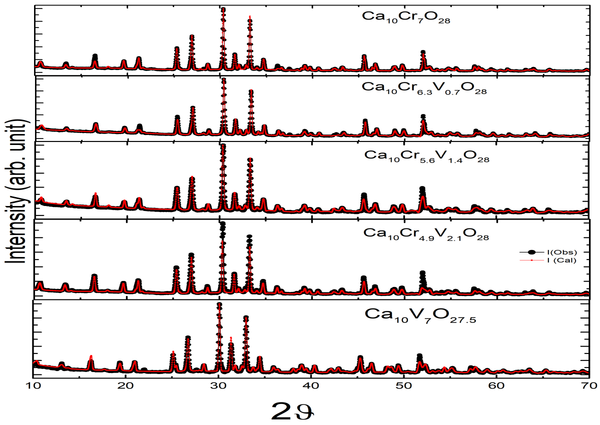

Figure 6.1: Powder X-ray diffraction pattern for $Ca_{10}(Cr_{1-x}V_x)_7O_{28}$ (x = 0, 0.1, 0.2 and 0.3) and $Ca_{10}V_7O_{27.5}$. The solid circles represent the observed data, the solid lines through the data represent the fitted pattern.

PXRD pattern was found for all samples. The crystal structure of parent and doped compound were refined, and the best-fitted parameters obtained from Rietveld refinements are listed in Table-6.1, 6.2, 6.3, and 6.4. The target concentration of vanadium was matched well with the refined fractional occupation of Cr and V. We tried $Ca_{10}Cr_7O_{28}$ lattice model for different vanadium positions assuming that the V^{5+} could sit only at the Cr^{5+} sites (Cr1 and Cr2). A linear increase in lattice constants "a = b" and "c" with an increase in vanadium concentration was found, which is shown in the Fig:6.2(a).

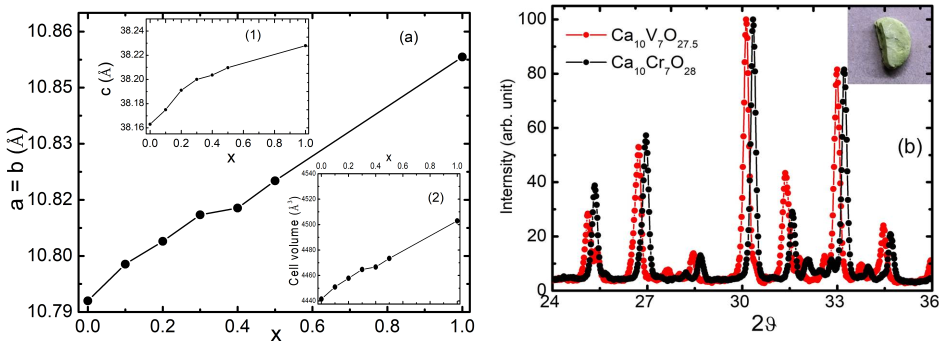

Figure 6.2: (a) Variation of lattice constant "a = b" as a function of vanadium doping. Inset-1 and Inset-2 show variation of lattice constant "c" and cell-volume versus vanadium doping x respectively for $Ca_{10}(Cr_{1-x}V_x)_7O_{28}$ ($0 \leq x \leq 0.5$) and $Ca_{10}V_7O_{27.5}$. (b) Comparision of PXRD diffraction peak positions in intensity versus 2θ graph of $Ca_{10}Cr_7O_{28}$ (black) and $Ca_{10}V_7O_{27.5}$ (red). A yellow - green pellet of $Ca_{10}V_7O_{27.5}$ is shown on the up - right corner.

An expansion in the lattice volume is consistent with the sizes of V^{5+} and Cr^{5+}

Table 6.1: Atomic parameters obtained by refining X-ray powder diffraction for $Ca_{10}Cr_{6.3}V_{0.7}O_{28}$. The lattice constants are a = b = 10.797(8) Å, c = 38.175(3) Å, α = β = 90° and γ = 120°. χ^2 = 1.43, R_{exp} = 7.58%, R_{wp} = 10.87%

Atom	Wyck	x	y	z	Occ.	B (Å^2)
Ca1	36f	0.29(4)	0.160(5)	-0.061(4)	1	0.008
Ca2	36f	0.19(8)	-0.18(5)	-0.006	0.99	0.0071
Ca3	36f	0.39	0.18(2)	0.03(2)	1	0.0086
Ca4	12c	0.66(6)	0.33(3)	0.08(7)	1	0.0099
Cr1	36f	0.31(8)	0.14(7)	0.13(2)	0.95(4)	0.0040
V1	36f	0.31(8)	0.14(7)	0.13(2)	0.03(5)	0.0040
Cr2	36f	0.17(4)	-0.13	-0.09(8)	0.92(2)	0.00118
V2	36f	0.17(4)	-0.13	-0.09(8)	0.06(8)	0.00118
Cr3A	12C	0.00	0.00	-0.099(3)	0.75	0.025
Cr3B	12C	0.00	0.00	0.53	0.24(8)	0.025
O3A	12c	0.00	0.00	-0.45(3)	0.72(3)	0.001
O3B	12c	0.00	0.00	-0.60(9)	0.29(3)	0.009
O1	36f	0.27(7)	0.08(5)	0.094(7)	0.84	0.0192
O2	36f	0.25(7)	0.22(5)	0.14(2)	1	0.0110
O3	36f	0.26	-0.01(9)	0.15	1	0.0395
O4	36f	0.48(5)	0.23(8)	0.13(9)	1	0.0008
O5	36f	0.15(3)	-0.14	-0.05(7)	1	0.033
O6	36f	0.25(4)	-0.24(6)	-0.10(9)	1	0.0081
O7	36f	0.28(7)	-0.05(8)	-0.11(7)	1	0.0094
O8	36f	0.01	0.21	0.11(5)	1	0.0131
O9	36f	-0.098	0.1401	0.0125	1	0.0131

ions, where the larger V^{5+} (0.355 Å) replaces the smaller Cr^{5+} (0.345 Å) ion in $Ca_{10}(Cr_{1-x}V_x)_7O_{28}$. PXRD data of $Ca_{10}V_7O_{27.5}$, is shown in Fig-6.1 and the absence of any extra diffraction peak, confirms the single-phase purity. A brittle yellow-green polycrystalline pellet of $Ca_{10}V_7O_{27.5}$ is shown in the Fig-6.2(b). The Rietveld refinement with $Ca_{10}Cr_7O_{28}$ lattice model was successful. An increase in lattice constant (cell volume about 1.16 %) was found, as we increase the vanadium concentration

Table 6.2: Atomic parameters obtained by refining X-ray powder diffraction for $Ca_{10}Cr_{5.6}V_{1.4}O_{28}$. The lattice constants are a = b = 10.803(9) Å, c = 38.191(1) Å, α = β = 90° and γ = 120°. χ^2 = 1.28, R_{exp} = 4.35%, R_{wp} = 5.6%

Atom	Wyck	x	y	z	Occ.	B (Å^2)
Ca1	36f	0.2866	0.1569	-0.604	1	0.008
Ca2	36f	0.2119	0.1831	-0.0012	1	0.0071
Ca3	36f	0.3887	0.1905	0.0356	1	0.0086
Ca4	12c	0.6667	0.3333	0.1019	1	0.0099
Cr1	36f	0.3113	0.1491	0.1334	0.84	0.009
V1	36f	0.3113	0.1491	0.1334	0.15	0.009
Cr2	36f	0.1782	-0.1318	-0.0997	0.92	0.005
V2	36f	0.1782	-0.1318	-0.0997	0.08	0.005
Cr3A	12C	0.0000	0.0000	-0.0064	0.72	0.002
Cr3B	12C	0.0000	0.0000	0.0144	0.27	0.025
O3A	12c	0.000	0.000	-0.0308	0.72	0.001
O3B	12c	0.000	0.000	-0.0726	0.35	0.009
O1	36f	0.2886	0.1236	0.0873	0.84	0.0192
O2	36f	0.2099	0.2155	0.141	1	0.0110
O3	36f	0.4932	-0.0355	0.1486	1	0.0395
O4	36f	0.1183	0.2562	0.1463	1	0.0008
O5	36f	0.2531	-0.1642	-0.0533	1	0.033
O6	36f	0.3240	-0.2504	-0.1093	1	0.0081
O7	36f	0.0039	0.0608	-0.1103	1	0.0094
O8	36f	-0.0134	0.2271	-0.1143	1	0.0131
O9	36f	-0.0998	0.1401	0.0125	1	0.0131

from x = 0 to 1 ($Ca_{10}V_7O_{27.5}$) as shown in the Fig-6.2(a). As compared to the parent compound, a small broadening and shifting of the diffraction peaks towards the lower 2θ were found as shown in the Fig-6.2(b) consistent with a lattice expansion.

Table 6.3: Atomic parameters obtained by refining X-ray powder diffraction for $Ca_{10}Cr_{4.9}V_{2.1}O_{28}$. The lattice constants are a = b = 10.811(3) Å, c = 38.2(5) Å, $\alpha = \beta = 90°$ and $\gamma = 120°$. χ^2 = 1.22, R_{exp} = 41.87%, R_{wp} = 34.37%

Atom	Wyck	x	y	z	Occ.	B (Å^2)
Ca1	36f	0.3004	0.1645	-0.0638	1	0.008
Ca2	36f	0.1980	-0.1887	-0.008(5)	1	0.0071
Ca3	36f	0.3749	0.1800	0.0352	1	0.0086
Ca4	12c	0.6667	0.333	0.1026	1	0.0099
Cr1	36f	0.3152	0.1373	0.1342	0.81(4)	0.0018
V1	36f	0.3152	0.1373	0.1342	0.18(5)	0.0018
Cr2	36f	0.1738	-0.1357	-0.0988	0.90	0.011
V2	36f	0.1738	-0.1357	-0.0988	0.10	0.011
Cr3A	12C	0.0000	0.0000	-0.0019	0.69	0.025
Cr3B	12C	0.0000	0.0000	0.0197	0.31	0.025
O3A	12c	0.000	0.000	-0.0371	0.69	0.001
O3B	12c	0.000	0.000	-0.0688	0.30(5)	0.009
O1	36f	0.2849	0.0915	0.0903	0.84	0.019(2)
O2	36f	0.2363	0.2482	0.1439	1	0.0110
O3	36f	0.2732	-0.0211	0.1531	1	0.0395
O4	36f	0.4860	0.2328	0.1409	1	0.0008
O5	36f	0.1530	-0.1186	-0.0556	1	0.033
O6	36f	0.2492	-0.2420	-0.1068	1	0.0081
O7	36f	0.3049	-0.0424	-0.1106	1	0.0094
O8	36f	0.0232	-0.2156	0.1200	1	0.0131
O9	36f	-0.0978	0.1401	0.0125	1	0.0131

6.1.2 Magnetic Susceptibility

DC magnetic susceptibility $\chi = M/H$ as a function of temperature at applied magnetic field H = 0.1 T for $Ca_{10}(Cr_{1-x}V_x)_7O_{28}$ ($0 \leq x \leq 0.5$) and $Ca_{10}V_7O_{27.5}$ are shown in Fig.-6.3. No long-range magnetic ordering was found in any sample down to the lowest temperature measured. The inset of Fig-6.3 shows the low - temperature (2 - 12 K) variation of χ for all samples, where a clear decreasing trend in χ for an in-

Table 6.4: Atomic parameters obtained by refining X-ray powder diffraction for $Ca_{10}V_7O_{27.5}$. The lattice constants are a = b = 10.85(3) Å, c = 38.22(7) Å, $\alpha = \beta = 90°$ and $\gamma = 120°$. $\chi^2 = 1.135$, $R_{exp} = 47.02\%$, $R_{wp} = 53.41\%$

Atom	Wyck	x	y	z	Occ.	B (Å^2)
Ca1	36f	0.2850	0.1582	-0.0605	1	0.008
Ca2	36f	0.1973	-0.1963	-0.006	1	0.0071
Ca3	36f	0.3878	0.1817	0.0345	1	0.0086
Ca4	12c	0.6667	0.3333	0.1004	1	0.0099
V1	36f	0.3108	0.1400	0.1328	1	0.00709
V2	36f	0.1781	-0.1363	-0.0991	1	0.0119
V3A	12C	0.0000	0.0000	0.0018	0.69(5)	0.0178
V3B	12C	0.0000	0.0000	0.0267	0.30(5)	0.002987
O3A	12C	0.0000	0.0000	0.0419	0.69(5)	0.00178
O3B	12C	0.0000	0.0000	0.0673	0.30(5)	0.002987
O1	36f	0.2825	0.0882	0.0908	1	0.0192
O2	36f	0.2354	0.2354	0.1464	1	0.0110
O3	36f	0.2772	-0.0154	0.1545	1	0.0395
O4	36f	0.4905	0.2456	0.1421	1	0.0008
O5	36f	0.1515	-0.1249	-0.0557	1	0.033
O6	36f	0.2564	-0.2373	-0.1095	1	0.0081
O7	36f	0.3013	-0.0339	-0.1115	1	0.0094
O8	36f	0.0148	0.2215	-0.1174	1	0.0131
O9	36f	-0.0044	0.1451	0.0138	1	0.0131

crease in vanadium doping was found. This decrease in χ results from the partial doping of nonmagnetic vanadium in the parent compound $Ca_{10}Cr_7O_{28}$. Qualitatively, the low - temperature data can be explained by the reduction of the number of spins as Cr^{5+} is replaced by nonmagnetic V^{5+}. As we already described in PXRD section the V^{5+} most likely substitutes at the Cr^{5+} site, so we have used the modified chemical formula $Ca_{10}(Cr_{1-x}V_x)^{5+}{}_6Cr^{6+}O_{28}$ for calculation of effective magnetic moment per chromium for the whole series of doping. The high - temperature data were found to follow a Curie-Weiss behavior. The χ(T) for $T \geq 100$ K were fit by the Curie-Weiss

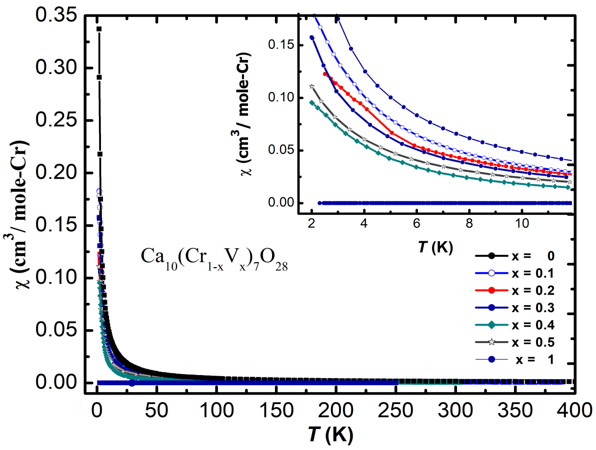

Figure 6.3: (color line) (a) DC Magnetic susceptibility χ as a function of temperature T(K) for $\mathrm{Ca_{10}(Cr_{1-x}V_x)_7O_{28}}$ ($0 \leq$ x ≤ 0.5) and $\mathrm{Ca_{10}V_7O_{27.5}}$ at applied magnetic field H = 0.1 T. Inset shows the DC magnetic susceptibility versus temperature in the low - temperature range 2 - 14 K.

expression $\chi = \chi_0 + C/(T - \theta)$ where χ_0, C, and θ are the fitting parameters. The parameters obtained from the fit to the data for each sample $\mathrm{Ca_{10}(Cr_{1-x}V_x)_7O_{28}}$ ($0 \leq$ x ≤ 0.5) are given in Table 6.5. A monotonic reduction of the Curie-Weiss temperature observed which suggests that the ferromagnetic exchange interactions weaken and antiferromagnetic exchange are strengthened with an increase in vanadium content. This reduction of θ in $\mathrm{Ca_{10}(Cr_{1-x}V_x)_7O_{28}}$ ($0 \leq$ x ≤ 0.5) is opposite to the trend found in high - pressure measurements, where an increase in θ from 2 to 8 K was found [104].

	$\chi_0 \frac{10^{-5} cm^3}{Cr-mol}$	θ (K)	C $\frac{cm^3 K}{Cr-mol}$	C (expected) $\frac{cm^3 K}{Cr-mol}$
x = 0	-1.41 (3)	3.8 (5)	0.31 (1)	0.32
x = 0.1	-1.13 (7)	3.19 (2)	0.298(4)	0.315
x = 0.2	-1.161(2)	2.56 (7)	0.293 (2)	0.308
x = 0.3	-1.366(3)	1.9 (3)	0.283(3)	0.298
x = 0.4	-1.894(1)	1.2 (1)	0.274 (6)	0.286
x = 0.5	-1.945(6)	0.9(2)	0.263(3)	0.268

Table 6.5: Parameters obtained by Curie-Weiss fit of magnetic susceptibility of $\mathrm{Ca_{10}(Cr_{1-x}V_x)_7O_{28}}$ ($0 \leq$ x ≤ 0.5) in the temperature range 100 - 400 K.

Since vanadium substitution leads to an expansion of the lattice, the above trends of θ suggest a way of tuning θ with a pressure or chemical pressure. In Fig-6.3, we have also shown the diamagnetic susceptibility of $\mathrm{Ca}_{10}V_7\mathrm{O}_{27.5}$ as a function of temperature, as expected for a nonmagnetic material.

6.1.3 Heat capacity

The temperature dependence of the zero magnetic field heat capacity of $\mathrm{Ca}_{10}(\mathrm{Cr}_{1-x}\mathrm{V}_x)_7\mathrm{O}_{28}$ ($0 \leq x \leq 0.5$) and $\mathrm{Ca}_{10}\mathrm{V}_7\mathrm{O}_{27.5}$ samples are shown in Fig-6.4. The inset of Fig-6.4 shows the low - temperature heat capacity variation of all doped samples. An upturn below T_p = 3 K in $\mathrm{Ca}_{10}Cr_7\mathrm{O}_{28}$ is consistent with the previous reports [32]. In the parent compound, this upturn indicates the onset of coherent quantum fluctuations T_p = 3 K. With vanadium substitution low - temperature upturn is suppressed in magnitude and shifted towards lower temperature side but retains its shape. The arrow (light grey) in Fig-6.4 indicates the change in peak position with increasing vanadium concentration. It is also seen that the heat capacity value decreases about half of the value for 50% vanadium content. The magnetic field dependence of low - temperature upturn for $\mathrm{Ca}_{10}(\mathrm{Cr}_{1-x}\mathrm{V}_x)_7\mathrm{O}_{28}$, x = 0.1, 0.2, 0.3 and 0.4 are shown in Fig-6.5(a) - (e). The temperature of the peak T_P as a function of magnetic field H is plotted in the Fig-6.5(f). At high magnetic fields ($\mathrm{H} \geq 3$ T), a linear magnetic field dependence of T_p was found for all samples. The zero field C/T versus T for $\mathrm{Ca}_{10}(\mathrm{Cr}_{1-x}\mathrm{V}_x)_7\mathrm{O}_{28}$

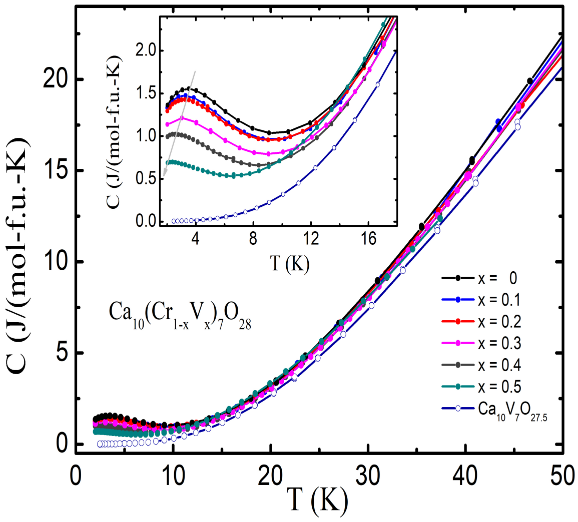

Figure 6.4: (a) Heat capacity C versus temperature T(K) for $\mathrm{Ca}_{10}(\mathrm{Cr}_{1-x}\mathrm{V}_x)_7\mathrm{O}_{28}$ ($0 \leq x \leq 0.5$) and $\mathrm{Ca}_{10}\mathrm{V}_7\mathrm{O}_{27.5}$ up to 50 K. The Inset shows C(T) for all doped samples in the temperature range 2 - 18 K.

and $Ca_{10}V_7O_{27.5}$ is shown in the Fig:6.6. Consistent with DC magnetic susceptibility results, no sharp anomaly is observed, suggesting the absence of long-range spin ordering. The availability of a perfect nonmagnetic analog $Ca_{10}V_7O_{27.5}$ of $Ca_{10}Cr_7O_{28}$,

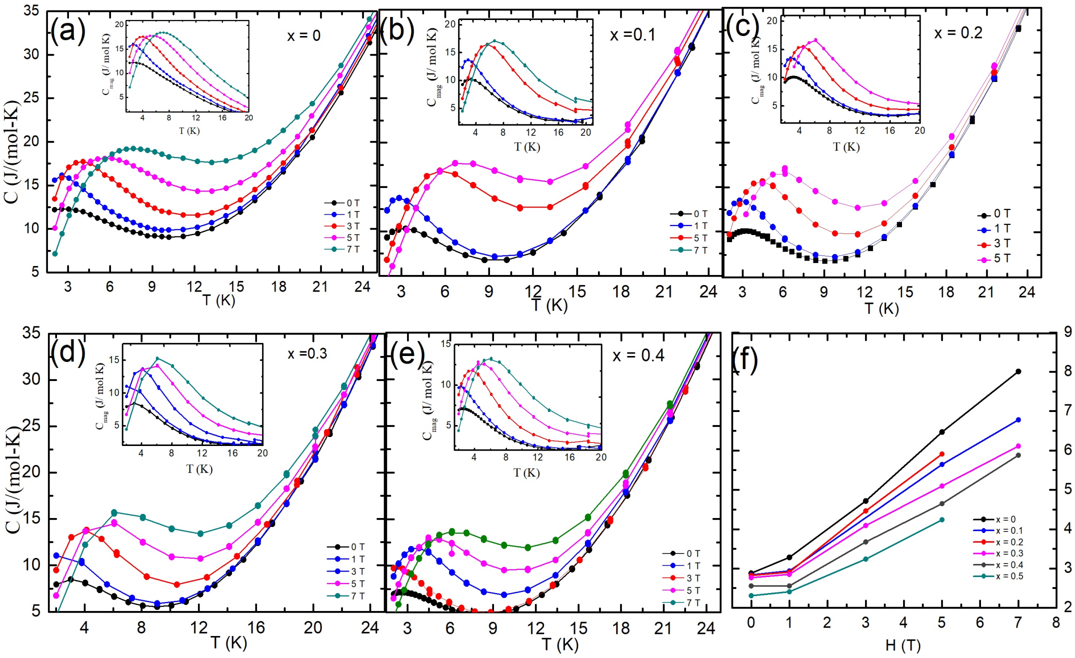

Figure 6.5: a-e: C versus T for $Ca_{10}(Cr_{1-x}V_x)_7O_{28}$ $(0 \leq x \leq 0.5)$ and $Ca_{10}V_7O_{27.5}$ up to 25 K measured at different magnetic fields. The insets show C_{mag} vs T data for respective samples. (f) Peak position T_p vs magnetic field H(T) for $Ca_{10}(Cr_{1-x}V_x)_7O_{28}$.

enables an accurate subtraction of the lattice heat-capacity without any high - temperature Debye fit. The approximate lattice contribution was obtained by measuring the heat-capacity of $Ca_{10}V_7O_{27.5}$, and then rescaling this data to account for the molecular mass difference between the vanadium doped samples and $Ca_{10}V_7O_{27.5}$(similar to previous chapters). The lattice heat capacity C(T) for $Ca_{10}V_7O_{27.5}$ can be converted to the lattice C(T) for doped smaples by multiplying the temperature (T) for C(T) data of $Ca_{10}V_7O_{27.5}$ by the factor (θ_D of $Ca_{10}V_7O_{27.5}$ / θ_D of $Ca_{10}(Cr_{1-x}V_x)_7O_{28})^{1/2}$, where θ_D is Debye temperature. The magnetic heat capacity C_{mag}/T of the parent and doped samples have been obtained by subtracting the rescaled heat capacity of $Ca_{10}V_7O_{27.5}$ from C(T) data for $Ca_{10}(Cr_{1-x}V_x)_7O_{28}$. The variation of C_{mag}/T versus T is shown in Fig-6.7.

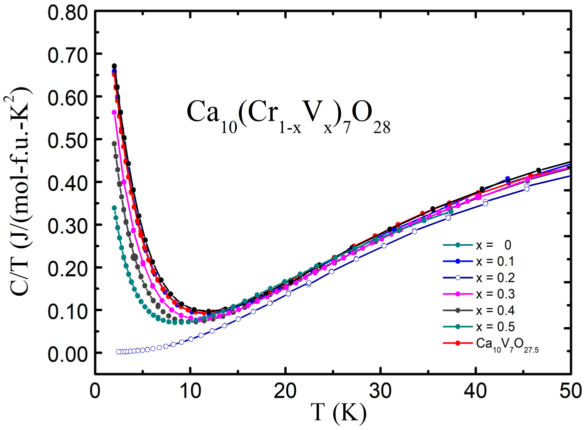

Figure 6.6: (C/T versus T for $Ca_{10}(Cr_{1-x}V_x)_7O_{28}$ ($0 \leq x \leq 0.5$) and $Ca_{10}V_7O_{27.5}$ up to 50 K.

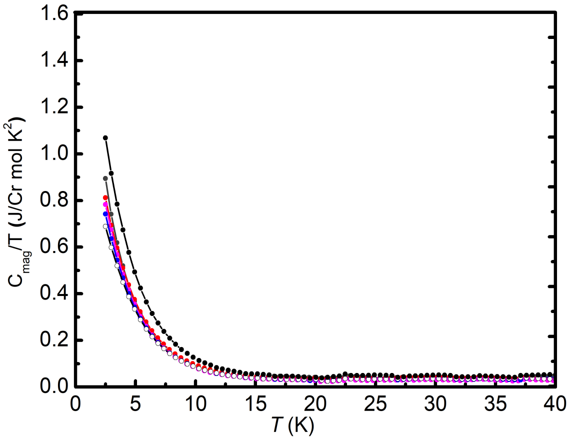

Figure 6.7: (For per magnetic Cr): Magnetic heat capacity C_{mag}/T versus temperature T(K) for $Ca_{10}(Cr_{1-x}V_x)_7O_{28}$ ($0 \leq x \leq 0.5$) at H = 0 from 2 - 40 K.

6.2 Summary

We have grown polycrystalline samples of vanadium-doped $Ca_{10}(Cr_{1-x}V_x)_7O_{28}$ ($0 \leq x \leq 0.5$) and $Ca_{10}V_7O_{27.5}$. Further, we characterized them using Powder X - ray diffraction, magnetic susceptibility, and heat capacity measurements between 2 K and 300 K and in magnetic fields of up to 9 T.

PXRD shows that the V substituted samples crystallize in the same structure as the parent material. A monotonic increase in cell volume is observed with an increase in Vanadium content. Magnetic susceptibility analysis shows the monotonic decrease in Curie constant and the decrease of Curie-Weiss temperature for 4 K to 0.1 K. The heat capacity measurements on the doped samples show the low - temperature hump similar to the parent material despite decreasing in magnitude and shifting towards the lower values of temperature. These heat capacity results are consistent with the magnetic results. The understanding of the present observations with correct lattice subtraction (without high - temperature fit) in heat capacity brings new challenges for the existing theoretical scenarios of quantum spin-liquid state in $Ca_{10}Cr_7O_{28}$.

Chapter 7

Summary

In this thesis, we have investigated the effect of perturbations like doping, pressure and magnetic field on the QSL state in 3-dimensional hyperkagome $Na_4Ir_3O_8$ and kagome bilayer compound $Ca_{10}Cr_7O_{28}$. Our work on $Na_4Ir_3O_8$, and $Ca_{10}Cr_7O_{28}$ provides several new results which we summarize below:

► $Na_4Ir_3O_8$ is of particular interest because of its 3-dimensional lattice structure. Most of the QSL candidate materials were found to have a low dimensional character. The minimal Hamiltonian required to describe the observed magnetic properties of $Na_4Ir_3O_8$ is still under debate. The hyperkagome is a unique lattice that became a playground for both theorists and experimentalist to understand the mechanism of QSL state or quantum frustration in higher dimensions. We have addressed the bond-disordered QSL state by introducing holes, magnetic and nonmagnetic impurities in polycrystalline $Na_4Ir_3O_8$. The results of different doping are listed below:.

(a) We have synthesized Na deficient samples $Na_{4-x}Ir_3O_8$ (x = 0, 0.1, 0.3, 0.7) having the hyperkagome structure with the cubic space group symmetry $P4_232$. The extended heat capacity measurements on the x = 0 parent compound down to T = 100 mK do not show any magnetic transition. This firmly establishes $Na_4Ir_3O_8$ as a strong spin-liquid candidate material. The hole doped $Na_{4-x}Ir_3O_8$ (x = 0, 0.3, 0.7) showed that the strongly frustrated Mott insulating state in $Na_4Ir_3O_8$ is quite robust against the large removal of Na (x = 0.7) from the lattice. The broad anomaly in the magnetic heat capacity observed in the parent (x = 0) compound around T = 30 K remains and still seen for x = 0.7 with slightly decrease in magnitude. Unfortunatly, the parent and doped compounds showed spin freezing at T $\approx$ 6 K in the magnetic measurements.

(b) To explore the bond-disordered spin liquid states, we disturbed the magnetic interactions between the Ir atoms on $Na_4Ir_3O_8$ by replacing it from magnetic (Ru, S = 1) and nonmagnetic (Ti) impurities. Our PXRD results confirmed the doping of Ru/Ti with a decrease in the lattice constants. For $Na_4(Ir_{1-x}Ru_x)_3O_8$ (x = 0, 0.05, 0.1 and 0.3), the Ru substitution leads to an increase in the average effective moment, suggesting that Ru dopants go in as localized moments. The increasing disorder (Ru) in the partially substituted samples leads to an enhancement in freezing temperature T_f from 6 K (x = 0) to 12.4 K for x = 0.2. This variation of T_f also suggests that the parent material is inherently disordered and efforts to synthesize less disordered $Na_4Ir_3O_8$ should be made to reveal the true ground state. Interestingly, the analysis of magnetic and thermal measurement of nonmagnetic (Ti) doping on $Na_4Ir_{2.7}Ti_{0.3}O_8$ revealed the "orphan spin-liquid state." In addition, a smaller Weiss temperature showed that the magnetic correlations became weak and the spin-freezing (T_f) was pushed to much lower temperature $T_f \approx 2.3$ K. Since the partial substitution for Ir by Ru/Ti in $Na_4Ir_3O_8$ leads to positive chemical pressure, therefore, the contrasting effects on the magnetic properties of $Na_4Ir_3O_8$ must be due to the kind of bond-disorder (magnetic or non-magnetic) introduced by their substitution.

► In the continuation of the QSL materials study in higher dimensions, we have addressed the effect of perturbations: hydrostatic pressure and nonmagnetic doping in the kagome bilayer QSL candidate material $Ca_{10}Cr_7O_{28}$. Generally, frustrated lattices with the anti-ferromagnetic exchange are considered as essential ingredients for QSL. $Ca_{10}Cr_7O_{28}$ provides a new direction in the field of QSL, where dominant ferromagnetic interactions within the kagome bilayer are responsible for QSL state. $Ca_{10}Cr_7O_{28}$ is a kagome bilayer compound develops a novel frustration mechanism, where competing ferro and antiferromagnetic exchange interactions within a kagome bilayer suppress the possibility of long-range magnetic order. Both experimental and theoretical results strongly suggest the signatures of a QSL ground state in $Ca_{10}Cr_7O_{28}$.

(a) With the motivation of disturbing the exchange interactions within and between the kagome bilayers, we have synthesized polycrystalline samples of $Ca_{10}Cr_7O_{28}$ and studied in detail its temperature-dependent magnetic susceptibility at ambient and high pressure, isothermal magnetization, and temperature and magnetic field-dependent heat capacity measurements. The ambient pressure magnetic measurements indicate the presence of both ferromagnetic (FM) and antiferromagnetic (AFM) exchange interactions with the FM interactions dominating. The net magnetic scale was found about $\sim$ 10 - 15 K. High-pressure magnetic susceptibility measurements up to P $\approx$ 1 GPa revealed that the QSL state at ambient pressure is quite robust and may not depend on a delicate balance between any specific values of competing exchange interactions. Additionally, our results indicate that at high pressure the relative strength of ferromagnetic interactions increases as evidenced by an increase in the value of the Weiss temperature from θ = 4 K at P = 0 to θ = 7 K at P = 1 GPa.

(b) We have also studied the nonmagnetic (V) doping in $Ca_{10}(Cr_{1-x}V_x)_7O_{28}$ ($0 \leq x \leq 0.5$). We have also synthesized a new nonmagnetic analog $Ca_{10}V_7O_{27.5}$ of $Ca_{10}Cr_7O_{28}$, which enables an accurate estimation of lattice heat capacities without any high-temperature Debye fit. A monotonic reduction of the Curie-Weiss temperature (θ) suggests that the ferromagnetic exchange interactions are weaken and antiferromagnetic exchange are strengthened in $Ca_{10}Cr_7O_{28}$ with an increase in V concentration. This reduction of θ in $Ca_{10}(Cr_{1-x}V_x)_7O_{28}$ was opposite to the trend found in high-pressure measurements. Since V substitution leads to an expansion of the lattice, the above trends of θ suggests a way of tuning magnetic properties of $Ca_{10}Cr_7O_{28}$ with hydrostatic pressure or chemical pressure. The magnetic heat capacity measurements revealed a linear magnetic field dependence of low-temperature hump for all doped samples.

Appendix A

Spin-liquid like Raman signatures in the hyperkagome iridate $Na_4Ir_3O_8$

$Na_4Ir_3O_8$ has spurred a lot of theoretical interest as a QSL candidate [88][70][89][91]. Most of these works strongly suggest the Heisenberg model on the hyperkagome lattice. Recently the Kitaev-Heisenberg model on hyperkagome iridate $Na_4Ir_3O_8$ showed that the Kitaev spin liquid exact solution does not generalize to this lattice [105]. For $Na_4Ir_3O_8$, the more appropriate model whether the Kitaev or Heisenberg is still an open question.

In collaboration with the group of Prof. A. K. Sood at IISC Bengaluru, we studied inelastic light scattering using Raman spectroscopy on the polycrystalline samples of $Na_4Ir_3O_8$. The combine calculation of Raman scattering measurements with mean-field calculations of the Raman response show that the Kitaev-like magnetic exchange is dominant in the hyperkagome iridate. In contrast to the previous study [105], results of the Kitaev-Heisenberg model on the hyperkagome lattice shows that the experimental observations are consistent with the calculated Raman response where the Kitaev exchange interaction (J_K) is much larger than the Heisenberg term J_1 ($J_1/J_K \approx 0.1$)[92].

In this work, we have experimentally shown the existence of a broad Raman band (BRB) at $\sim$ 3500 cm^1 with a large bandwidth of $\sim$ 1700 cm^1. By calculating the Raman response for the Kitaev-Heisenberg model on the hyperkagome lattice, we showed that the observed BRB is in very good agreement with the calculated Raman response for the Kitaev limit with small Heisenberg perturbations (J_1/J_K = 0.1). Although the

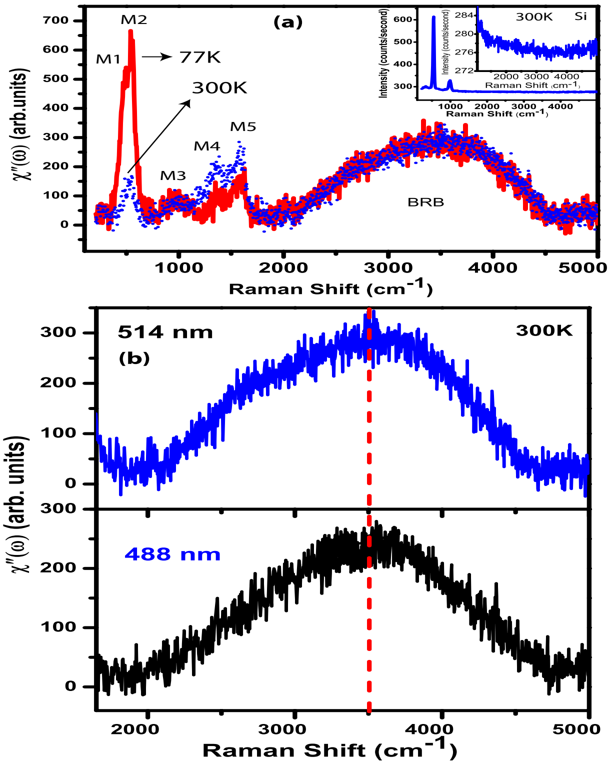

Figure A.1: (a) Raman spectra of $Na_4Ir_3O_8$ measured at T = 77 K (red line) and 300 K (blue circles) in the spectral range 100 - 5000 cm^{1} using an excitation laser wavelength of 514.5 nm. Inset: Raman spectra of silicon at 300 K. The sharp lines near 520 and 1040 cm^{1} are first and second-order Raman modes of Si, respectively. The magnified Si spectra from 1000 to 5000 cm^{1} is shown in the inset. (b) Raman spectra recorded with two different laser excitation lines 514.5 and 488 nm. The vertical dashed line shows the center of the BRB. [92].

Kitaev limit is not exactly solvable for the hyperkagome lattice, we find a spin liquid state for the parameters used to calculate the Raman response which matches the experiments. This strongly suggests that $Na_4Ir_3O_8$ is a spin liquid driven by strong Kitaev interactions with smaller Heisenberg terms. More details can be found in Phys. Rev. B 94, 155153 (2016)[92].

Appendix B

Spin dynamics in $Na_{4-x}Ir_3O_8$ (x = 0.3 and 0.7) investigated by ^{23}Na NMR and μSR

In this appendix, we summarize the highlights of the results of ^{23}Na Nuclear magnetic resonance (NMR) and muon spin relaxation (μSR) measurements performed on the sodium depleted $Na_{4-x}Ir_3O_8$ for x = 0.3 and 0.7. These results are used to describe the spin dynamics and support the proposed fermionic statistics of a spin-liquid ground state with spinon Fermi surfaces for hyperkagome $Na_4Ir_3O_8$ [70][71]. These results were published in the Journal of Phys.:Condens. Matter [99].

B.1 ^{23}Na NMR results on $Na_{4-x}Ir_3O_8$ (x = 0.3 and 0.7)

We discussed in the third chapter that the laboratory x-ray measurements were not sufficient to differentiate between the structure of $Na_{4-x}Ir_3O_8$ and $Na_3Ir_3O_8$. The only difference between the structures of these two materials is the number of Na positions. $Na_4Ir_3O_8$ has three distinct Na positions while $Na_3Ir_3O_8$ has two. Only one of the Na positions is common between the two structures as shown Table-3.1 and Table-3.2. Removing Na from $Na_4Ir_3O_8$ can lead to a two-phase mixture of $Na_4Ir_3O_8$ and $Na_3Ir_3O_8$ [66] [90]. For confirming the $Na_4Ir_3O_8$ phase purity, the ^{23}Na NMR measurement at applied field H = 6 Tesla in the temperature range of T = 2 - 360 K performed in IFW Dresden, Germany.

B. Spin dynamics in $Na_{4-x}Ir_3O_8$ (x = 0.3 and 0.7) investigated by ^{23}Na NMR and μSR

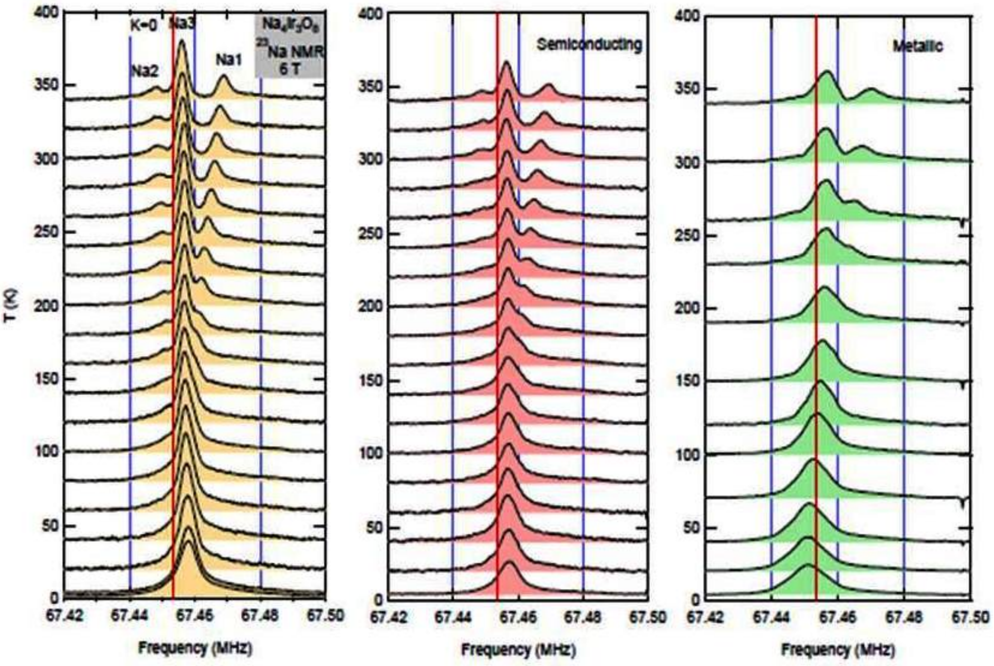

Figure B.1: (From left to right) Temperature dependence of the ^{23}Na NMR spectra of $Na_4Ir_3O_8$, $Na_{3.7}Ir_3O_8$ (x=0.3, semimetallic) and $Na_{3.3}Ir_3O_8$ (x=0.7, metallic) measured at H = 6 T.

The temperature dependence of the ^{23}Na NMR on parent compound $Na_4Ir_3O_8$ and for the depleted $Na_{3.7}Ir_3O_8$ (x = 0.3) and $Na_{3.3}Ir_3O_8$ (x = 0.7) is shown in Fig: B.1. At high-temperature, Well separated three Na peaks correspond to the three different crystallographically Na sites [Na1: Na2: Na3] with the ratio 4:3:9 [66]. These three Na lines confirm the single phase ($Na_4Ir_3O_8$) purity of our samples. The temperature independent behavior of Na3 line, indicating the negligibly weak hyperfine (hf) coupling to the Ir spins, which allows calculating non-spin contribution from the spin-lattice relaxation rate.

The Na1 site in B-pyrochlore sublattice of $Na_4Ir_3O_8$ (AB_2O_4) is coupled to three Ir site. Thus the Na1 line is most sensitive to spin dynamics of Ir ions. The rightmost spectral line corresponds to the Na1, which shows strong temperature dependence in Fig: -B.1 and Fig: B.2(a). For Na1, the hf coupling constant was estimated to be -5.2 kOe per Bohr magneton. It seen from Fig: B.1 and Fig: B.2(a) that the Na-deficiency causes the inhomogeneous broadening without changing the spectral shape indicates that the depleted $Na_{3.7}Ir_3O_8$ (x = 0.3) and $Na_{3.3}Ir_3O_8$ (x = 0.7) samples don't develop a static inhomogeneous field and/or a slowly fluctuating field from electron spins.

Fig:-B.2(b) shows the absence of any static magnetism down to 2 K. For investigating the low-energy Ir spin dynamics, the spin-lattice relaxation rate ${T_1}^{-1}$ at the Na1 and Na3 sites were measured and plotted on a log-log scale in Fig:- B.2(c). For finding the total spin contribution ${T_{1,spin}}^{-1}$ in the spin-lattice relaxation rate, the non-spin Na3 site contribution is subtracted from the total spin contribution of the Na1 site is shown in B.2(d) all of the three samples x = 0, 0.3 and 0.7.

$$T_{1,spin}^{-1} = T_1^{-1}(Na1) - T_1^{-1}(Na3) \tag{B.1}$$

The power-law behavior seen in the parent compound $Na_4Ir_3O_8$ is still persisted for the Na deficient samples $Na_{3.7}Ir_3O_8$ (x = 0.3) and $Na_{3.3}Ir_3O_8$ (x = 0.7) but changes from 3 to 2.5. The similar power-law behavior has been found in the magnetic heat capacity which supports the spinon Fermi surface in the $Na_4Ir_3O_8$.

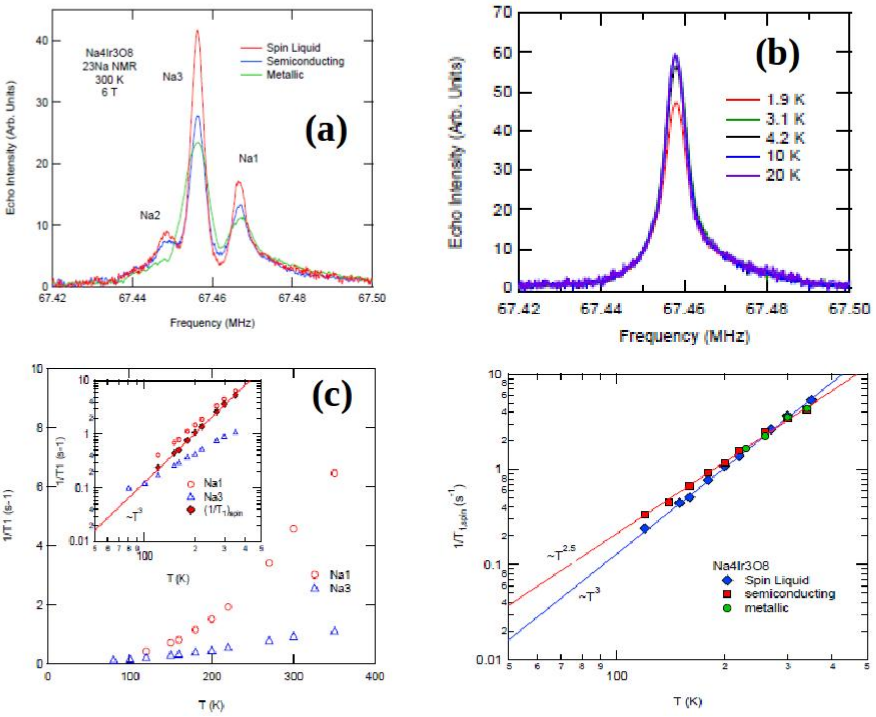

Figure B.2: (a) The three Na sites which are well resolved at high temperature 300 K for x = 0, 0.3, and 0.7 sample. (b) In low-temperature region 20-2 K, $Na_4Ir_3O_8$ doesn't develop any static magnetism. (c) Temperature dependence of ${T_1}^{-1}$ measured at Na1 and Na3 sites for $Na_4Ir_3O_8$. (d) ${T_{1,spin}}^{-1}$ versus temperature for all three samples $Na_4Ir_3O_8$, $Na_{3.7}Ir_3O_8$ (x = 0.3, semimetallic) and $Na_{3.3}Ir_3O_8$ (x = 0.7, metallic) shows the power-law behavior.

B.2 Zero-Field and longitudinal-Field μSR results on $Na_{4-x}Ir_3O_8$ (x = 0, 0.3 and 0.7)

For confirming the frustrated ground state and spin dynamics of the Na depleted samples, Zero-field (ZF) and longitudinal-field (LF) μSR measurements on $Na_{4-x}Ir_3O_8$ (x = 0.3 and 0.7) were performed using the ARGUS spectrometer of RIKEN-RAL and the EMU spectrometer of ISIS at the Rutherford Appleton Laboratory[99].

The representative ZF depolarization curves of $Na_{3.7}Ir_3O_8$ (x = 0.3) and $Na_{3.3}Ir_3O_8$ (x = 0.7) samples at selected temperatures between 1.4 and 200 K are shown in Fig:-B.3(a) and (b). In contrast to the parent compound, $Na_4Ir_3O_8$ depolarization curves for Na depleted samples exhibit a very slow depolarization with no static electronic moments for temperatures down to T = 1.4 K. This indicates as a result of hole dopings, a melting of the quasistatic order to a dynamic quantum state.

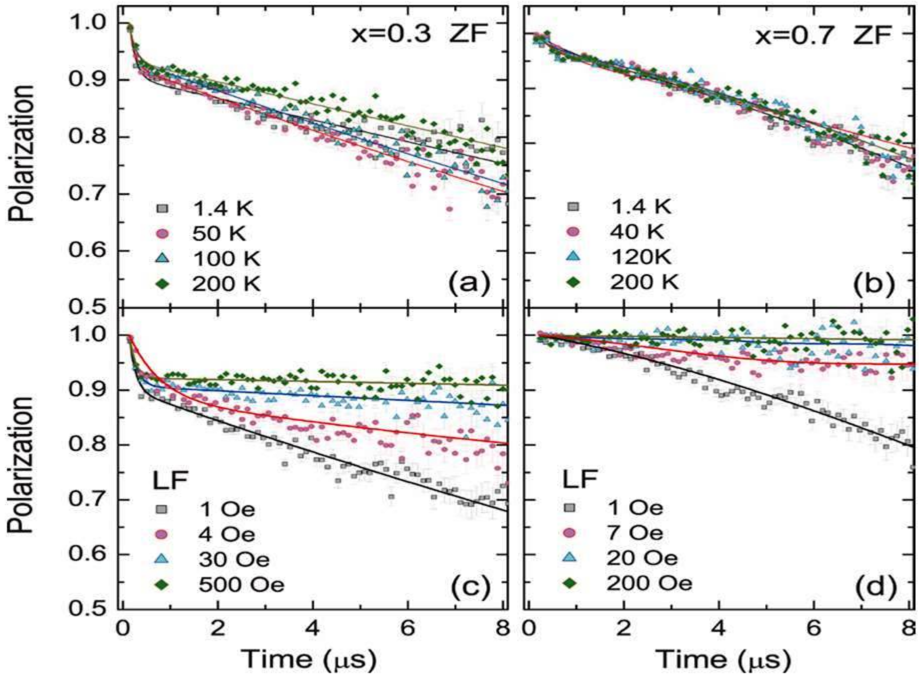

Figure B.3: (Color online) Time evolution of the ZF-μSR polarization of (a) $Na_{3.7}Ir_3O_8$ and (b) $Na_{3.3}Ir_3O_8$ at the selected temperatures between 1.4 and 200 K. Time evolution of the LF-μSR polarization of (c) $Na_{3.7}Ir_3O_8$ and (d) $Na_{3.3}Ir_3O_8$ measured at T = 1.4 K.

Time evolution of the LF-μSR polarization of $Na_{4-x}Ir_3O_8$ for x = 0.3 and 0.7 is shown in Fig:-B.3 (c) and (d) at T = 1.4 K. The field dependence of the relaxation rate allows for determining the nature of transport of spin excitations. The ZF-μSR data give evidence for a quasi-itinerant paramagnetic behavior on the tetrahedral clusters upon hole-doping. The power-law dependence of the relaxation rates at elevated temperatures, suggesting gapless spin excitations. This study indicates that intriguing charge and spinon excitations emerge in a frustrated spin system across the Mott transition, which is proposed for the hyperkagome model by Lawer[70][71].

References

[1] I. M. Khalatnikov, Introduction to the Theory of Superfluidity , Advanced Book Program, Perseus Pub (2000). 1

[2] S. Rachel, L. Fritz and M. Vojta, Landau Levels of Majorana Fermions in a Spin Liquid, Phys. Rev. Lett. **116**, 167201 (2016). URL `https://link.aps.org/doi/10.1103/PhysRevLett.116.167201`. 1

[3] K. Le Hur, A. Soret and F. Yang, Majorana spin liquids, topology, and superconductivity in ladders, Phys. Rev. B **96**, 205109 (2017), URL `https://journals.aps.org/prb/abstract/10.1103/PhysRevB.96.205109`.

[4] V. Kozii, J. W. F. Venderbos and L. Fu, Three-dimensional Majorana fermions in chiral superconductors, Science 5037,0036-8075 (2016), URL `http://advances.sciencemag.org/content/2/12/e1601835`.

[5] S.-H. Do, S.-Y. Park, J. Yoshitake, J. Nasu, Y. Motome, Y. S. Kwon, D. T. Adroja, D. J. Voneshen, K. Kim, T.-H. Jang, J.-H. Park, K.-Y. Choi and S. Ji, Majorana fermions in the Kitaev quantum spin system -RuCl$_3$, Nature Physics **13,**, 1079-1084 (2017), URL `https://www.nature.com/articles/nphys4264`.

[6] B. Bradlyn, J. Cano1, Z. Wang, M. G. Vergniory, C. Felser, R. J. Cava, B. A. Bernevig, Beyond Dirac and Weyl fermions: Unconventional quasiparticles in conventional crystals, Science Advances **2**,12 (2016), URL `http://science.sciencemag.org/content/353/6299/aaf5037`

[7] S. L. Sondhi, A. Karlhede, and S. A. Kivelson, Skyrmions and the crossover from the integer to fractional quantum Hall effect at small Zeeman energies, Phys. Rev. B **47**,24 (1993), URL `http://link.aps.org/pdf/10.1103/PhysRevB.47.16419`.

[8] S. Murakami, Phase transition between the quantum spin Hall and insulator phases in 3D: emergence of a topological gapless phase, New J. Phys. **9**,356 (2007), URL `http://iopscience.iop.org/article/10.1088/1367-2630/9/9/356/meta`. 1

[9] J. A. Hertz, Quantum critical phenomena, Phys. Rev. B **14**,1165 (1976), URL `http://link.aps.org/pdf/10.1103/PhysRevB.14.1165`. 2

[10] D. H. Reich, B. Ellman, J. Yang, T. F. Rosenbaum, G. Aeppli, and D. P. Belanger, Dipolar magnets and glasses: Neutron-scattering, dynamical, and calorimetric studies of randomly distributed Ising spins, Phys. Rev. B **42**, 4631 (1990), URL `https://link.aps.org/doi/10.1103/PhysRevB.42.4631`. 2, 5

[11] D. Bitko, T. F. Rosenbaum, and G. Aeppli, Quantum Critical Behavior for a Model Magnet, Phys. Rev. Lett **77**, 940 (1996), URL `https://link.aps.org/doi/10.1103/PhysRevLett.77.940`. 2

[12] H. M. Ronnow, R. Parthasarathy, J. Jensen, G. Aeppli, T. F. Rosenbaum, D. F. McMorrow, Quantum Phase Transition of a Magnet in a Spin Bath, Science **308**, 5720 (2005), URL `http://science.sciencemag.org/content/308/5720/389`. 2

[13] R. B. Laughlin, Quantized Hall conductivity in two dimensions, Phys. Rev. B**23**, 5632 (1981), URL `https://link.aps.org/doi/10.1103/PhysRevB.23.5632`. 3, 10

[14] R. B. Laughlin, Anomalous quantum Hall effect: An incompressible quantum fluid with fractionally charged excitations, Phys. Rev. Lett.**50**, 1395 (1983), URL `https://link.aps.org/doi/10.1103/PhysRevLett.50.1395`. 3

[15] D. B. McWhan, A. Menth, J. P. Remeika, W. F. Brinkman, and T. M. Rice,, Metal-Insulator Transitions in Pure and Doped V_2O_3, Phys. Rev. B 7, 1920 (1973). URL `https://link.aps.org/doi/10.1103/PhysRevB.7.1920` 4

[16] B.J. Kim, H. Jin, S. J. Moon, J.Y. Kim, B.-G. Park, C. S. Leem, J. Yu, T. W. Noh, C. Kim, S. J. Oh, J. H. Park, V. Durairaj, G. Cao, and E. Rotenberg, Novel J_{eff}=1/2 Mott State Induced by Relativistic Spin-Orbit Coupling in Sr_2IrO_4, Phys. Rev. Lett.01, 076402(2008), URL `https://link.aps.org/doi/10.1103/PhysRevB.7.1920`. 4

[17] G. Jackeli and G. Khaliullin, Mott Insulators in the Strong Spin-Orbit Coupling Limit: From Heisenberg to a Quantum Compass and Kitaev Models, Phys. Phys. Rev. Lett. **102**, 017205 (2009), URL `https://link.aps.org/doi/10.1103/PhysRevLett.102.017205`. 4

[18] A. Shitade, H. Katsura, J. Kunes, X.-L. Qi, S.-C. Zhang and N. Nagaosa, Quantum Spin Hall Effect in a Transition Metal Oxide Na_2IrO_3, . Phys. Rev. Lett. **102**, 256403 (2009), URL `https://link.aps.org/doi/10.1103/PhysRevLett.102.256403`. 4

[19] Y. Singh and P. Gegenwart, Antiferromagnetic Mott insulating state in single crystals of the honeycomb lattice material Na_2IrO_3, Phys. Rev. B **82**, 064412 (2010), URL `https://link.aps.org/doi/10.1103/PhysRevB.82.064412`. 4

[20] D. C. Johnston, Handbook of Magnetic Materials,, edited by K. H. J. Buschow (E), lsevier, Amsterdam, **10**, chap. 1, pp. 1-237 (1997). 4

[21] R. A. Borzi, S. A. Grigera, J. Farrell, R. S. Perry, S. J. S. Lister, S. L. Lee, D. A. Tennant, Y. Maeno and A. P. Mackenzie Formation of a Nematic Fluid at High Fields in $Sr_3Ru_2O_7$, Science **315**, 214 (2007), URL `http://adsabs.harvard.edu/abs/2007Sci...315..214B`. 4

[22] P. Fazekas, Lecture Notes on Electron Correlation and Magnetism, World Scientific Publishing Co. Pte. Ltd, (1999). 4

[23] J. A. Mydosh, Spin Glasses: An Experimental Introduction, CRC Press, 1993. 5, 22, 45, 47

[24] C. Lacroix, P. Mendels, F. Mila, -Introduction to Frustrated Magnetism: Materials, Experiments, Theory, Springer Series in Solid-State Sciences (Springer, Berlin, 2011) 5, 10

[25] A. P. Ramirez, G. P. Espinosa, and A. S. Cooper, Strong frustration and dilution-enhanced order in a quasi-2D spin glass, Phys. Rev. Lett. **64**, 2070(1990), URL `https://link.aps.org/doi/10.1103/PhysRevLett.64.2070`. 5

[26] P.W Anderson Resonating valence bonds: A new kind of insulator?, Mater.Res. **8**, 153 (1973), URL `https://www.sciencedirect.com/science/article/pii/0025540873901670`. 5, 10, 27

[27] G.H. Wannier, Antiferromagetnism. The Triangular Ising Net, Phys. Rev. B9, 2 (1950), URL `https://link.aps.org/doi/10.1103/PhysRev.79.357`. 6, 11

[28] D. E. MacLaughlin, Y. Nambu, S. Nakatsuji, R. H. Heffner, Lei Shu, O. O. Bernal, and K. Ishida, Unconventional spin freezing and fluctuations in the frustrated antiferromagnet $NiGa_2S_4$, Phys. Rev. B **78**, 220403(R) (2008), URL `https://journals.aps.org/prb/abstract/10.1103/PhysRevB.78.220403`. 6, 11

[29] Y. Shimizu, K. Miyagawa, K. Kanoda, M. Maesato, and G. Saito Spin Liquid State in an Organic Mott Insulator with a Triangular Lattice, Phys. Rev. Lett. 1, 107001(2003). IRL `http://link.aps.org/pdf/10.1103/PhysRevLett.91.107001`. 6

[30] M. Yamashita, N. Nakata, Y. Kasahara, T. Sasaki, N. Yoneyama, N. Kobayashi, S. Fujimoto, T. Shibauchi, and Y. Matsuda, Thermal-transport measurements in a quantum spin-liquid state of the frustrated triangular magnet κ-(BEDT-TTF)$_2$Cu$_2$(CN)$_3$, Nat. Phys. **5**, 44 (2009), URL `https://www.nature.com/articles/nphys1134`. 11

[31] S. Nakajima, T. Suzuki, Y. i Ishii, K. Ohishi, I. Watanabe, T. Goto, A. Oosawa, N. Yoneyama, N. Kobayashi, Microscopic Phase Separation in Triangular-Lattice Quantum Spin Magnet κ-(BEDT-TTF)$_2$Cu$_2$(CN)$_3$ Probed by Muon Spin Relaxation, J. Phys. Soc. Jpn. **81**, 063706(2012), URL `https://journals.jps.jp/doi/abs/10.1143/JPSJ.81.063706`. 6

[32] C. Balz, B. Lake, J. Reuther, H. Luetkens, R. Schonemann, T. Herrmannsdorfer, Y. Singh, A. T. M. N. Islam, E. M. Wheeler, J.A. Rodriguez-Rivera, T. Guidi, G. G. Simeoni, C. Baines and H. Ryll, Physical realization of a quantum spin liquid based on a complex frustration mechanism, Nature Physics **12**,942–949 (2016), URL `https://www.nature.com/articles/nphys3826`. 6, 53, 54, 55, 58, 60, 62, 65, 72

[33] C. Balz, B. Lake, M. Reehuis, A T M N. Islam, O. Prokhnenko, Y. Singh, P. Pattison and S. Toth, Crystal growth, structure and magnetic properties of Ca$_{10}$Cr$_7$O$_{28}$, JPCM **75(29)**, 22 (2017), URL `http://iopscience.iop.org/article/10.1088/1361-648X/aa68eb/meta`. 6, 53, 54, 55

[34] M. Tamura, A. Naka and Reizo Kato, Frustration-Induced Valence-Bond Ordering in a New Quantum Triangular Antiferromagnet Based on [Pd(dmit)$_2$], JPCM **75(9)**,093701(2006), URL `https://journals.jps.jp/doi/abs/10.1143/JPSJ.75.093701`. 6

[35] T. Itou, A. Oyamada, S. Maegawa, M. Tamura, and R. Kato, Quantum spin liquid in the spin-1/2 triangular antiferromagnet EtMe$_3$Sb[Pd(dmit)$_2$]$_2$, Phys. Rev. B **77**,104413 (2008), URL `https://link.aps.org/doi/10.1103/PhysRevB.77.104413`. 6, 11

[36] I. Syozi, Statistics of Kagome Lattice, Progress of Theoretical Physics, **3** (1951), URL `https://academic.oup.com/ptp/article-pdf/6/3/306/5239621/6-3-306.pdf`. 7

[37] S. T. Bramwell and M. J. P. Gingras, Spin Ice State in Frustrated Magnetic Pyrochlore Materials, Science **294**, 1495 (2001), URL `https://doi.org/10.1126/science.1064761`. 8

[38] S. T. Bramwell, S. R. Giblin, S. Calder, R. Aldus, D. Prabhakaran, and T. Fennell, Measurement of the charge and current of magnetic monopoles in spin ice, Nature (London)**461**, 956 (2009), URL `https://www.nature.com/articles/nature08500`. 8

[39] M. J. Harris, S. T. Bramwell, D. F. McMorrow, T. Zeiske, and K. W. Godfrey, Geometrical Frustration in the Ferromagnetic Pyrochlore $Ho_2Ti_2O_7$, Phys. Rev. Lett. **79**,2554 (1997), URL `https://link.aps.org/doi/10.1103/PhysRevLett.79.2554`. 8

[40] L. Pauling, The Structure and Entropy of Ice and of Other Crystals with Some Randomness of Atomic Arrangement, J. Am. Chem. Soc. **57**, 2680 (1935), URL `https://pubs.acs.org/doi/abs/10.1021/ja01315a102`. 8

[41] A. P. Ramirez, ,A. Hayashi, R.J. Cava, R.B. Siddharthan,and S. Shastry, Zero-point entropy in spin ice, Nature **399**, 333-336 (1999), URL `https://www.nature.com/articles/20619`. 8

[42] B. Canals and C. Lacroix. Pyrochlore Antiferromagnet: A Three-Dimensional Quantum Spin Liquid, Phys. Rev. Lett.**80**, 2933 (1998), URL `http://link.aps.org/pdf/10.1103/PhysRevLett.80.2933`. 8

[43] R. Moessner and J. T. Chalker Properties of a Classical Spin Liquid: The Heisenberg Pyrochlore Antiferromagnet, Phys. Rev. Lett.**80**, 2929 (1998), URL `http://link.aps.org/pdf/10.1103/PhysRevLett.80.2929`. 8

[44] L. Balents, Spin liquids in frustrated magnets, Nature **464**, 199-208 (2010), URL `https://www.nature.com/articles/nature08917`. 9, 10

[45] A.P. Ramirez, Quantum spin liquids: A flood or a trickle?, Nat. Phys. **4**, 442 (2008), URL `https://www.nature.com/articles/nphys978`. 9

[46] F. Mila, Quantum spin liquids, Eu.r J. Phys. **21**,6 (2000), URL `http://iopscience.iop.org/article/10.1088/0143-0807/21/6/302/meta`. 9

[47] J. D. Cloizeaux and J.J. Pearsont,, Spin-Wave Spectrum of the Antiferromagnetic Linear Chain, Phys. Rev. **128**, 5 (1962), URL `https://link.aps.org/doi/10.1103/PhysRev.128.2131`. 10, 11

[48] T. Han, J. S. Helton, S. Chu, D. G. Nocera, J. A. RodriguezRivera, C. Broholm, and Y. S. Lee, Fractionalized excitations in the spin-liquid state of a kagome-lattice antiferromagnet, Nature **492**,406 (2012), URL `https://www.ncbi.nlm.nih.gov/pubmed/23257883`. 10, 11

[49] E. Runge and P. Fulde, Charge degrees of freedom in frustrated lattice structures, Physical Review B **70**, 245113(2004), URL `https://link.aps.org/doi/10.1103/PhysRevB.70.245113`. 10

[50] P.W. Anderson, The Resonating Valence Bond State in La_2CuO_4 and Superconductivity, Science. **235**, 4793 (1987), URL `http://science.sciencemag.org/content/235/4793/1196`. 10

[51] A. P. Ramirez, STRONGLY GEOMETRICALLY FRUSTRATED MAGNETS, Annu. Rev. Mater. Sci.**24**, 1 (1994), URL `https://www.annualreviews.org/doi/abs/10.1146/annurev.ms.24.080194.002321`. 10, 12, 27

[52] D.A. Tennant, R.A. Cowley, S.E. Nagler and A.M. Tsvelik, - Measurement of the spin-excitation continuum in one-dimensional KCuF 3 using neutron scattering, Phys. Rev. B2, 13368 (1995), URL `https://link.aps.org/doi/10.1103/PhysRevB.52.13368`. 10

[53] R. Coldea, D. A. Tennant, A. M. Tsvelik, and Z. Tylczynski, Experimental Realization of a 2D Fractional Quantum Spin Liquid, Phys. Rev. Lett. **86** 1335,(2001), URL `https://journals.aps.org/prl/abstract/10.1103/PhysRevLett.86.1335`. 10, 11

[54] X.G. Wen and Q. Niu, Ground-state degeneracy of the fractional quantum Hall states in the presence of a random potential and on high-genus Riemann surfaces, Phys. Rev. B1, 9377 (1990), URL `https://link.aps.org/doi/10.1103/PhysRevB.41.9377`. 10

[55] J.S. Helton,K. Matan,M.P. Shores,E.A. Nytko,B.M. Bartlett, Y. Yoshida, Y. Takano, A. Suslov, Y. Qiu, J.-H. Chung, D. G. Nocera, and Y. S. Lee, Spin Dynamics of the Spin-1/2 Kagome Lattice Antiferromagnet $ZnCu_3(OH)_6Cl_2$, Phys. Rev. Lett. **98**,107204(2007), URL `https://link.aps.org/doi/10.1103/PhysRevLett.98.107204`. 11

[56] P. Mendels and F. Bert, Quantum Kagome Antiferromagnet $ZnCu_3(OH)_6Cl_2$, J. Phys. Soc. Jpn. **79**, 011001(2010), URL `https://journals.jps.jp/doi/abs/10.1143/JPSJ.79.011001`. 11

[57] M. Yamashita,N. Nakata,Y. i Senshu,Masaki Nagata1, M. Nagata, H. M. Yamamoto, Highly Mobile Gapless Excitations in a Two-Dimensional Candidate Quantum Spin Liquid, Science **328**, 1246 (2010), URL `http://science.sciencemag.org/content/328/5983/1246`. 11, 62

[58] S. Yamashita, Y. Nakazawa, M. Oguni, Y. Oshima,H. Nojiri,Y. Shimizu, K. Miyagawa and K. Kanoda, Thermodynamic properties of a spin-1/2 spin-liquid state in a κ-type organic salt Nat. Phys. **4**, 459(2008), URL `https://www.nature.com/articles/nphys942`. 6, 11

[59] B. Lake,D. A. Tennant, C. D. Frost and S. E. Nagler, Quantum criticality and universal scaling of a quantum antiferromagnet, Nature materials, **4** 1327,(2005), URL `https://www.nature.com/articles/nmat1327`. 11

[60] J.-W. Mei, Ji-Y. Chen,H. He and X.-G. Wen, Gapped spin liquid with Z_2 topological order for the kagome Heisenberg model, Phys. Rev. B **95**, 235107 (2017), URL `https://link.aps.org/doi/10.1103/PhysRevB.95.235107`. 11

[61] A. Zorko, S. Nellutla, J. van Tol, L. C. Brunel, F. Bert, F. Duc, J.-C. Trombe, M. A. de Vries, A. Harrison, and P. Mendels, Dzyaloshinsky-Moriya Anisotropy in the Spin-1/2 Kagome Compound $ZnCu_3(OH)_6Cl_2$, Phys. Rev. Lett **101**, 026405(2008), URL . 11

[62] Y. Iqbal, F. Becca, S. Sorella and D. Poilblanc, Gapless spin-liquid phase in the kagome spin- 1/2 Heisenberg antiferromagnet, Phys. Rev. B **87**,060405(R)

(2013), URL `https://link.aps.org/doi/10.1103/PhysRevB.87.060405`. 11

[63] Y. Okamoto, H. Yoshida, and Z. Hiroi, Vesignieite $BaCu_3V_2O_8(OH)2$ as a Candidate Spin-1/2 Kagome, J.Phys. Soc. Jpn. **78**, 033701 (2009), URL `https://journals.jps.jp/doi/10.1143/JPSJ.78.033701`. 11

[64] David A. Huse, Classical antiferromagnets on the Kagome lattice, Phys. Rev. B**45**, 13 (1992), URL `http://link.aps.org/pdf/10.1103/PhysRevB.45.7536`. 11, 12

[65] MK. Kano and S. Naya, Antiferromagnetism. The Kagome Ising Net, Progress of Theoretical Physics **10**,2 (1953), URL `https://academic.oup.com/ptp/article-pdf/10/2/158/5229090/10-2-158.pdf`. 11, 12

[66] Y. Okamoto, M. Nohara, H. A. Katori, and H. Takagi, Spin-Liquid State in the S=1/2 Hyperkagome Antiferromagnet $Na_4Ir_3O_8$, Phys. Rev. Lett. **99**, 137207 (2007), URL `https://link.aps.org/doi/10.1103/PhysRevLett.99.137207`. xviii, 12, 27, 28, 29, 30, 33, 34, 35, 41, 48, 83, 84

[67] A. C. Shockley, F. Bert,J-C. Orain, Y. Okamoto, and P. Mendels, Frozen State and Spin Liquid Physics in $Na_4Ir_3O_8$: An NMR Study, Phys. Rev. Lett.**115**, 047201(2015), URL `https://link.aps.org/doi/10.1103/PhysRevLett.115.047201`. 12

[68] Y. Singh, Y. Tokiwa, J. Dong, and P. Gegenwart, Spin liquid close to a quantum critical point in $Na_4Ir_3O_8$, Phys. Rev. B **88**, 220413(2013), URL `https://link.aps.org/doi/10.1103/PhysRevB.88.220413`. 12, 27, 28, 35, 38

[69] B. Fauque, X. Xu, A. F. Bangura, E. C. Hunter, A. Yamamoto, K. Behnia, A. Carrington, H. Takagi, N. E. Hussey, and R. S. Perry, Thermal conductivity across the metal-insulator transition in the single-crystalline hyperkagome antiferromagnet $Na_{3+x}Ir_3O_8$ Phys. Rev. B **91**, 075129 (2015), URL `https://link.aps.org/doi/10.1103/PhysRevB.91.075129`. 12, 35, 38

[70] M.J. Lawler, A. Paramekanti, Y.B. Kim, and L. Balents, Gapless Spin Liquids on the Three-Dimensional Hyperkagome Lattice of $Na_4Ir_3O_8$, Phys. Rev. Lett. **110**, 197202 (2008), URL `https://link.aps.org/doi/10.1103/PhysRevLett.101.197202`. 12, 81, 83, 87

[71] Y. Zhou, P. A. Lee, T.K. Ng, and F.C. Zhang, $Na_4Ir_3O_8$ as a 3-D Spin Liquid with Fermionic Spinons, Phys. Rev. Lett. **101**, 197201 (2008), URL `https://link.aps.org/doi/10.1103/PhysRevLett.101.197201`. 12, 83, 87

[72] R. Dally, T. Hogan, A. Amato, H. Luetkens, C. Baines, J. Rodriguez-Rivera, Michael J. Graf, and Stephen D. Wilson, Short-Range Correlations in the Magnetic Ground State of $Na_4Ir_3O_8$, Phys. Rev. Lett. **113**,247601 (2014), URL `https://link.aps.org/doi/10.1103/PhysRevLett.113.247601`. 27, 33, 34

[73] M. Elhajal, B. Canals and C. Lacroix, Ordering in pyrochlore compounds due to Dzyaloshinsky-Moriya interactions: the case of Cu_4O_3, JPCM **16**, 11 (2004), URL `http://iopscience.iop.org/article/10.1088/0953-8984/16/11/049/meta`. xvii, 8

[74] Y. Iqbal, D. Poilblanc, R. Thomal and F. Becca, Persistence of the gapless spin liquid in the breathing kagome Heisenberg antiferromagnet, Phys. Rev. B **91**,020402(R) (2015), URL `https://link.aps.org/doi/10.1103/PhysRevB.97.115127`. 11

[75] M. Yoshida, M. Takigawa, H. Yoshida, Y. Okamoto, and Z. Hiroi, Phase Diagram and Spin Dynamics in Volborthite with a Distorted Kagome Lattice, Phys. Rev. Lett **103**, 077207 (2008), URL . 11

[76] R. W. Rollins, H. Kupfer, and W. Gey, Magnetic field profiles in type-II superconductors with pinning using a new ac technique, J. Appl. Phys. **45**,5392(1974), URL `https://aip.scitation.org/doi/10.1063/1.1663250`. 22

[77] R. W. Chantrell, and E. P. Wohlfarth, Dynamic and static properties of interacting fine ferromagnetic particles, J. Magn. Magn. Mater

40, 1 (1983), URL `https://www.sciencedirect.com/science/article/abs/pii/0304885383900021`. 22

[78] A. Olariu, P. Mendels, F. Bert, F. Duc, J. C. Trombe, M. A. de Vries, and A. Harrison, ^{17}O NMR Study of the Intrinsic Magnetic Susceptibility and Spin Dynamics of the Quantum Kagome Antiferromagnet $ZnCu_3(OH)_6Cl_2$, Phys.Rev.Lett.**100**,087202 (2008), URL `https://link.aps.org/doi/10.1103/PhysRevLett.100.087202`. 11

[79] G. Dhanraj, K. Byrappa, V. Prasad, and M. Dudley, editors. Handbook of Crystal Growth. Springer. 17

[80] A. R. West, Solid state chemistry and its applications, John Wiley and Sons, 1984. 17

[81] J. C. Brice, Crystal growth Processes, John Wiley and Sons, 1986. 17

[82] Physical Property Measurement System, EverCool II Option User's Manual, Part Number 1099-400, C0. 20

[83] Physical Property Measurement System, Vibrating Sample Magnetometer (VSM) Option, User's Manual, Part Number 1096-100, B0. 22

[84] Physical Property Measurement System, AC Measurement System (ACMS) Option, User's Manual, Part Number 1084-100 C-1. 23

[85] Physical Property Measurement System, Heat Capacity Option User's Manual, Part Number 1085-150, M1. 25, 26

[86] K. T. Law and P. A. Lee, 1T-TaS_2 as a quantum spin liquid, PNAS, **114(27)**, 6996-7000 (2017), URL `http://www.pnas.org/content/114/27/6996`. 27

[87] Z.A. Kelly, M.J. Gallagher, and T.M. McQueen, Electron Doping a Kagome Spin Liquid, Phys. Rev. X **6**, 041007 (2016), URL `https://journals.aps.org/prx/abstract/10.1103/PhysRevX.6.041007`. 27

[88] J.M. Hopkinson, S. V. Isakov, H.Y. Kee, and Y. B. Kim, Classical Antiferromagnet on a Hyperkagome Lattice, Phys. Rev. Lett. **99**, 037201 (2007), URL `https://link.aps.org/doi/10.1103/PhysRevLett.99.037201`. 81

[89] M.J. Lawler, H. Y. Kee, Y. B. Kim, and A. Vishwanath, Topological Spin Liquid on the Hyperkagome Lattice of $Na_4Ir_3O_8$, Phys. Rev. Lett. **100**, 227201 (2008), URL `https://link.aps.org/doi/10.1103/PhysRevLett.100.227201`. 81

[90] T. Takayama, A. Yaresko, A. Matsumoto, J. Nuss, K. Ishii, M. Yoshida, J. Mizuki and H. Takagi Spin-orbit coupling induced semi-metallic state in the 1/3 hole-doped hyper-kagome $Na_3Ir_3O_8$ Scientific Reports **4**,6818 (2014), URL `https://www.nature.com/articles/srep06818`. xxiii, 30, 31, 32, 38, 83

[91] T. Mizoguchi and K. Hwang,E. K.-H. Lee, and Y. B. Kim Generic model for the hyperkagome iridate $Na_4Ir_3O_8$ in the local-moment regime, Phys. Rev. B**94**, 064416 (2016), URL `https://link.aps.org/doi/10.1103/PhysRevB.94.064416`. 81

[92] S. N. Gupta, P. V. Sriluckshmy, A. Balodhi, D. V. S. Muthu, S. R. Hassan,Y. Singh, T. V. Ramakrishnan, and A. K. Sood, Spin liquid like Raman signatures in the hyperkagome iridate $Na_4Ir_3O_8$, Phys. Rev. B **94**, 155153 (2016), URL `https://link.aps.org/doi/10.1103/PhysRevB.94.155153`. xxii, 81, 82

[93] D. Podolsky, A. Paramekanti, Y. B. Kim, and T. Senthil, Mott Transition between a Spin-Liquid Insulator and a Metal in Three Dimensions, Phys. Rev. Lett. **102**, 186401(2009), URL `https://link.aps.org/doi/10.1103/PhysRevLett.102.186401`. 27, 40

[94] D. Podolsky and Y. B. Kim, Spin-orbit coupling in the metallic and spin-liquid phases of $Na_4Ir_3O_8$, Phys. Rev. B **83**, 054401,(2011), URL `https://journals.aps.org/prb/abstract/10.1103/PhysRevB.83.054401`. 27, 40

[95] P. Schiffer and I . Daruka, Two-population model for anomalous low-temperature magnetism in geometrically frustrated magnets, Phys. Rev. Lett. **56**, 13712 (1997), URL `http://link.aps.org/pdf/10.1103/PhysRevB.56.13712`. 46

[96] J.G. Rau, E.K. -H.Lee and H.-Y. Kee, Spin-Orbit Physics Giving Rise to Novel Phases in Correlated Systems: Iridates and Related Materials, Annu. Rev. Condens. Matter. Phys. , 195-221(2016), URL `https://www.annualreviews.org/doi/abs/10.1146/annurev-conmatphys-031115-011319`. 39

[97] A. Balodhi and Y. Singh Evolution of magnetic, transport, and thermal properties in $Na_4Ir_3O_8$, Phys. Rev. B1, 224409(2015), URL `https://link.aps.org/doi/10.1103/PhysRevB.91.224409`. 34, 38, 41, 48

[98] H. Zheng, J. Zhang, C. C. Stoumpos, Y. Ren, Yu-S. Chen,R. Dally, S. D. Wilson, Z. Islam, and J. F. Mitchell, Controlled vapor crystal growth of $Na_4Ir_3O_8$: A three-dimensional quantum spin liquid candidate, Phys. Rev. M., **2**, 043403 (2018), URL `https://link.aps.org/pdf/10.1103/PhysRevMaterials.2.043403`. 41, 43

[99] S. Yoon, S-H Baek, A. Balodhi, W-J Lee, K-Y Choi, I Watanabe, J S Lord, B Buchner, B J Suh and Y. Singh, Spin dynamics in $Na_{4-x}Ir_3O_8$ (x =0.3 and 0.7) investigated by ^{23}Na NMR and μSR, JPCM **27**, 48 (2015), URL `http://iopscience.iop.org/article/10.1088/0953-8984/27/48/485603/meta`. 30, 83, 86

[100] Y. Kurosaki, Y. Shimizu, K. Miyagawa, K. Kanoda, and G. Saito, Mott Transition from a Spin Liquid to a Fermi Liquid in the Spin-Frustrated Organic Conductor κ-$(ET)_2Cu_2(CN)_3$, Phys. Rev. Lett., **95**, 177001 (2005)., URL `https://link.aps.org/doi/10.1103/PhysRevLett.95.177001`. 27

[101] Y. Li, H. Liao, Z. Zhang, S. Li, F. Jin, L. Ling, L. Zhang, Y. Zou, Li Pi, Z. Yang, Junfeng Wang, Z. Wu Q. Zhang, Gapless quantum spin liquid ground state in the two - dimensional spin - 1/2 triangular antiferromagnet $YbMgGaO_4$,

Scientific Reports, **5**, 16419 (2015), URL `https://www.nature.com/articles/srep16419`. 62

[102] S. Petit, E. Lhotel, S. Guitteny, O. Florea, J. Robert, P. Bonville, I. Mirebeau, J. Ollivier, H. Mutka, E. Ressouche, C. Decorse, M. C. Hatnean, and G. Balakrishnan , Quantum fluctuations in spin-ice-like $Pr_2Zr_2O_7$, Phys. Rev. B , **9**4, 165153 (2016), URL `https://journals.aps.org/prb/abstract/10.1103/PhysRevB.94.165153`. 62

[103] K. Kimura, S. Nakatsuji, J-J. Wen, C. Broholm, M. B. Stone, E. Nishibori and H. Sawa, Quantum fluctuations in spin-ice-like $Pr_2Zr_2O_7$, Nature Communications, **4**, 1934 (2013), URL `https://www.nature.com/articles/ncomms2914`. 62

[104] Ashiwini Balodhi and Yogesh Singh, Synthesis and pressure and field-dependent magnetic properties of the kagome-bilayer spin liquid $Ca_{10}Cr_7O_{28}$, Phys. Rev. M.**1**, 1, 024407 (2017), URL `https://link.aps.org/doi/10.1103/PhysRevMaterials.1.024407`. 56, 57, 59, 63, 65, 71

[105] I. Kimchi and A. Vishwanath, Kitaev-Heisenberg models for iridates on the triangular, hyperkagome, kagome, fcc, and pyrochlore lattices, Phys. Rev. B.**89**, 014414 (2017), URL `https://link.aps.org/doi/10.1103/PhysRevB.89.014414`. 81